

Stellingen

behorende bij het proefschrift:

Computational aspects of biaxial stress in plain and reinforced concrete

van P.H. Feenstra

1. De reductie van de druksterkte tengevolge van laterale scheurvorming zoals voorgesteld door Vecchio en Collins is gebaseerd op foutieve experimenten en onjuiste theorievorming.
F.J. Vecchio en M.P. Collins, The response of reinforced concrete to in-plane shear and normal stresses. University of Toronto, 1982.
2. Volgens het kritisch rationalisme van Karl Popper dienen experimenten om een onderliggende theorie te falsificeren en niet om deze te verifiëren. De experimenten door Kollegger en Mehlhorn zijn dus niet uitgevoerd met deze kritisch rationalistische visie.
J. Kollegger en G. Mehlhorn, Experimentelle Untersuchungen zur Bestimmung der Druckfestigkeit des gerissenen Stahlbetons bei einer Querkzugbeanspruchung. Deutscher Ausschuß für Stahlbeton, 1990.
3. Stelling 3 van Vonk: "De afschuifscheuren, ... , zijn bepalend voor het bezwijken van een betonconstructie. De splitscheuren, ... , modificeren dit bezwijkgedrag", ondersteunt de aanname dat het compressiegedrag kan worden beschreven met een J_2 -criterium.
R.A. Vonk, Softening of concrete loaded in compression. Proefschrift Technische Universiteit Eindhoven 1992.
4. Het is onjuist te veronderstellen dat in een singulier punt van een vloeioppervlak de consistente tangent operator kan worden vervangen door de continuüm tangent operator.
5. Het gebruik van de tensorafschuifrek ε_{xy} in plaats van de ingenieursafschuifrek $\gamma_{xy} = 2 \varepsilon_{xy}$ in een eindige-elementenmethode dient nader onderzocht te worden.
6. Het berekenen van constructies met een niet-lineaire eindige-elementenmethode heeft als doel constructies minder sterk te maken.
7. Voor het ontwikkelen van stabiele numerieke mechanicamodellen dienen naast een gedegen kennis van numerieke methoden en computeraritmetica ook kennis van de specifieke kenmerken van compilers aanwezig te zijn.
8. In tegenstelling tot een mechanisch systeem is bij een mens een dieptepunt niet stabiel. Het menselijk wezen kan dus niet beschreven worden met een mechanisch model.
9. Bij het toekennen van een Europees project dient één van de criteria te zijn dat bij de deelnemers een minimale kennis van een gemeenschappelijke taal aanwezig is.
10. Sinds de invoering van het gescheiden inzamelen van huisafval is het straatbeeld aanmerkelijk vervuild.

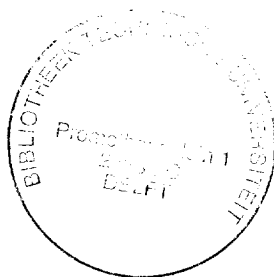
11. De naamgeving *onderzoekschool* doet vermoeden dat over enige jaren de vraag zal ontstaan naar een derde fase-opleiding voor *zelfstandig* onderzoeker.
12. Gezien het hoge aantal stellingen over het menselijk gedrag mag aangenomen worden dat promovendi beschikken over een brede ontwikkeling op het gebied van de sociale wetenschappen.
13. De invoering van een basisinkomen kan waarschijnlijk op een bredere steun rekenen als het gepresenteerd wordt als een instrument voor fraudebestrijding dan wanneer het gepresenteerd wordt vanuit een gelijkheidsbeginsel.
14. Door het hoge aantal fietsendiefstallen staat Nederland hoog in de internationale misdaadstatistieken. Gezien het feit dat fietsendiefstal in het algemeen gelaten wordt aanvaard, verdient het aanbeveling om van fietsendiefstal een overtreding te maken en zo het veiligheidsgevoel te vergroten.

COMPUTATIONAL ASPECTS OF BIAXIAL STRESS
IN
PLAIN AND REINFORCED CONCRETE

COMPUTATIONAL ASPECTS OF BIAXIAL STRESS

IN

PLAIN AND REINFORCED CONCRETE



PROEFSCHRIFT

ter verkrijging van de graad van doctor
aan de Technische Universiteit Delft,
op gezag van de Rector Magnificus, Prof. Ir. K. F. Wakker,
in het openbaar te verdedigen ten overstaan van een commissie
aangewezen door het College van Dekanen
op 29 november 1993 te 16.00 uur

door

PETER HENDRIKUS FEENSTRA

geboren te Sittard
civiel ingenieur

Dit proefschrift is goedgekeurd door de promotor :
Prof.dr.ir. R. de Borst

Published and distributed by

Delft University Press

Stevinweg 1

2628 CN Delft

The Netherlands

Telephone +31 15 783254

ISBN 90-6275-935-1 / CIP

Cover designed by

NOORDERBREEDTE ontwerp bureau Delft

Copyright © 1993 by P.H. Feenstra

All rights reserved.

No part of the material protected by this copyright notice may be reproduced or utilized in any form or by any means, electronic or mechanical, including photocopying, recording or by any information storage and retrieval system, without permission from the publisher:

Delft University Press, Stevinweg 1, 2628 CN Delft, The Netherlands.

Printed in The Netherlands.

ACKNOWLEDGEMENTS

The research reported in this thesis has been carried out at the Civil Engineering Department of Delft University of Technology. This research was supported by the Technology Foundation (STW) under grant DCT 72.1405. The additional financial support by TNO Building and Construction Research is highly appreciated.

I would like to gratefully acknowledge my supervisor Professor René de Borst for his guidance during this study. Furthermore, I wish to record thanks to all my colleagues of the Computational Mechanics Group of the Civil Engineering Department, Han Schellekens, Bert Sluys, Jerzy Pamin, Wang Wei Min, Zhangping Wu, Arend Groen and Paolo Lourenço for their interest and support during the work. I also wish to express my deep appreciation and gratitude to Jan Rots of TNO Building and Construction Research for his encouragements and fruitful discussions throughout the course of this study.

The models described in this thesis have been implemented in the DIANA finite element code of TNO Building and Construction Research which is commercially available through the DIANA Analysis b.v. The calculations have been performed on a Silicon Graphics Workstation operated by Harold Thung who I like to thank for his support.

CONTENTS

1. Introduction	1
1.1 Scope and objectives	2
1.2 Contents	2
2. Formulation and solution strategies	4
2.1 Finite element formulation	5
2.2 Constitutive model	8
2.3 Constrained Newton-Raphson method	12
2.4 Line search technique	15
2.5 Load estimation	17
2.6 Summary	19
3. Material model for plain and reinforced concrete	20
3.1 Discretization aspects	21
3.2 Uniaxial behavior of plain concrete	22
3.3 Biaxial behavior of plain concrete	27
3.4 Uniaxial behavior of reinforced concrete	28
3.5 Biaxial behavior of reinforced concrete	34
3.6 Summary	36
4. Modeling of plain concrete	37
4.1 Incremental formulations	38
4.1.1 The Rankine yield criterion	41
4.1.2 A composite yield criterion	54
4.2 Total formulations	67
4.2.1 Deformation theory of plasticity	68
4.2.2 Co-rotational formulation	70
4.3 Tension-shear model problem	81
4.3.1 Comparison of the total formulations	82
4.3.2 Comparison of incremental formulations with the rotating crack model	84
4.4 Summary	87
Appendix: Axisymmetrical formulation of the composite yield criterion	87
5. Application to plain concrete	95
5.1 Single-edge-notched beam	96
5.2 Pull-out of an anchor bolt	98
5.3 Cylinder splitting test	102
6. Modeling of reinforced concrete	105
6.1 Embedded formulation	106

6.2	Constitutive model of reinforced concrete	108
6.3	Constitutive model for reinforcing steel	109
6.4	Constitutive model for plain concrete	111
6.5	Validation of the tension-stiffening model	113
7.	Application to reinforced concrete	124
7.1	Analysis of deep beams	124
7.2	Analysis of shear wall panels	131
8.	Summary and concluding remarks	141
	References	144
	Samenvatting	149

1. INTRODUCTION

Reinforced concrete is one of the most commonly used materials in civil engineering with applications into all kinds of structures, such as high rise buildings, cooling towers and offshore platforms. The design of these structures is usually based on a linear-elastic analysis to calculate the internal forces in the structure which are then used to design the reinforcement and the details of the structure using code provisions. These codes are usually based on an empirical approach, using experimental data, and provide design rules to satisfy safety and serviceability requirements. Although the design of reinforced concrete structures based on a linear-elastic stress analysis is adequate and reliable in most cases, for complex structures under complex loading conditions, nonlinear finite element analyses are often required. With these analyses, information can be obtained regarding the ultimate load capacity and the post-failure behavior of the structure.

The behavior of concrete structures is characterized by a reduction of the load-carrying capacity with increasing deformations after reaching a certain limit load. This global behavior is usually caused by a material behavior which is described as strain softening and occurs in tension and in compression. Due to this softening behavior, the deformations tend to localize in a small part of the structure which can introduce mesh-dependent responses in finite element calculations. This deficiency can partially be solved by relating the constitutive model to a fracture energy and to the geometry of the finite element mesh via an equivalent length.

In reinforced concrete, the response of the structure is even more complicated. In general a number of cracks will develop in the structure due to the bond action between concrete and reinforcement. This results in a redistribution of the tensile load from concrete to reinforcement. This phenomenon is called tension-stiffening, because the response is stiffer than the response with a brittle fracture approach. The tension-stiffening is closely related to the tension-softening in plain concrete and the controversy between tension-softening and tension-stiffening approaches seems to have been exaggerated in the past. More important in the analysis of reinforced concrete structures is the problem of multiple equilibrium states during the process of crack formation. The localization due to the softening behavior induces local maxima in the load-displacement response, after which the structure unloads. In reinforced concrete, a number of cracks tend to localize which results in a set of local maxima. This can cause numerical difficulties in the solution algorithm.

Another issue which can cause numerical difficulties is the biaxial stress state, especially in tension-compression. The numerical problems are mainly due to the fact that the nonlinear behavior in tension, viz. cracking, is treated by a different constitutive model than the nonlinear behavior in compression, viz. plasticity and crushing. These different constitutive models are treated in different algorithms and a local iteration on a constitutive level is necessary to meet both the cracking and the plasticity conditions. This local iteration process can result in an oscillating numerical process if both cracking and plasticity occur in the same integration point. Because tension-compression

stress states often occur in reinforced concrete, this problem is encountered frequently.

The behavior of reinforced concrete is highly nonlinear which is caused by mechanisms such as cracking, crushing, creep and shrinkage of concrete, but also caused by interaction between reinforcement and concrete. Because all these mechanisms are interacting, it is not realistic to try to formulate a constitutive model which incorporates all these mechanisms, but a model has to be formulated which adequately describes the behavior of a structure within the range of application which has been restricted in advance. Although the constitutive models which are developed within this phenomenological approach are usually simplified representations of the real behavior of a material, it is believed that more insight can be gained by tracing the entire response of a structure in this manner, than modeling a structure with highly sophisticated material models which do not result in a converged solution after failure load. Since structural failure cannot be identified with divergence of the iterative procedure, the principal aim of this thesis is to develop robust algorithms in order to provide the structural engineer with reliable numerical tools.

1.1 Scope and objectives

This study is concerned with nonlinear failure analysis of plain and reinforced concrete structures which can be approximated as being in a state of plane stress, such as panels and shear walls. The structures under consideration are subjected to short time, static loads, which are not necessarily proportional, but the loading regime is such that the rotation of the directions of the principal strain vector remains moderate. The primary aim in this study will be the development and the evaluation of a numerical stable algorithm that handles the biaxial stress state in reinforced concrete. The objectives of this study are:

- to propose a solution technique which is stable and economic in the entire loading regime of the structure.
- to develop a constitutive model for reinforced concrete which incorporates the knowledge of nonlinear fracture mechanics used in crack propagation problems.
- to develop a constitutive model for concrete which is stable and robust in tension-tension, compression-compression and tension-compression stress states.
- to verify the developed models by comparing the predicted behavior with the behavior observed in experiments on different types of structures. The developed model should be able to predict the ultimate load and the failure mode within 30 % of the experimental behavior.

1.2 Contents

In Chapter 2, the fundamentals of the finite element method are briefly described and the general formulation of the constitutive model will be given. The solution technique

which will be utilized to solve equilibrium during the entire response will be discussed. The nonlinear system-of-equations which follows from the finite element discretization will be solved with an incremental-iterative Newton-Raphson method with arc-length control. The Newton-Raphson method will be enhanced with a line search technique to improve the global convergence characteristics of this method. The usual application of the incremental-iterative solution technique is with user-supplied incremental load steps. This method demands a-priori knowledge about the behavior of the structure to supply incremental load steps in accordance with the response of the structure. To solve this problem, a self-adaptive incremental load step procedure will be presented, which improves the global convergence characteristics considerably.

In Chapter 3, the material model for plain and reinforced concrete will be discussed. Experimental results indicate that the compressive and tensile behavior of plain concrete is governed by a similar failure mechanism, viz. cracking at the meso-level of the material. The accumulated damage in the material will be represented by two internal damage parameters, one in compression and one in tension. The constitutive model will be formulated as a relation between an equivalent stress and the internal damage parameter. The behavior of reinforced concrete under uniaxial tension will be modeled with a decomposition of the stiffness into the stiffness of the plain concrete, the stiffness of the reinforcement and an additional stiffness due to the interaction between concrete and steel after cracking. The tension-compression interaction in reinforced concrete will be discussed and a proposition will be put forward for the compressive strength reduction due to lateral cracking.

In Chapter 4, the constitutive model of plain concrete will be discussed. Two different approaches will be followed, the presentation of the constitutive model within an incremental, or rate formulation and the presentation of the constitutive model within a total formulation. The incremental formulation with a fracture energy-based plasticity model is considered as the most versatile and will be discussed in detail with respect to a consistent formulation of the tangential operator and the modeling of the biaxial stress state. The total formulation will be given merely to show the similarity of the fracture energy-based plasticity model and the rotating crack model. The behavior of the both formulations will be compared with a fundamental tension-shear model problem.

In Chapter 5, the developed constitutive models for plain concrete will be applied to simulate two experiments, a single-edge-notched beam and a pull-out of an anchor bolt, and to analyze a cylinder splitting test. The last analysis is mainly governed by tension-compression interaction, whereas the other two analyses are examples of crack propagation problems in plain concrete.

In Chapter 6, the modeling of reinforced concrete will be discussed. The embedded formulation of reinforcement will be given, as well as the constitutive model of the reinforcing steel. An idealized reinforced panel will be analyzed to examine the differences between the constitutive models for plain concrete when applied in the analysis of reinforced concrete panels. The proposed model for reinforced concrete will be validated with the analyses of reinforced panels subjected to uniaxial tension and to shear loading.

In Chapter 7, final examples will be presented to show the applicability of the fracture energy-based plasticity model and the model for reinforced concrete. The analyses concern two deep beams without shear reinforcement and a series of shear wall panels. For all analyses, the numerical results will be compared with the experimental data to assess the correlation between experiment and analysis.

In Chapter 8, a summary and final conclusions will be given which can be derived from this study.

2. FORMULATION AND SOLUTION STRATEGIES

In this study the finite element method will be adopted to simulate the behavior of structures. The maximum load capacity of a structure is the first interest in the analysis but it is also of importance to obtain an idea of the failure mode and the post-failure behavior of the structure. It has been recognized some years ago that numerical collapse, at which the iterative solution procedure no longer converges, has no physical meaning with regard to the real collapse of the structure. It is therefore of utmost importance that the entire structural response of the structure is traced with a solution procedure that remains stable even beyond the failure load of the structure.

In a finite element method based on the displacement method the structure is subdivided into elements for which the relation between the nodal forces and the displacements of the elements can be derived. The assembly of elements results in a system of equations describing the equilibrium of the structure which has to be solved to obtain the displacements of the structure. The complete response of the structure is calculated using an incremental analysis in which the total load is applied in a number of steps and a time variable t is introduced to conveniently describe the loading regime and displacement of the structure. The concept of time is used merely to order the sequence of events because time-independent behavior will be assumed in this study. Assume that at time t the equilibrium of the structure is satisfied and that a new load increment has been applied in a time increment Δt . The equilibrium equations need to be solved at time $t + \Delta t$. The equilibrium equations are in general nonlinear and an iterative procedure has to be employed to solve this problem. In this fashion, an incremental-iterative procedure is employed as the solution strategy to solve the equilibrium of a structure along the complete loading history of the structure. Equilibrium in a time step will be attained by means of the Newton-Raphson method which linearizes the nonlinear equilibrium conditions at each iteration. This iteration method has some deficiencies, as no globally convergent behavior can be established and as the method is unable to overcome limit points in the load-deformation response. These deficiencies can be remedied

using special techniques assuring globally convergent behavior of the method. The convergence of the Newton-Raphson method can be improved by using a line-search technique which calculates an optimal multiplier of the incremental displacement field following from the iterative procedure. An important addition to the Newton-Raphson method is the constraint of the incremental displacements which results in a constrained Newton-Raphson method. With this method it is possible to pass extremal points in the load-displacement response of a structure. The final part of the solution strategy is the method which is used to assess the load increments. It is seldom recognized in the literature that the procedure to calculate the load increments may be the most important part in the incremental-iterative solution strategy.

The main objective of this Chapter is to describe the finite element method and the solution procedure for a nonlinear continuum. Point of departure will be the virtual work principle. The general expression of the constitutive model will be given for a plane-stress situation which is assumed in the structures that will be analyzed in this thesis. The solution strategy which will adopted will be described in the remainder of this Chapter, which includes the constrained Newton-Raphson method, the line search technique and the estimation of the load increments.

2.1 Finite element formulation

Consider the equilibrium of a body B at time $t + \Delta t$ expressed in the weak form with the principal of virtual displacements, see Bathe (1982), as the residual G ,

$$G(\mathbf{u}, \delta\mathbf{u}) = \int_B \delta\boldsymbol{\varepsilon}^T \boldsymbol{\sigma} dV - \int_B \delta\mathbf{u}^T \mathbf{b} dV - \int_{\partial B} \delta\mathbf{u}^T \bar{\mathbf{t}} dS \quad (2.1)$$

in which \mathbf{u} the displacement vector with respect to a reference configuration denoted by \mathbf{x} and $\delta\mathbf{u}$ a kinematically admissible virtual displacement vector. The superscript T denotes the transpose symbol. As for the structures which will be considered in this study small displacement gradients will be assumed, the stress vector is given by $\boldsymbol{\sigma}$ and the linearized strain vector $\boldsymbol{\varepsilon}$ is defined by

$$\boldsymbol{\varepsilon} \stackrel{sym}{=} 1/2 \left(\frac{\partial \mathbf{u}}{\partial \mathbf{x}} + \frac{\partial \mathbf{u}^T}{\partial \mathbf{x}} \right) = \mathbf{L} \mathbf{u} \quad (2.2)$$

with \mathbf{L} a differential operator. The variation of the strain vector is denoted by $\delta\boldsymbol{\varepsilon}$. Furthermore, the loads on the body are given by the body forces \mathbf{b} and the tractions $\bar{\mathbf{t}}$ defined on a part of the boundary ∂B .

The solution of the equilibrium problem $G(\mathbf{u}, \delta\mathbf{u}) = 0$ is accomplished by a Newton-Raphson method, in which a sequence of linearized equations is solved

$$\frac{\partial G(\mathbf{u}^{(i)}, \delta \mathbf{u})}{\partial \mathbf{u}^{(i)}} \Delta \mathbf{u}^{(i+1)} = -G(\mathbf{u}^{(i)}, \delta \mathbf{u}) \quad (2.3)$$

until the residual G vanishes within a prescribed accuracy. The notation $\mathbf{u}^{(i)}$ denotes a quantity at equilibrium iteration (i) during load step $t + \Delta t$. The displacement vector is updated with the incremental displacement vector which results in

$$\mathbf{u}^{(i+1)} = \mathbf{u}^{(i)} + \Delta \mathbf{u}^{(i+1)} \quad (2.4)$$

The left-hand-side of the Newton-Raphson procedure can be elaborated to

$$\frac{\partial G(\mathbf{u}^{(i)}, \delta \mathbf{u})}{\partial \mathbf{u}^{(i)}} \Delta \mathbf{u}^{(i+1)} = \int_B \delta \boldsymbol{\varepsilon}^T \frac{\partial \boldsymbol{\sigma}^{(i)}}{\partial \boldsymbol{\varepsilon}^{(i)}} \frac{\partial \boldsymbol{\varepsilon}^{(i)}}{\partial \mathbf{u}^{(i)}} dV \Delta \mathbf{u}^{(i+1)} \quad (2.5)$$

Now define the consistent tangent stiffness matrix $\mathbf{D}^{(i)}$ as

$$\mathbf{D}^{(i)} = \frac{\partial \boldsymbol{\sigma}^{(i)}}{\partial \boldsymbol{\varepsilon}^{(i)}} \quad (2.6)$$

then the Newton-Raphson procedure reads

$$\int_B \delta \boldsymbol{\varepsilon}^T \mathbf{D}^{(i)} (\mathbf{L} \Delta \mathbf{u}^{(i+1)}) dV = -G(\mathbf{u}^{(i)}, \delta \mathbf{u}) \quad (2.7)$$

The incremental strain vector $d\boldsymbol{\varepsilon}^{(i+1)}$ is defined as

$$d\boldsymbol{\varepsilon}^{(i+1)} = \boldsymbol{\varepsilon}^{(i+1)} - \boldsymbol{\varepsilon}^{(i)} \quad (2.8)$$

which can be elaborated to

$$d\boldsymbol{\varepsilon}^{(i+1)} \stackrel{\text{sym}}{=} \frac{1}{2} \left(\frac{\partial \Delta \mathbf{u}^{(i+1)}}{\partial \mathbf{x}} + \frac{\partial \Delta \mathbf{u}^{(i+1)T}}{\partial \mathbf{x}} \right) = \mathbf{L} \Delta \mathbf{u}^{(i+1)} \quad (2.9)$$

with \mathbf{L} the differential operator. The virtual strain vector $\delta \boldsymbol{\varepsilon}$ is given as

$$\delta \boldsymbol{\varepsilon} = \delta d\boldsymbol{\varepsilon} \quad (2.10)$$

Substitution of eq.(2.1) and eq.(2.10) into eq.(2.7) results in the expression for the equilibrium equation of the body at $t + \Delta t$

$$\begin{aligned} \int_B \delta d\boldsymbol{\varepsilon}^T \mathbf{B}^T \mathbf{D}^{(i)} d\boldsymbol{\varepsilon}^{(i+1)} dV_0 = & - \int_B \delta d\boldsymbol{\varepsilon}^T \mathbf{B}^T \boldsymbol{\sigma}^{(i)} dV_0 \\ & + \int_B \delta \mathbf{u}^T \mathbf{b} dV + \int_{\partial B} \delta \mathbf{u}^T \bar{\mathbf{t}} dS \end{aligned}$$

The finite element formulation will be applied at this point to approximate the continuum displacement field \mathbf{u} with the discrete nodal displacements collected in a vector \mathbf{a} . The discrete incremental nodal degrees-of-freedom of an element and the continuum incremental displacement vector $\Delta \mathbf{u}$ are related by an interpolation matrix \mathbf{N} which is dependent upon the specific type of element employed. In general this relation is given by

$$\Delta \mathbf{u} = \mathbf{N} \Delta \mathbf{a} \quad (2.11)$$

with a interpolation matrix \mathbf{N} . The relation between the incremental strain vector and the displacement increment is in general given by the strain-nodal displacement matrix, $\mathbf{B} = \mathbf{L} \mathbf{N}$, which is dependent upon the specific element description via \mathbf{N} and the stress configuration via \mathbf{L} . With eq.(2.9) and eq.(2.11) the equilibrium equation reads

$$\begin{aligned} \int_B \delta \Delta \mathbf{a}^T \mathbf{B}^T \mathbf{D}^{(i)} \mathbf{B} \Delta \mathbf{a}^{(i+1)} dV = & \\ - \int_B \delta \Delta \mathbf{a}^T \mathbf{B}^T \boldsymbol{\sigma}^{(i)} dV_0 + \int_B \delta \Delta \mathbf{a}^T \mathbf{N}^T \mathbf{b} dV + \int_{\partial B} \delta \Delta \mathbf{a}^T \mathbf{N}^T \bar{\mathbf{t}} dS & \end{aligned} \quad (2.12)$$

Because the equilibrium equation must hold for any virtual displacement increment $\delta \Delta \mathbf{a}$, the Newton-Raphson equilibrium iteration in a nonlinear system discretized via the finite element method is given by

$$\mathbf{B}^T \mathbf{D}^{(i)} \mathbf{B} \Delta \mathbf{a}^{(i+1)} = - \int_B \mathbf{B}^T \boldsymbol{\sigma}^{(i)} dV + \mathbf{q} \quad (2.13)$$

with \mathbf{q} the generalized external load vector

$$\mathbf{q} = \int_B \mathbf{N}^T \mathbf{b} dV + \int_{\partial B} \mathbf{N}^T \bar{\mathbf{t}} dS \quad (2.14)$$

and the assembled stiffness matrix given by

$$\mathbf{K}^{(i)} = \int_B \mathbf{B}^T \mathbf{D}^{(i)} \mathbf{B} dV \quad (2.15)$$

2.2 Constitutive model

In the elaboration of the finite element equations, the constitutive model has not yet been defined. Since the principle of virtual work has been used, eq.(2.12) is independent of the constitutive model. The mathematical model of a constitutive law should give a relation between the stress tensor in a material point of the body ξ and the deformation in the actual configuration as a function of the time t , see e.g. Becker and Burger (1972), Willam and Dietsche (1992). The model is given by a functional f which is dependent upon the relative movement of a material point and all other material points of the body, or in general

$$\sigma(\xi, t) = \int_{\substack{s=0 \\ \eta \in B}}^{\infty} (x(\eta, t-s) - x(\xi, t-s)) ; \xi) \quad (2.16)$$

in which the material point η passes through the complete body. The model gives an interaction between all material points of the body and is the general description of the non-local material models. If the functional has the form of an integral, a typical representative of this class is the non-local damage model of Pijaudier-Cabot and Bažant (1987). Because the interaction of material points in a body is usually restricted to the neighborhood of the material points, the relative deformation is usually approximated by a truncated Taylor series, resulting in

$$\sigma(\xi, t) = \int_{s=0}^{\infty} (F(\xi, t-s), F_2(\xi, t-s), \dots, F_N(\xi, t-s)) ; \xi) \quad (2.17)$$

in which $F_N = \partial^N x / \partial \xi^N$. This material model is called a grade-N material and can be related to the so-called polar continuum models, e.g. the Cosserat continuum, see Mühlhaus (1989). Most constitutive models used in concrete structures come into the group of homogeneous, grade-1 materials, for which the stress tensor only depends on the first deformation gradient, and for which the material properties do not depend upon the material point ξ . These models are defined by

$$\sigma(\xi, t) = \int_{s=0}^{\infty} F(\xi, t-s) \quad (2.18)$$

The time dependent behavior which is still modeled explicitly with this formulation can be treated in a more convenient manner if the time-dependence is modeled by some internal variables, collected in a vector q , so that the functional is given by an integral of the stress rate. In this formulation the material model is given in an incremental formulation as

$$\sigma(\xi, t) = \int_0^t \dot{\sigma} d\tau = \int_0^t D_e \dot{\epsilon}_e d\tau \quad (2.19)$$

with D_e the linear-elastic stiffness matrix and the elastic strain rate given by the additive strain decomposition

$$\dot{\epsilon}_e = \dot{\epsilon} - \dot{\epsilon}_c$$

The inelastic strain rate $\dot{\epsilon}_c$ is assumed to be a function of the total strain rate and the internal variables, i.e. $\dot{\epsilon}_c = \dot{\epsilon}_c(\dot{\epsilon}, q)$. Material models which comply with this description are for instance the models which are based on the flow theory of plasticity.

Homogeneous, grade-1 materials can also be described with a total formulation in which the formulation of eq.(2.18) reduces to

$$\sigma(\xi) = f(F(\xi)) \quad (2.20)$$

which can be expressed as

$$\sigma = D_e \epsilon_e \quad (2.21)$$

with again the additive strain decomposition $\epsilon_e = \epsilon - \epsilon_c$, but with the inelastic strain vector now determined as a function of the total strain vector, $\epsilon_c = \epsilon_c(\epsilon)$.

Both classes of constitutive models, eq.(2.19) and eq.(2.21), can be defined in a general six dimensional stress and strain space, but it is more convenient to define the constitutive model in accordance with the stress situation in the analyzed structure. In a membrane configuration the stress and strain vectors are assumed to be given by

$$\begin{aligned} \sigma &= \{ \sigma_{xx} \quad \sigma_{yy} \quad \sigma_{zz} \quad \sigma_{xy} \}^T \\ \epsilon &= \{ \epsilon_{xx} \quad \epsilon_{yy} \quad \epsilon_{zz} \quad \gamma_{xy} \}^T \end{aligned} \quad (2.22)$$

respectively, where the stress σ_{zz} is assumed to be zero. The formulation of constitutive models in a plane-stress situation is possible via two approaches. The first approach is to omit the constrained stress component in the stress vector and formulate the constitutive model in a plane-stress situation. The second approach is to expand the strain vector in the constrained direction, formulate the constitutive model in a plain-strain situation and finally compress the stress vector such that the constrained condition is enforced rigorously, see De Borst (1991). In this study the latter approach is used because the formulation of the constitutive model based on the plasticity theory is more convenient in an unconstrained formulation. The linear-elastic constitutive relation in the unconstrained state is given by

$$D_e = \frac{E}{(1+\nu)(1-2\nu)} \begin{bmatrix} 1-\nu & \nu & \nu & 0 \\ \nu & 1-\nu & \nu & 0 \\ \nu & \nu & 1-\nu & 0 \\ 0 & 0 & 0 & 1/2(1-2\nu) \end{bmatrix} \quad (2.23)$$

In the linear-elastic state the strain component in the constrained direction $\varepsilon_{zz,e}$ is calculated from the constraint condition $\sigma_{zz} = 0$ which results in

$$\varepsilon_{zz,e} = -\frac{\nu}{1-\nu} (\varepsilon_{xx,e} + \varepsilon_{yy,e}) \quad (2.24)$$

In the nonlinear state the internal forces are calculated in an incremental-iterative manner and during this iterative procedure the strain vector is expanded in the constrained direction in the beginning of each equilibrium iteration. The updated stress vector is approximated with a first order Taylor expansion

$${}^{t+\Delta t}\boldsymbol{\sigma}^{(i+1)} \approx {}^{t+\Delta t}\boldsymbol{\sigma}^{(i)} + \frac{\partial {}^{t+\Delta t}\boldsymbol{\sigma}^{(i)}}{\partial {}^{t+\Delta t}\boldsymbol{\varepsilon}^{(i)}} d\boldsymbol{\varepsilon}^{(i+1)} = {}^{t+\Delta t}\boldsymbol{\sigma}^{(i)} + {}^{t+\Delta t}\mathbf{D}^{(i)} d\boldsymbol{\varepsilon}^{(i+1)} \quad (2.25)$$

in which the consistent tangent stiffness matrix ${}^{t+\Delta t}\mathbf{D}^{(i)}$ can be written as

$${}^{t+\Delta t}\mathbf{D}^{(i)} = \begin{bmatrix} D_{33} & D_{13} \\ D_{31} & D_{33} \end{bmatrix} \quad (2.26)$$

with

$$D_{33} = \begin{bmatrix} D_{11} & D_{12} & D_{14} \\ D_{21} & D_{22} & D_{24} \\ D_{41} & D_{42} & D_{44} \end{bmatrix} \quad (2.27)$$

and

$$\begin{aligned} D_{31} &= \{ D_{31}, D_{32}, D_{34} \} \\ D_{13} &= \{ D_{13}, D_{23}, D_{43} \}^T \end{aligned} \quad (2.28)$$

With this constitutive relation the updated stress vector in iteration $(i + 1)$ is written as

$$\begin{Bmatrix} {}^{t+\Delta t}\bar{\boldsymbol{\sigma}}^{(i+1)} \\ {}^{t+\Delta t}\sigma_{zz}^{(i+1)} \end{Bmatrix} = \begin{Bmatrix} {}^{t+\Delta t}\bar{\boldsymbol{\sigma}}^{(i)} \\ {}^{t+\Delta t}\sigma_{zz}^{(i)} \end{Bmatrix} + \begin{bmatrix} D_{33} & D_{13} \\ D_{31} & D_{33} \end{bmatrix} \begin{Bmatrix} d\bar{\boldsymbol{\varepsilon}}^{(i+1)} \\ d\varepsilon_{zz}^{(i+1)} \end{Bmatrix} \quad (2.29)$$

in which $\bar{\boldsymbol{\sigma}}$ the constrained stress vector

$$\bar{\boldsymbol{\sigma}} = \{ \sigma_{xx}, \sigma_{yy}, \sigma_{xy} \}^T \quad (2.30)$$

and $d\bar{\boldsymbol{\varepsilon}}$ the incremental constrained strain vector

$$d\bar{\boldsymbol{\varepsilon}} = \{ d\varepsilon_{xx}, d\varepsilon_{yy}, d\gamma_{xy} \}^T \quad (2.31)$$

Because of the plane-stress condition the incremental strain in constrained direction can be calculated as

$$d\epsilon_{zz}^{(i+1)} = - \frac{1}{{}^{t+\Delta t}D_{33}^{(i)}} ({}^{t+\Delta t}D_{31}^{(i)} d\epsilon^{(i+1)} + {}^{t+\Delta t}\sigma_{zz}^{(i)}) \quad (2.32)$$

During an iterative process σ_{zz} will converge to zero, but during the equilibrium-finding process, i.e. at non-converged states, the stress in the constrained direction is not necessarily zero and inclusion of ${}^{t+\Delta t}\sigma_{zz}^{(i)}$ prevents the constrained stress drifting away from the plane-stress condition during the iteration process. This algorithm fails if D_{33} of the tangent stiffness matrix becomes equal to zero and the constitutive model should always be analyzed for this limiting case to ensure a numerically stable algorithm. The compression of the stress vector is carried out by substitution of $d\epsilon_{zz}^{(i+1)}$ in the updated stress vector which results in

$${}^{t+\Delta t}\tilde{\sigma}^{(i+1)} = {}^{t+\Delta t}\tilde{\sigma}^{(i)} - {}^{t+\Delta t}D_{13}^{(i)} \frac{{}^{t+\Delta t}\sigma_{zz}^{(i)}}{{}^{t+\Delta t}D_{33}^{(i)}} + \left[D_{33}^{(i)} - \frac{D_{13}^{(i)} D_{31}^{(i)}}{D_{33}^{(i)}} \right] d\epsilon^{(i+1)} \quad (2.33)$$

The compression of the updated stress vector is performed as a regular static condensation with an additional correction on the compressed stress vector due to the non-zero intermediate stress in the constrained direction. Substitution of eq.(2.33) into the equilibrium condition, cf. eq.(2.13),

$$\int_B B^T {}^{t+\Delta t}\sigma^{(i+1)} = {}^{t+\Delta t}q$$

results in the Newton-Raphson equilibrium iteration in the constrained stress state

$$\int_B B^T {}^{t+\Delta t}\tilde{D}^{(i)} B dV \Delta a^{(i+1)} = {}^{t+\Delta t}q - \int_B B^T \left\{ {}^{t+\Delta t}\tilde{\sigma}^{(i)} - {}^{t+\Delta t}D_{13}^{(i)} \frac{{}^{t+\Delta t}\sigma_{zz}^{(i)}}{{}^{t+\Delta t}D_{33}^{(i)}} \right\} dV$$

in which \tilde{D} the statically condensed consistent tangent stiffness matrix

$$\tilde{D} = \left[D_{33} - \frac{D_{13} D_{31}}{D_{33}} \right] \quad (2.34)$$

The correction on the internal force vector due to the non-zero intermediate stress ${}^{t+\Delta t}\sigma_{zz}^{(i)}$ disturbs the flow of a finite element calculation in which the internal force vector is calculated with the updated stress vector at the end of the previous iteration, that is before the updated tangent stiffness matrix is calculated. It is more convenient to correct the internal force vector with the tangent stiffness matrix ${}^{t+\Delta t}D^{(i-1)}$ and to apply afterwards a correction vector

$${}^{t+\Delta t}\mathbf{r}^{(i)} = \int_V \mathbf{B}^T \left\{ \frac{{}^{t+\Delta t}\mathbf{D}_{13}^{(i)}}{{}^{t+\Delta t}\mathbf{D}_{33}^{(i)}} - \frac{{}^{t+\Delta t}\mathbf{D}_{13}^{(i-1)}}{{}^{t+\Delta t}\mathbf{D}_{33}^{(i-1)}} \right\} {}^{t+\Delta t}\sigma_z^{(i)} dV \quad (2.35)$$

It is important that the correction is indeed applied as has been shown by De Borst (1991).

2.3 Constrained Newton-Raphson method

In this study, the solution of the equilibrium problem will be accomplished by a Newton-Raphson iteration in which the system of equations following from the finite element discretization is solved. This system of equations is expressed as (cf. eq.(2.13))

$${}^{t+\Delta t}\mathbf{K}^{(i)} \Delta \mathbf{a}^{(i+1)} = - {}^{t+\Delta t}\mathbf{g}^{(i)}$$

with \mathbf{K} the assembled tangential stiffness matrix, eq.(2.15), and the unbalance force vector

$${}^{t+\Delta t}\mathbf{g}^{(i)} = \int_B \mathbf{B}^T {}^{t+\Delta t}\boldsymbol{\sigma}^{(i)} dV - {}^{t+\Delta t}\mathbf{q}$$

The generalized external load vector ${}^{t+\Delta t}\mathbf{q}$ is as defined in eq.(2.14). The total load vector is normally applied in a number of loading steps and for each step equilibrium iterations will be performed. The Newton-Raphson method in an incremental-iterative fashion is now rewritten as

$${}^{t+\Delta t}\mathbf{K}^{(i)} \Delta \mathbf{a}^{(i+1)} = {}^{t+\Delta t}\Delta \mu^{(i+1)} \hat{\mathbf{q}} + \mathbf{p}^{(i)} \quad (2.36)$$

with ${}^{t+\Delta t}\Delta \mu^{(i+1)}$ the incremental load factor in iteration $(i+1)$, related to a reference external load vector $\hat{\mathbf{q}}$. The vector $\mathbf{p}^{(i)}$ is defined as

$$\mathbf{p}^{(i)} = {}^t\mu^{(n)} \hat{\mathbf{q}} - \int_B \mathbf{B}^T {}^{t+\Delta t}\boldsymbol{\sigma}^{(i)} dV \quad (2.37)$$

with ${}^t\mu^{(n)}$ the total load factor at the end of the previous time step t . The Newton-Raphson method and the used notation are depicted in Figure 2.1.

A crucial part of the incremental-iterative procedure is that the initial incremental load factor has to be adapted to the structural behavior. If the initial load factor is chosen properly the convergence behavior of the Newton-Raphson method is in general quadratic. The standard load control method in which the initial load factor is kept constant during the equilibrium iterations is not very efficient and fails at limit points. To overcome this deficiency, a constraint equation has to be added to the nonlinear equilibrium equations as an additional equation which has the general form

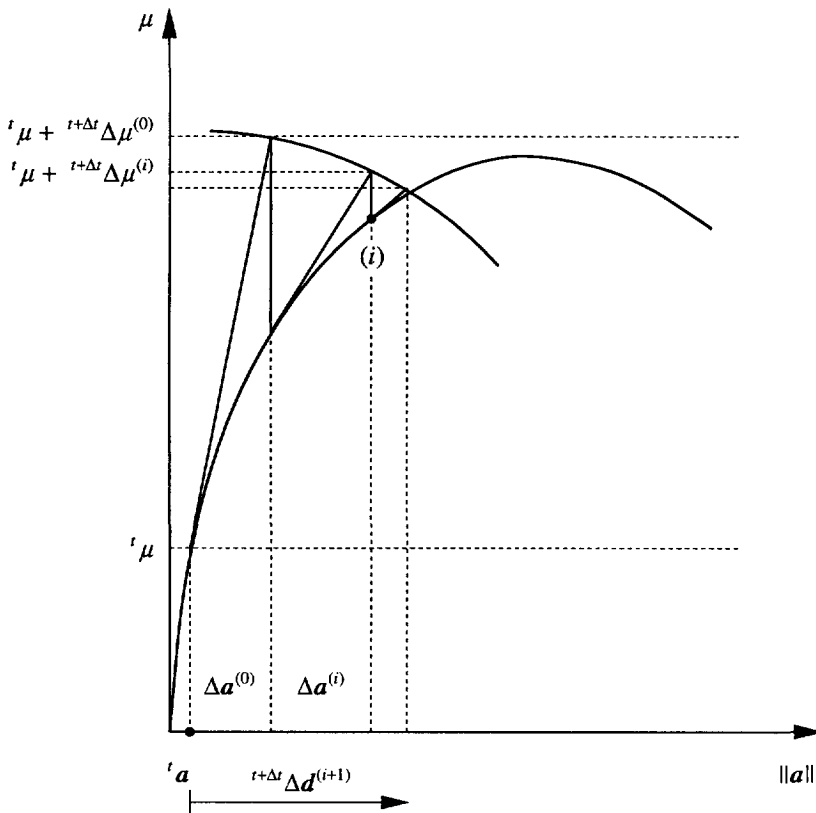


Figure 2.1 Constrained Newton-Raphson method and notation.

$$f(\beta \Delta \mu, a) = 0 \quad (2.38)$$

This technique, introduced by Riks (1970) and by Wempner (1971), gives the possibility to overcome limit points by iterating in the load-displacement space. The constraint equation depends upon the updated incremental displacement vector and upon the load factor via a scalar β , which reflects the influence of the load factor on the constraint. The factor β can be considered as a scaling factor for which different proposals have been put forward, Schweizerhof and Wriggers (1986). Crisfield (1981) and Ramm (1981) have suggested to set the factor equal to zero, thus avoiding the dimensional incompatibility between the displacements and the load factor. Further analyses in which the influence of the β -factor has been studied, see Langeslag (1992), showed that the β -factor hardly affects the convergence characteristics of the calculation. It is therefore assumed in this study that the β -factor is equal to zero.

In the incremental displacement vector splitting technique of Batoz and Dhett (1979), the incremental displacement vector $\Delta a^{(i+1)}$ is decomposed into two parts

$$\begin{aligned}\Delta^I \mathbf{a}^{(i+1)} &= \mathbf{K}^{-1} \mathbf{p}^{(i)} \\ \Delta^H \mathbf{a}^{(i+1)} &= \mathbf{K}^{-1} \hat{\mathbf{q}}\end{aligned}\tag{2.39}$$

which results in

$$\Delta \mathbf{a}^{(i+1)} = \Delta^I \mathbf{a}^{(i+1)} + {}^{t+\Delta t} \Delta \mu^{(i+1)} \Delta^H \mathbf{a}^{(i+1)}\tag{2.40}$$

With the additional constraint equation, eq.(2.38) this method is known as a constrained incremental Newton-Raphson method. With this technique, introduced by Crisfield (1981) and by Ramm (1981), the solution algorithm has an appropriate form for finite element methods.

Introducing the total incremental displacement vector $\Delta \mathbf{d}$, see Figure 2.1, which is updated with the incremental displacement vector, $\Delta \mathbf{a}^{(i+1)}$, according to

$${}^{t+\Delta t} \Delta \mathbf{d}^{(i+1)} = {}^{t+\Delta t} \Delta \mathbf{d}^{(i)} + \Delta \mathbf{a}^{(i+1)}\tag{2.41}$$

the constraint equations can be derived from orthogonality principles between the total incremental displacement vector and incremental displacement vector, see Forde and Stierner (1987). The scalar product of these two vectors results in a general expression for the incremental load factor

$${}^{t+\Delta t} \Delta \mu^{(i+1)} = \frac{R^{(i+1)} - {}^{t+\Delta t} \Delta \mathbf{d}^{(i)T} \Delta^I \mathbf{a}^{(i+1)}}{{}^{t+\Delta t} \Delta \mathbf{d}^{(i)T} \Delta^H \mathbf{a}^{(i+1)}}\tag{2.42}$$

Different formulations for the residual $R^{(i+1)}$ in eq.(2.42) have been proposed in literature but comparison of these methods for a variety of structures shows that the actual choice of the constraint equation is of minor influence compared with the load estimation algorithm which is used, see Feenstra and Schellekens (1991) and Schellekens (1992). In this study the constraint method which is based on linearization of a hypersurface in the displacement space, the updated-normal-plane method will be applied. This method, proposed by Ramm (1981), is based on orthogonality between tangent vector and update vector, i.e. $R^{(i+1)} = 0$ and the incremental load factor is given by

$${}^{t+\Delta t} \Delta \mu^{(i+1)} = - \frac{{}^{t+\Delta t} \Delta \mathbf{d}^{(i)T} \Delta^I \mathbf{a}^{(i+1)}}{{}^{t+\Delta t} \Delta \mathbf{d}^{(i)T} \Delta^H \mathbf{a}^{(i+1)}}\tag{2.43}$$

The constrained Newton-Raphson method can further be enhanced with a numerical relaxation technique which is applied if the incremental load factors are oscillating, Schweizerhof and Wriggers (1986). The constraint algorithm is oscillating if

$$({}^{t+\Delta t} \Delta \mu^{(i+1)} - {}^{t+\Delta t} \Delta \mu^{(i)}) ({}^{t+\Delta t} \Delta \mu^{(i)} - {}^{t+\Delta t} \Delta \mu^{(i-1)}) < 0\tag{2.44}$$

and

$$| {}^{t+\Delta t}\Delta\mu^{(i+1)} - {}^{t+\Delta t}\Delta\mu^{(i)} | > | {}^{t+\Delta t}\Delta\mu^{(i)} - {}^{t+\Delta t}\Delta\mu^{(i-1)} | \quad (2.45)$$

If this happens, the incremental load factor is calculated as

$${}^{t+\Delta t}\Delta\mu^{(i+1)} = {}^{t+\Delta t}\Delta\mu^{(i)} + \alpha ({}^{t+\Delta t}\Delta\mu^{(i+1)} - {}^{t+\Delta t}\Delta\mu^{(i)}) \quad (2.46)$$

The factor α is generally chosen equal to 0.5, see Schweizerhof and Wriggers (1986).

In case of strong localization, the constrained Newton-Raphson method can still fail which is caused by the fact that the constraint equation is based on all displacement degrees-of-freedom. To overcome this problem, De Borst (1986) proposed to confine the number of degrees-of-freedom in the constraint equation. This indirect displacement control method has been used in analyses which were concerned with crack propagation and with discrete cracking in composite laminates and this method is reported to be highly successful, Rots (1988), Schellekens (1992). A major draw-back of the method is the fact that the dominant degrees-of-freedom have to be selected a-priori but this can be avoided if techniques based on an eigenvalue analysis are used, see Napoleão, Elwi and Murray (1992). In this study, the indirect displacement control method will be used with a single degree-of-freedom which is actually the displacement control method used by Batoz and Dhatt (1979) and Ramm (1981). The displacement vector in the constraint equation is now given by

$$\Delta\mathbf{d} = \{ 0, 0, 0, \dots, \Delta\bar{d}_p, \dots, 0, 0, 0 \}^T \quad (2.47)$$

with $\Delta\bar{d}_p$ the prescribed displacement increment of the active degree-of-freedom. The choice of this degree-of-freedom should be made with engineering judgement and should fulfil the requirement that it is a continuously increasing degree-of-freedom. The incremental load vector is now given by

$${}^{t+\Delta t}\Delta\mu^{(i+1)} = - \frac{\Delta^I a_p^{(i+1)}}{\Delta^II a_p^{(i+1)}} \quad (2.48)$$

which follows directly from the prescribed displacement which should be constant during the iterations, i.e. $\Delta a_p^{(i+1)} = 0$.

2.4 Line search technique

Application of line search techniques to the solution of nonlinear equations can be a significant enhancement of the robustness of the Newton-Raphson method. However, most studies, Matthies and Strang (1979), Crisfield (1982), Crisfield (1983), Schweizerhof (1992), report the application of line search techniques to a modified Newton-Raphson

method which should be regarded as less robust than the full Newton-Raphson method, or to variable metric methods which in general do not work properly without a line search technique. In this study the full Newton-Raphson method will be adopted and the line search technique will be used to enhance the robustness of the iteration of the equilibrium. Especially if the consistent tangent operator will be used, the full Newton Raphson procedure with line searches will result in an economic solution procedure, Crisfield (1987).

The line search technique can be regarded as a minimization of the total potential energy Π in a given direction \mathbf{n} which results in a minimization with respect to the scalar s ,

$$\min \Pi \rightarrow \frac{\partial \Pi}{\partial s} = \frac{\partial \Pi^T}{\partial \mathbf{a}} \frac{\partial \mathbf{a}}{\partial s} = \mathbf{g}^{(t+\Delta t) \mathbf{a}^{(i+1)}})^T \frac{\partial \mathbf{n}}{\partial s} = 0 \quad (2.49)$$

if the updated displacement vector is given by

$${}^{t+\Delta t} \mathbf{a}^{(i+1)} = {}^{t+\Delta t} \mathbf{a}^{(i)} + \mathbf{n}^{(i+1)}$$

and if the arbitrary update direction $\mathbf{n}^{(i+1)}$ is a function of the scalar s_k , the line search factor which scales the incremental displacement field. The line search algorithm calculates the scalar s for which the potential energy of the system is minimum in the direction \mathbf{n} . The condition given in eq.(2.49) is not satisfied exactly because the use of weak acceptance criteria generally performs better, Dennis and Schnabel (1983). The choice of the search direction is the critical part of the line search technique, Matthies and Strang (1979), who use a method based on the BFGS-method to determine the new search direction. It is not readily possible to implement this method in general purpose finite element codes like DIANA, because of the specific structure of these programs, and the search direction used in this study is determined by the incremental displacement vector $\Delta \mathbf{a} = \mathbf{K}^{-1} \mathbf{g}$. The search vector is now given by

$$\mathbf{n}^{(i+1)} = s_k \Delta \mathbf{a}^{(i+1)} = s_k (\Delta^I \mathbf{a} + {}^{t+\Delta t} \Delta \mu^{(i+1)} \Delta^II \mathbf{a}) \quad (2.50)$$

Because the load factor ${}^{t+\Delta t} \Delta \mu^{(i+1)}$ is in general a function of the incremental displacement vector, the combination of the line search technique with a constrained Newton-Raphson method results in load level adjustment during the line searches. This drawback can be avoided if the updated-normal-plane constraint is used in conjunction with the line search algorithm. The residual is then given by

$$R^{(i+1)} = {}^{t+\Delta t} \Delta \mathbf{a}^{(i)T} s_k \Delta \mathbf{a}^{(i+1)} = 0 \quad (2.51)$$

which results in the updated incremental load factor

$${}^{t+\Delta t}\Delta\mu^{(i+1)} = - \frac{{}^{t+\Delta t}\Delta\mathbf{d}^{(i)T} \Delta^I \mathbf{a}^{(i+1)}}{{}^{t+\Delta t}\Delta\mathbf{d}^{(i)T} \Delta^II \mathbf{a}^{(i+1)}} \quad (2.52)$$

which is indeed not influenced by the line search factor s_k and the line search can be performed on a constant load level. The minimization reduces to the scalar equation

$$\mathbf{g}({}^{t+\Delta t}\mathbf{a}^{(i)} + s_k \Delta\mathbf{a}^{(i+1)})^T \Delta\mathbf{a}^{(i+1)} = 0 \quad (2.53)$$

which will be solved using the regula-falsi method. If the line search algorithm is applied the additional cost is negligible compared with the calculation of the internal force vector because the initial energy at $s_k = 0$ is calculated as the inner product of the incremental displacement vector and the unbalance-force vector from the previous iteration and the energy at $s_k = 1$ is always known by the scalar product because the internal force vector is always calculated once. The criterion which has to be fulfilled reads

$$|\mathbf{g}({}^{t+\Delta t}\mathbf{a}^{(i)} + s_k \Delta\mathbf{a}^{(i+1)})^T \Delta\mathbf{a}^{(i+1)}| \leq \eta |\mathbf{g}({}^{t+\Delta t}\mathbf{a}^{(i)})^T \Delta\mathbf{a}^{(i+1)}| \quad (2.54)$$

with η a tolerance factor, which is usually chosen equal to 0.8 for the Newton-Raphson method. This slack criterion is usually fulfilled in the first line search. The line search algorithm is supplemented with a stopping criterion if no significant update is calculated and if the line search factors are close together. A cut-off criterion is used if an extrapolation is calculated, Schweizerhof and Wriggers (1986).

2.5 Load estimation

The Newton-Raphson method is used within the context of an incremental-iterative procedure. The load is applied in a number of steps with each incremental load step given by the user. This method demands knowledge about the behavior of the structure to supply incremental load factors in accordance with the structural response. Directly related is the question whether to increment or decrement the load factor when a snap-back or a snap-through occurs in the load-displacement path. Both issues should be solved to obtain a stable solution strategy to analyze the nonlinear response of structures.

Different proposals for a self-adaptive loading method have been put forward, see Clarke and Hancock (1990) for an overview, but in physically-nonlinear analyses a work-based method shows good performance, see Feenstra and Schellekens (1991). The work-based method which will be used in this study can be considered as an unscaled version of Bergan's stiffness parameter method, Bergan (1982) and Crisfield (1983), and can be conceived as a measure for external work or strain energy. Suppose, the total external work at time t is given by

$${}^tW = 1/2 {}^t\Delta\mu^{(n)} {}^t\Delta\mathbf{d}^{(n)T} \hat{\mathbf{q}} \quad (2.55)$$

with the total incremental displacements ${}^t\Delta\mathbf{d}^{(n)}$ at the end of the previous time step with the corresponding load factor ${}^t\Delta\mu^{(n)}$. It is now assumed that this work is equal to the approximated external work in step $t + \Delta t$

$${}^{t+\Delta t}\bar{W} \approx 1/2 \ {}^{t+\Delta t}\Delta\mu^{(0)T} \ {}^{t+\Delta t}\Delta\mu^{(0)} \ \hat{\mathbf{q}} \quad (2.56)$$

with ${}^{t+\Delta t}\Delta\mathbf{d}^{(0)} = {}^{t+\Delta t}\Delta\mu^{(0)} \ \Delta^{II} \mathbf{a}^{(0)}$ this results in

$$({}^{t+\Delta t}\Delta\mu^{(0)})^2 = \frac{{}^t\Delta\mu^{(n)} \ {}^t\Delta\mathbf{d}^{(n)T} \ \hat{\mathbf{q}}}{\Delta^{II} \mathbf{a}^{(0)T} \ \hat{\mathbf{q}}} \quad (2.57)$$

The initial load factor in step $t + \Delta t$ is given by

$${}^{t+\Delta t}\Delta\mu^{(0)} = \left(\frac{|{}^t\Delta\mu^{(n)} \ {}^t\Delta\mathbf{d}^{(n)T} \ \hat{\mathbf{q}}|}{|\Delta^{II} \mathbf{a}^{(0)T} \ \hat{\mathbf{q}}|} \right)^{1/2} \quad (2.58)$$

In order to calculate the the proper approximation of the external work it is necessary to use the tangent stiffness matrix in the first iteration of the new load increment. When a modified Newton-Raphson iteration method is used with initially the previous tangent or even the linear-elastic stiffness matrix, this method may fail due to a severe over-estimation of the new load factor. In order to circumvent that the load factor becomes too large or impractically small, the load factor should be bounded between a lower and an upper bound which will be dependent on the structural behavior, as

$$\Delta\mu_{\min} \leq |{}^{t+\Delta t}\Delta\mu^{(0)}| \leq \Delta\mu_{\max} \quad (2.59)$$

A major problem of this method is that the calculated load factor will be reduced in time steps near limit points in the behavior of the structure, but that the load factor is not increased if the behavior after a limit point is nearly linear. This problem mainly occurs in geometrically-nonlinear analyses. In physically-nonlinear analyses this problem is less dominant. Usually only one limit point will be encountered, after which an unstable branch has to be traced in which small steps are needed anyway to achieve convergence.

The indirect displacement method based on a single degree-of-freedom is in fact a solution technique in which a displacement is prescribed and the external load factor is calculated such that during the iterations the prescribed value will be reached. The initial load factor is now completely defined by the user-supplied value of the prescribed degree-of-freedom $\Delta\bar{d}_p$ and the current stiffness of the structure. The initial load factor in case of an indirect displacement control method is given by

$${}^{t+\Delta t}\Delta\mu^{(0)} = \frac{\Delta\bar{d}_p}{\Delta^{II} a_p^{(0)}} \quad (2.60)$$

The total load factor should be decremented when the response of the structure shows a global softening response. The sign of the load factor can be determined using different methods. The first method is that unloading is initiated whenever a negative pivot is encountered in the triangularized global stiffness matrix. The method fails when a bifurcation point exists in the load-displacement path and should therefore be used with care in an application to reinforced concrete structures, but has proved to be successful in nonlinear analyses with sharp snap-back behavior due to a discrete failure mode. The second method is similar to the one used by Crisfield (1981) to determine the appropriate root of the quadratic equation for the quadratic constraint methods. The total incremental displacements in step t are given by ${}^t\Delta\mathbf{d}^{(n)}$ and the appropriate load factor is chosen which gives a positive value for the vector product of the total incremental displacements in the previous time step and the incremental displacements in the first iteration of the following time step, so

$${}^{t+\Delta t}\Delta\mu^{(0)} = \begin{cases} + |{}^{t+\Delta t}\Delta\mu^{(0)}| & \text{if } {}^t\Delta\mathbf{d}^{(n)T} \Delta^H \mathbf{a}^{(0)} \geq 0 \\ - |{}^{t+\Delta t}\Delta\mu^{(0)}| & \text{if } {}^t\Delta\mathbf{d}^{(n)T} \Delta^H \mathbf{a}^{(0)} < 0 \end{cases} \quad (2.61)$$

Numerous analyses with this method, Feenstra and Schellekens (1991), show that this method is successful in tracing the complete load-displacement path even with severe snap-back and snap-through behavior. The method is also used by Bellini and Chulya (1987) who also claim this method to be highly successful.

2.6 Summary

A formulation of the finite element equations has been given which is derived from the principle of virtual work without assumptions about the constitutive model. The constitutive models which will be used in this study are based either on an incremental formulation or on a total formulation. The application in membranes justifies the assumption of a plane-stress condition. However, the formulation of the constitutive models will be given in an unconstrained situation where the constrained condition is enforced by a compression/expansion method.

The nonlinear equations which result from the equilibrium condition are solved in an incremental-iterative procedure by means of the Newton-Raphson method. The tangent stiffness matrix which is necessary in this method has to be calculated consistently with the Newton-Raphson method in order to retain the quadratic convergence characteristics of the iteration method. To overcome limit points, the Newton-Raphson method will be used in conjunction with an arc-length technique, the updated-normal-plane method, which provides a solution strategy which is capable of handling snap-back and snap-through behavior in the load-displacement. The robustness of the Newton-Raphson method has been enhanced using a line search technique and a numerical relaxation

method. The estimation of the increment in a load step is probably the most important issue and a work-based method has been discussed to assess the load increment. The loading/unloading criterion can be founded on two mechanism. The first method is based on the existence of negative pivots in the global stiffness matrix and will be used if strong localizations dominate the global response. The second method is based on displacements and it has been shown that this method is stable if the failure mode has a global character.

The solution strategy which will be adopted in this study is given by the Newton-Raphson iteration method with a consistent formulation of the tangent stiffness matrix. The Newton-Raphson method will be constrained with the updated-normal-plane method in order to overcome limit points. The robustness of the iteration method will be enhanced with a line search algorithm with a maximum of line searches equal to five and a convergence tolerance $\eta = 0.8$. Numerical relaxation with a factor α equal to 0.5 will be used throughout the analyses. The iteration is assumed to be converged if the norm of the unbalance force vector is less or equal to 10^{-3} times the norm of the reference unbalance force vector calculated at the beginning of each load step. The incremental load factor will be calculated using the work-based method with the sign of the load increment determined with either one of the methods discussed above depending on the specific application. If converged solutions cannot be reached with this solution procedure, indirect displacement techniques will be used to ensure converged solution. When this technique is used, it will be mentioned explicitly.

In the applications which will be presented in this thesis, no attempt will be made to compare different solution techniques. Because the behavior of these structures is highly nonlinear, the convergence characteristics are influenced by many factors and an objective comparison of different solution techniques is hardly possible. The analyses show that with the proposed solution technique, convergent solutions could be obtained which indicates that the proposed combination of techniques results in a stable solution procedure.

3. MATERIAL MODEL FOR PLAIN AND REINFORCED CONCRETE

In experiments on plain concrete, two types of failure are observed which are both characterized by the formation of cracks in the material. When a concrete specimen is loaded in tension the response is nearly linearly up to the maximum load. At peak load existing cracks at micro-level due to hydration and drying shrinkage, see Wittman (1983), localize in a narrow band and a macro-crack develops in the process zone what is attended with a decrease of the external load, Hordijk (1991). Recently, also the

compressive failure of concrete has been recognized to be governed by cracking of concrete, Van Mier (1984), Vonk (1992). The crack growth at the micro-level causes the softening behavior of concrete under compression. Until about 30 % of the maximum compressive strength the material behaves linear-elastically because pre-existing micro cracks are stable and do not propagate. These micro cracks start to grow if the specimen is loaded further and up to the maximum compressive strength the formation of combined mortar and bond cracks have been observed. After the maximum compressive strength macro cracks develop because the micro cracks localize in narrow bands which is attended with a decrease of the external applied load.

The behavior of reinforced concrete is also characterized by the formation of cracks in the material. The major difference with plain concrete is the bond action between concrete and reinforcement which results in the formation of a number of cracks and a redistribution of internal stresses from concrete to reinforcement.

The constitutive behavior will be modeled according to a phenomenological approach in which the observed mechanisms are modeled in such a fashion that simulations with the developed material model are in reasonable agreement with the experiments.

3.1 Discretization aspects

The constitutive behavior of concrete will be modeled with a smeared model in which the damaged material is still considered as a continuum in which the notions of stress and strain apply. With this assumption, the localized damage can be represented by an internal damage parameter, denoted as κ , which is related by an equivalent length to the released energy per unit cracked area, G_f . In a finite element calculation this equivalent length should correspond to a representative dimension of the mesh size, as pointed out by many authors, see Bažant and Oh (1983), Crisfield (1984), Willam, Pramono and Sture (1986), Rots (1988) and Oliver (1989). The equivalent length, denoted by h , depends in general on the chosen element type, element size, element shape, integration scheme and even on the particular problem considered. In this study it is assumed that the equivalent length is related to the area of an element, as follows

$$h = \alpha_h \sqrt{A_e} = \alpha_h \left(\sum_{\xi=1}^{n_\xi} \sum_{\eta=1}^{n_\eta} \det(\mathbf{J}) w_\xi w_\eta \right)^{1/2} \quad (3.1)$$

in which w_ξ and w_η the weight factors of the Gaussian integration rule as it is tacitly assumed that the elements are always integrated numerically. The local, isoparametric coordinates of the integration points are given by ξ and η . The factor α_h is a modification factor which is equal to one for quadratic elements and equal to $\sqrt{2}$ for linear elements, see Rots (1988). The equivalent length calculated with this formula is accurate when the mesh is not distorted too much and when most cracks are aligned with the mesh lines. For most practical applications the formulation for the equivalent length,

eq.(3.1), gives a good approximation.

The accumulated damage in the material will be represented by an internal parameter κ which is assumed to be determined by the inelastic work using a work-hardening hypothesis. The inelastic work rate \dot{W}_c is defined by

$$\dot{W}_c = \boldsymbol{\sigma}^T \dot{\boldsymbol{\varepsilon}}_c = \bar{\sigma}(\kappa) \dot{\kappa} \quad (3.2)$$

in which $\dot{\boldsymbol{\varepsilon}}_c$ the inelastic strain rate vector and $\bar{\sigma}(\kappa)$ an equivalent stress as a function of the internal parameter κ . The inelastic work g_f is then defined by the integral

$$g_f = \int_{\tau=0}^{\tau=\infty} \dot{W}_c d\tau = \int_{\kappa=0}^{\kappa=\infty} \bar{\sigma}(\kappa) d\kappa \quad (3.3)$$

Assuming that the inelastic work g_f is uniformly distributed over the equivalent length, the relation between the fracture energy G_f and the work g_f is given by

$$g_f = \frac{G_f}{h} \quad (3.4)$$

This results in a material model which is related to the energy which has to be dissipated due to the irreversible damage in the material. The concept of an equivalent length has been used extensively in the analysis of concrete structures. In this study, this concept will also be used to model the compressive softening behavior of concrete, although it is recognized that this mechanism is perhaps more related to the volume of the elements than to a representative length of the elements.

The nonlinear material behavior is now completely governed by an assumed equivalent stress - internal parameter relation, the $\bar{\sigma} - \kappa$ relation, which will be discussed in the next paragraph for both tension and compression.

3.2 Uniaxial behavior of plain concrete

The design of concrete structures is usually based on a grade of concrete which corresponds to a specific value of the characteristic compressive strength f_{ck} , which is determined with compressive tests on concrete cylinders 150 [mm] in diameter and 300 [mm] in height, see CEB-FIP model code (1990). A characteristic stress-displacement diagram for concrete loaded in compression is shown in Figure 3.1. For purposes of simulation and for an estimate of other concrete properties, the mean value of the compressive strength f_{cm} is needed, which is estimated by, see CEB-FIP model code (1990),

$$f_{cm} = f_{ck} + 8 \text{ [N/mm}^2\text{]} \quad (3.5)$$

The initial behavior of concrete is modeled using a linear-elastic constitutive model

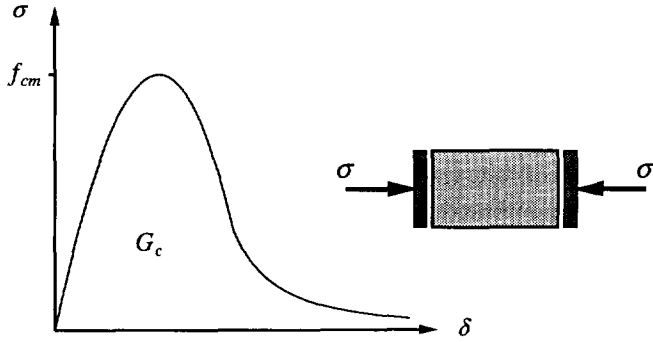


Figure 3.1 Concrete specimen under uniaxial compressive loading.

which is completely defined by the Young's modulus and the Poisson ratio. The Young's modulus of concrete is defined as the initial slope of the stress-strain diagram and depends on the compressive strength and on the type of aggregate. For normal weight concrete the Young's modulus can be estimated from the CEB-FIP model code (1990) recommendation

$$E_c = 10^4 f_{cm}^{1/3} [N/mm^2] \quad (3.6)$$

The Poisson ratio ranges from 0.1 to 0.2. In this study a value of the Poisson ratio equal to 0.15 will be used. Concrete loaded in compression behaves linear-elastically up to approximately 30 % of the compressive strength and upon further loading a gradual decrease of the stiffness is observed. If the deformation continues after the maximum compressive stress, the slope becomes negative and the descending branch of the stress-deformation curve characterizes the softening behavior of the concrete. The compression softening behavior of a concrete specimen is highly dependent upon the boundary conditions in the experiments and the size of the specimen, Van Mier (1984) and Vonk (1992). It is nevertheless assumed in this study that the compressive softening of concrete can be represented by a compressive fracture energy, denoted as G_c , which is assumed to be a material parameter. With this energy-based approach the compressive and tensile softening can be described within the same context which is plausible, because the underlying failure mechanisms are identical, viz. continuous crack growth at micro-level. Experimental data of the compressive fracture energy have been provided by Vonk (1992) who distinguishes a local compressive fracture energy which is constant and a continuum compressive fracture energy which is increasing with increasing specimen height. The total compressive fracture energy which has been found in the experiments ranges from 10 to 25 [Nmm/mm^2] which is about 50-100 times the tensile fracture energy.

The compressive stress-strain behavior has been approximated by different

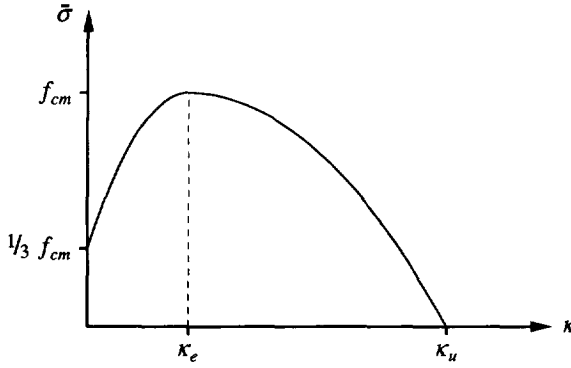


Figure 3.2 Compression softening model

functions, see e.g. Vecchio and Collins (1982), CEB-FIP model code (1990), but these relations are usually no energy-based formulations. In this study, the compressive constitutive model will be modeled either with ideal plastic behavior or with a compression softening model given by a parabolic equivalent stress-equivalent strain diagram according to Figure 3.2, which has been modified for the fracture energy-based model. The formulation of the equivalent stress reads

$$\bar{\sigma} = \begin{cases} \frac{f_{cm}}{3} \left(1 + 4 \frac{\kappa}{\kappa_e} - 2 \frac{\kappa^2}{\kappa_e^2} \right) & \text{if } \kappa < \kappa_e \\ f_{cm} \left(1 - \frac{(\kappa - \kappa_e)^2}{(\kappa_u - \kappa_e)^2} \right) & \text{if } \kappa_e \leq \kappa < \kappa_u \end{cases} \quad (3.7)$$

The maximum compressive strength will be reached at an equivalent strain κ_e which is determined irrespective of element size or compressive fracture energy and reads

$$\kappa_e = \frac{4 f_{cm}}{3 E_c} \quad (3.8)$$

The maximum equivalent strain κ_u is related to the compressive fracture energy and the element size and reads

$$\kappa_u = 1.5 \frac{G_c}{h f_{cm}} - \frac{11}{48} \kappa_e \quad (3.9)$$

The pre-peak energy has been taken into account with the correction factor $\frac{11}{48} \kappa_e$ in eq.(3.9). A possible snap-back on constitutive level if the equivalent length becomes too large, has been avoided by the assumption that the ultimate equivalent strain κ_u is

limited by

$$\kappa_u \geq 1.75 \kappa_e \quad (3.10)$$

It is noted that the limiting case $\kappa_u = 1.75 \kappa_e$ results in a steep descending branch after maximum stress.

The tensile strength of concrete is in accordance with the CEB-FIP model code (1990) related to the compressive strength. For the simulations performed in this study, the characteristic value of the tensile strength has been estimated by the CEB-FIP model code (1990) relationship

$$f_{ct,m} = 0.30 f_{ck}^{2/3} [N/mm^2] \quad (3.11)$$

A characteristic stress-deformation curve for concrete subjected to tensile loading is shown in Figure 3.3. Up to approximately 90 % of the maximum tensile load, the concrete behaves as a linear-elastic material. Then a macro-crack starts to develop and the stiffness reduces rapidly until the macro-crack cannot transfer any stress anymore. The released energy is then determined by the area under the stress-displacement diagram, which is equal to the fracture energy times the crack area. The fracture energy G_f is assumed to be a material parameter and is related to the compressive strength of the material f_{cm} and the maximum aggregate size d_{max} , according to the CEB-FIP model code (1990) recommendations which reads

$$G_f = 10^{-3} \alpha_F f_{cm}^{0.7} [Nmm/mm^2] \quad (3.12)$$

with the value of α_F given by Table 3.1.

Table 3.1 Coefficients α_F for an estimate of G_f (CEB-FIP model code)

$d_{max} [mm]$	α_F
8	4
16	6
32	10

The material model up to the tensile strength $f_{ct,m}$ is assumed to be given by a linear-elastic model. The material model for tensile behavior after the tensile strength has been violated is depicted in Figure 3.4 as an equivalent stress - equivalent strain diagram. The post-peak response is governed by the tensile fracture energy and the equivalent length. The tensile stress-strain relationship has been approximated by different functions, see e.g. CEB-FIP model code (1990), Hordijk (1991), and is one of the relevant features of the nonlinear tensile behavior of plain concrete, Rots (1988). In this study

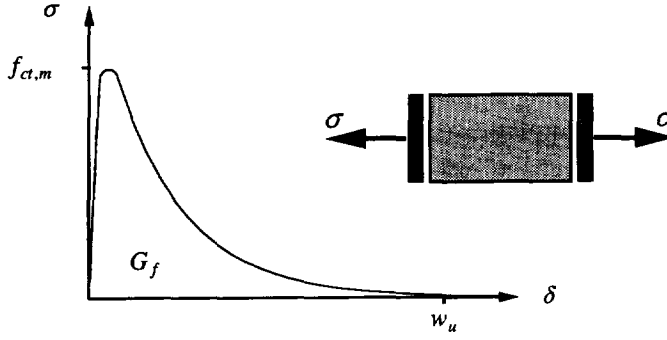


Figure 3.3 Concrete specimen under uniaxial tensile loading.

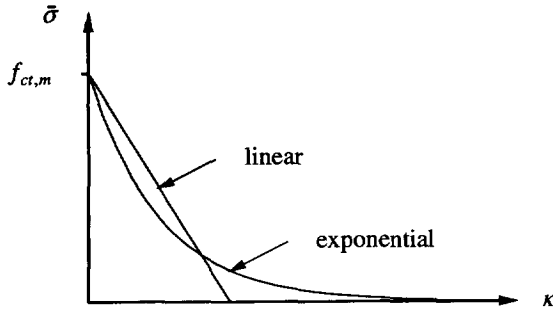


Figure 3.4 Tension-softening models

two different softening diagrams will be used, the linear and exponential diagram. For linear softening the equivalent stress as a function of the internal damage parameter κ is given by

$$\bar{\sigma} = f_{ct,m} \left(1 - \frac{\kappa}{\kappa_u} \right) \quad (3.13)$$

and for exponential softening

$$\bar{\sigma} = f_{ct,m} \exp(-\kappa / \kappa_u) \quad (3.14)$$

The ultimate damage parameter κ_u is calculated by

$$\kappa_u = k \frac{G_f}{h f_{ct,m}} \quad (3.15)$$

with $k = 2$ for linear softening and $k = 1$ for exponential softening. The parameter κ_u is assumed constant during the analysis and is considered to be an *element-related*

material property which can be calculated from the material properties, the tensile strength, the fracture energy and the element area represented by the equivalent length. The tensile fracture energy will be released in an element if the tensile strength is violated and the deformations localize in the element. With this approach the results which are obtained with the analysis are objective with regard to mesh refinement. It is however possible that the equivalent length of an element results in a snap-back in the constitutive model and the concept of objective fracture energy which has been assumed is no longer satisfied. In this case the strength limit has to be reduced in order to obtain an objective fracture energy by a sudden stress drop, resulting in brittle fracture, see Rots (1988). The condition of a maximum equivalent length is given by

$$h \leq k \frac{G_f E}{f_{ct,m}^2} \quad (3.16)$$

If the condition of eq.(3.16) is violated, the tensile strength is reduced to

$$f_{ct,m} = \left(k \frac{G_f E}{h} \right)^{1/2} \quad (3.17)$$

3.3 Biaxial behavior of plain concrete

The constitutive behavior of concrete under biaxial states of stress is different from the constitutive behavior under uniaxial loading conditions. The influence of the biaxial stress state has been investigated up to peak stress to provide a biaxial failure criterion, where it becomes evident that the tensile strength of concrete is influenced by the lateral stress state. The experimental data of concrete subjected to proportional biaxial loading is shown in Figure 3.5, Kupfer and Gerstle (1973). The maximum compressive strength increases approximately 16 % under conditions of equal biaxial compression, and about 25 % increase is achieved at a stress ratio of $\sigma_1 / \sigma_2 = 0.5$. A lateral compressive stress decreases the tensile strength, which can be explained that a lateral compressive stress introduces tensile stresses at the micro-level due to the heterogeneity of the material, which increases the process of internal damage, Vonk (1992). A lateral tensile stress has no major influence on the tensile strength. The increase in the compressive strength under biaxial compression can be explained by internal friction and aggregate interlock. The failure envelop which can be derived from the data of Kupfer and Gerstle is also valid for nonproportional loading because the strength envelop seems to be largely independent of the loading path, Nelissen (1972), which confirms the notion that softening due to compressive or tensile external loadings has the same underlying failure mechanism, i.e. continuous crack growth at the microlevel. Experimental data on the softening behavior of concrete under biaxial stress conditions is scarce but there is a

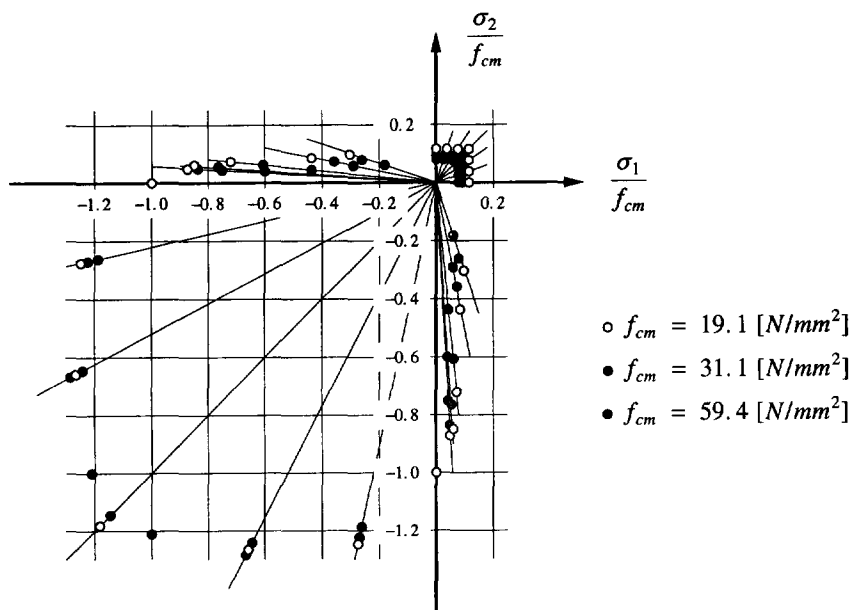


Figure 3.5 Biaxial strength of plain concrete, Kupfer and Gerstle (1973)

consensus of opinion that the softening of concrete is influenced by a biaxial stress state. For a multi-axial stress state it has been shown that softening is very sensitive for a confining pressure but in a biaxial stress state the concrete can always fail in the third direction which reduces the sensitivity of the softening to the confining pressure compared with the triaxial experiments, Vonk (1992).

3.4 Uniaxial behavior of reinforced concrete

The uniaxial compressive behavior of reinforced concrete is usually modeled with the compressive material model for plain concrete which has been discussed previously.

The tensile behavior of reinforced concrete is not fundamentally different from plain concrete and is also governed by cracking in the concrete. A characteristic stress-displacement diagram of a tension test is depicted in Figure 3.6. The existing cracks at the micro-level localize in a narrow band and a number of primary macro-cracks will develop. But due to bond between concrete and reinforcement, a gradual redistribution of internal forces from concrete to reinforcement is possible under the formation of secondary cracks until a stabilized crack pattern has developed. It is clear that the stiffness of the tension member is increased with reference to the reinforcing bar by the stiffness of the concrete. This effect is usually referred to in the literature as the tension-stiffening

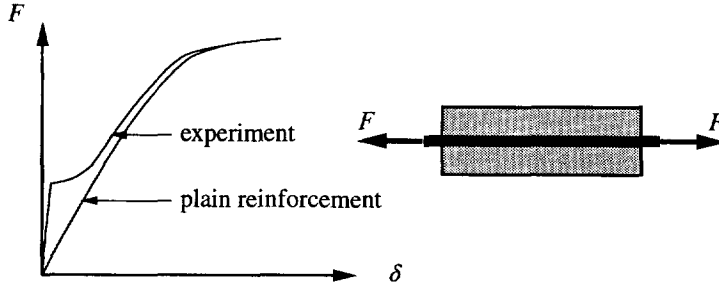


Figure 3.6 Reinforced concrete tensile member.

effect. Different formulations have been put forward for this tension-stiffening phenomenon, but in most formulations no reference has been made to the fracture energy which is actually released in the material.

The total amount of released energy at stabilized cracking is determined by the fracture energy of a single crack G_f and the average crack spacing l_s . The transition between plain and reinforced concrete can be obtained by assuming that the released energy is equal to the fracture energy of the material if the average crack spacing is equal to infinity. In general, the dimensions of the finite elements in simulations of reinforced concrete structures, and thus the equivalent length h , are much larger than the average crack spacing, l_s , and therefore it is assumed that the released energy can be determined by

$$G_f^{rc} = G_f \left(1 + \frac{h}{l_s} \right) \quad (3.18)$$

with G_f the fracture energy of a single crack, h the equivalent length and l_s the average crack spacing. This average crack spacing is a function of the bar diameter, the concrete cover and the reinforcement ratio according to the CEB-FIP model code (1990), which reads

$$l_s = 2/3 l_{s,max} = 2/3 \left(2 s_0 + \frac{\phi_s}{\alpha \rho_s} \right) \quad (3.19)$$

with s_0 the minimum bond length, ϕ_s the diameter of the reinforcement, a factor α equal to four for deformed bars and α equal to two for plain bars and the reinforcement ratio ρ_s given by

$$\rho_s = \frac{A_s}{A_c} \quad (3.20)$$

with A_s the total area of reinforcement and A_c the cross area of the tensile member. The minimum bond length s_0 is usually taken equal to 25 [mm] in the absence of more

precise data. A comparison of 132 experiments on tensile members, Braam (1990), showed that the average crack spacing given by eq.(3.19) is a good approximation of the experimentally observed crack spacing.

The formulas given in the previous paragraph are all related to the crack spacing in reinforced tensile members. Now, attention will be focused on the approximation of the released energy in plane two-dimensional structures like panels, reinforced with a reinforcing grid in two orthogonal directions. The crack spacing in panels is usually determined by treating a panel as a tensile member by the definition of an effective reinforcement ratio. If the reinforcement is supplied with a layer of a reinforcing grid, the average crack spacing is calculated with a modified expression of eq.(3.19),

$$l_s = 2/3 l_{s,max} = 2/3 (2 s_0 + \frac{\phi_s}{\alpha \rho_{s,eff}}) \quad (3.21)$$

with the effective reinforcement ratio $\rho_{s,eff}$ determined by

$$\rho_{s,eff} = \frac{A_s}{A_{c,eff}} \quad (3.22)$$

The effective tension area, $A_{c,eff} = h_{eff} b$, is estimated according to the CEB-FIP recommendations with the relation

$$h_{eff} = \min \left\{ 2.5 \left(c + \frac{\phi_{eq}}{2} \right) , \frac{t}{2} \right\}$$

with c the concrete cover on the reinforcement, ϕ_{eq} the equivalent bar diameter of the reinforcement and t the thickness of the structure. These geometrical properties are shown in Figure 3.7. The effective tension area is calculated with the equivalent bar diameter of the reinforcing grid which is determined by

$$\phi_{eq} = \frac{\phi_p \rho_p + \phi_q \rho_q}{\rho_p + \rho_q} \quad (3.23)$$

with the reinforcement ratios ρ_p and ρ_q in the p - and q -directions of the reinforcing grid, respectively. The diameter of the reinforcement is given by ϕ_p and ϕ_q in the p - and q -direction. The average crack spacing can now be calculated in the two directions of the reinforcing grid. The crack spacing given by eq.(3.21) is based on the fact that the cracks form at right angles to the reinforcing direction. When the cracks form at inclined angles with the reinforcing directions this identity cannot be used to estimate the crack spacing. In these cases, the average crack spacing is calculated with the following expression according to the CEB-FIP model code (1990),

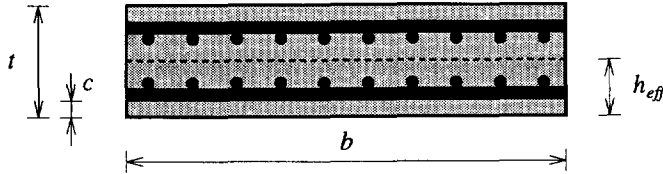


Figure 3.7 Concrete slab with two layers of reinforcement. Effective tension area according to CEB-FIP model code.

$$l_s = \left(\frac{|\cos \alpha|}{l_{s,p}} + \frac{|\sin \alpha|}{l_{s,q}} \right)^{-1} \quad (3.24)$$

where α denotes the angle between the reinforcement in the p -direction and the direction of the principal tensile stress at incipient cracking. The crack spacings predicted with eq.(3.24) are theoretically reasonable. For a structure reinforced equally in the p - and q -directions subjected to a pure shear loading, the cracks are forming at 45° to the p -direction and the crack spacing is $\frac{1}{2}\sqrt{2}$ times the crack spacing in the p - or q -direction. If the structure is only reinforced in the p -direction, the crack spacing for tension in the p -direction is equal to the value given by eq.(3.21). For tension in the q -direction the predicted crack spacing is equal to infinity, which implies that only one crack is formed in the structure. Comparison of the theoretical crack spacing with the experimental results of one-directionally reinforced structures shows that the trend of the crack spacing with increasing angle α is predicted correctly, but that the crack spacing is usually underestimated, Bhude and Collins (1987). This is due to the fact that only primary cracks have been observed with the secondary cracks being ignored. The expression of eq.(3.24) may be used according to the CEB-FIP model code (1990) when a more advanced model is not available.

As indicated in Figure 3.7, the reinforcement is usually applied in more layers with an arbitrary direction through the thickness of the structure. The average crack spacing of the structure is then determined by the smallest average crack spacing of all reinforcing grids. The average crack spacing in the case of different reinforcing grids with arbitrary directions will be given by a modification of eq.(3.24),

$$l_s = \left(a_x + a_y \right)^{-1} \quad (3.25)$$

in which the factors a_x and a_y are determined by

$$a_x = \max\left(\frac{|\cos \alpha_j|}{l_{s,pj}}\right)$$

$$a_y = \max\left(\frac{|\sin \alpha_j|}{l_{s,qj}}\right)$$

$$j = 1, \dots, n_{grid} \quad (3.26)$$

with α_j the angle between the reinforcement p -direction and the direction of the principal tensile stress at incipient cracking. It has tacitly been assumed that the cracks propagate through the entire thickness of the structure with no localization in the thickness direction. With this approach, the fracture energy in reinforced concrete can be assessed on the basis of the fracture energy of concrete, the reinforcement properties and the angle between reinforcement and the principal stress at incipient cracking. In this fashion, the tension-softening of reinforced concrete has been formulated in a rational fashion.

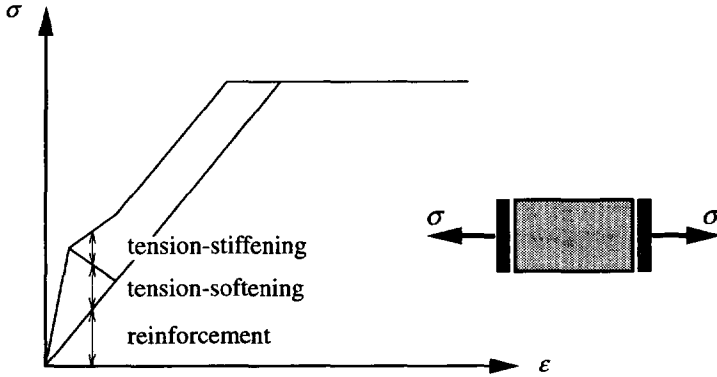


Figure 3.8 Constitutive model of reinforced concrete. Schematical representation.

After a stabilized crack pattern has developed, stresses are still transferred from reinforcement to concrete between the cracks due to the bond action which increases the total stiffness of the structure, see Figure 3.6. In this study it is therefore assumed that the behavior of cracked, reinforced concrete loaded in tension can be considered as the superposition of the stiffness of plain concrete, a stiffness of the reinforcement and an additional stiffness due to bond between concrete and reinforcement which is referred to as the tension-stiffening component. This leads to the following summation of stress contributions

$$\sigma = \sigma_c + \sigma_s + \sigma_{ia} \quad (3.27)$$

with σ_c the stress contribution of the concrete, σ_s the contribution of the reinforcing steel, and σ_{ia} the interaction stress contribution due to tension-stiffening, see Figure 3.8.

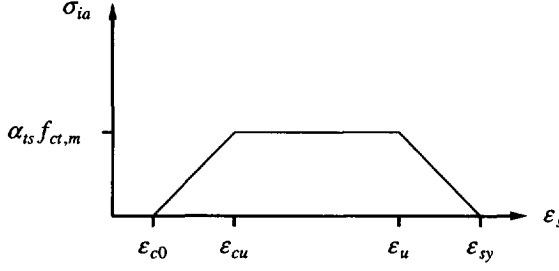


Figure 3.9 Tension-stiffening model.

The additional stress due to tension-stiffening is assumed to be given as a function of the strain in the direction of the reinforcement and will be active on the effective tension area defined in Figure 3.7. The interaction stress is assumed to be given by a tri-linear function according to Cervenka, Pukl and Eligehausen (1992) which is depicted in Figure 3.9. The interaction stress is only active if the strain in the reinforcement is larger than ϵ_{c0} which is determined by

$$\epsilon_{c0} = \frac{f_{ct,m}}{E_c} \cos^2 \alpha \quad (3.28)$$

with α the angle between the direction of the reinforcement and the direction of the principal stress at incipient cracking. The factor ϵ_{cu} is determined by the crack spacing, the equivalent length of the element and the fracture energy of the concrete and is given by

$$\epsilon_{cu} = k \cos^2 \alpha \frac{G_f^{rc}}{h f_{ct,m}} \quad (3.29)$$

with k equal to one for exponential softening and k equal to two for linear softening. The constant part of the diagram is a fraction of the tensile strength of the concrete with the factor α_{ts} as a rough approximation equal to the tensile strength, i.e. $\alpha_{ts} = 1.0$. The tension-stiffening component is reduced near the yield strain of the reinforcement ϵ_{sy} in order to avoid an artificial increase of the yield stress of the reinforcement. The strain at which the tension-stiffening component is reduced is given by

$$\epsilon_u = \epsilon_{sy} - \frac{\alpha_{ts} f_{ct,m}}{\rho_{s,eff} E_s} \quad (3.30)$$

This tri-linear function will be used in this study, but further research to the actual function is necessary.

3.5 Biaxial behavior of reinforced concrete

The biaxial failure surface of plain concrete is also applicable to reinforced concrete, because the reinforcement is usually not activated in the linear-elastic state. The tension-tension behavior is not affected by the biaxial stress state and will be modeled with the uniaxial behavior in both directions. The compression-compression behavior will also be modeled with the uniaxial model. The compression-tension behavior of reinforced concrete is usually modified after cracking, because it is assumed that the compressive strength of concrete is affected by cracking in the lateral direction. Vecchio and Collins (1982) analyzed the results of their experiments and found that the compressive strength should be reduced as a function of the lateral tensile strain down to 20 %. The large discrepancy between the proposal of Vecchio and Collins and the usual reduction up to 20 %, see for an extensive literature survey Kollegger and Mehlhorn (1990a), was the starting point of a comprehensive experimental study by Kollegger and Mehlhorn at the University of Kassel. The experimental study concerned 47 panels with dimensions $500 \times 1000 \text{ [mm}^2\text{]}$ and a thickness of 100 [mm] loaded in a tension-compression state, see Figure 3.10.

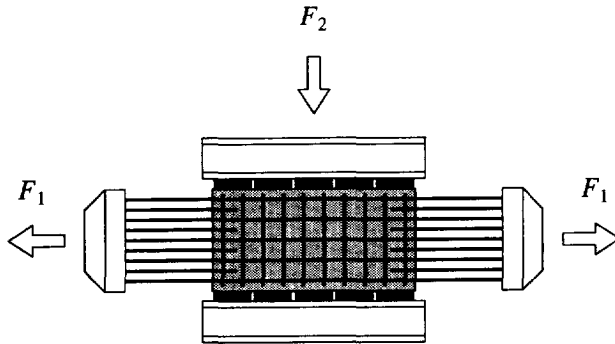


Figure 3.10 Experiment Kollegger and Mehlhorn (1990a).

The study concerned five series of tests with different reinforcement geometry and reinforcement directions. An influence of the reinforcement properties could not be determined in the study, and a reduction of the compressive strength up to 20 % as a function of the transverse tensile stress was proposed. The experimental results of all panels are given in Figure 3.11 in which the compressive strength of the panels is plotted against the lateral stress. It is clear that the stresses in the panels are compressive in the direction of the tensile loading. These compressive stresses result from prevented lateral strain by the reinforcement in the tensile direction and is calculated by

$$\sigma_1 = \frac{F_1}{A_c} - \sigma_s(\varepsilon_1) \cdot \rho_1$$

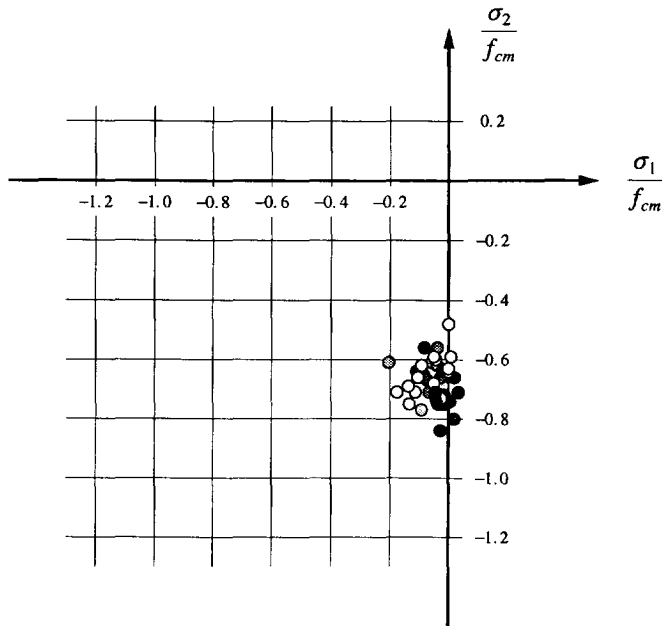


Figure 3.11 Biaxial strength of reinforced concrete, Kollegger and Mehlhorn (1990a).

with F_1 the tensile force, A_c the concrete area and σ_s the stress in the reinforcement as a function of the strain component ε_1 which is measured on the panel surface. The reinforcement ratio in the lateral direction is denoted by ρ_1 . However, when Figure 3.11 is examined in more detail, it is not obvious that the compressive strength is a function of the transverse stress, since we observe a constant reduction of the compressive strength. If the compressive strength is depicted as a function of the transverse strain, see Figure 3.12, it is even more pronounced that a reduction of the compressive strength as a function of the lateral strain cannot be observed, but that the apparent compressive strength of the panels is approximately 70 % of the mean compressive strength. The compressive strength has been determined with compression tests on concrete cubes $200 \times 200 \times 200 \text{ [mm}^3\text{]}$ and the differences between the cube compressive strength and the apparent compressive strength of the panels has been explained by Kollegger and Mehlhorn as the influence of the manufacturing of the panels, eccentricities and the non-linear relation between the mean compressive strength and the biaxial stress state in the panels. The compressive strength of two panels which have been loaded in compression without tensile loading have been given with a solid dot in Figures 3.11 and 3.12. These two panels have been reinforced only by four rebars with a diameter of 6.5 [mm] in the corners and also for these two panels a reduction of the compressive strength is observed of approximately 70 %. These panels can be considered as plain concrete and it is obvious that also for these panels the apparent compressive strength is reduced when compared with the cube compressive strength. A possible explanation for this

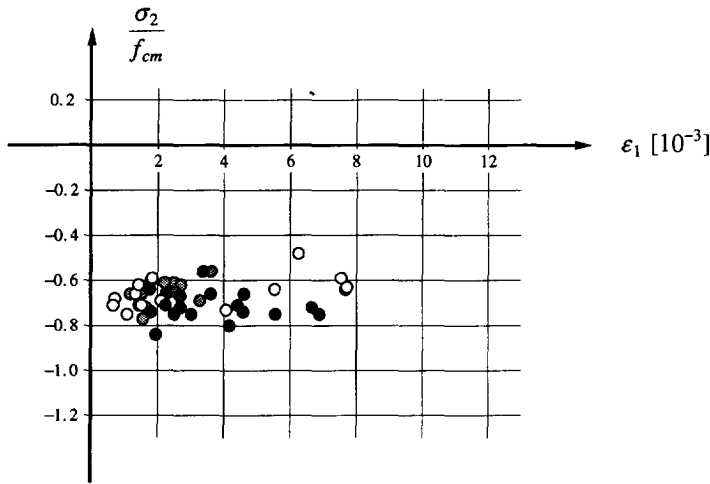


Figure 3.12 Compressive strength as a function of the transverse strain, Kollegger and Mehlhorn (1990a).

phenomenon is that the compressive strength of concrete is highly influenced by the boundary conditions and the size of the specimen, see van Mier (1984), Vonk (1992). The size effect and the effect of the boundary conditions should result in a constant reduction of the compressive strength of all panels with or without reinforcement which is indeed observed. Further investigations should give more insight in the mechanisms of strength reduction, size effect and boundary conditions in compressive tests. For the moment it is assumed in this study that the compressive strength of concrete is reduced by a constant factor of approximately 20 %.

3.6 Summary

The failure mechanism of concrete loaded in tension or compression is essentially the same, viz. crack growth at the microlevel of the material. The experimental results of triaxial test show a clear transition point between the brittle failure mechanism which is associated with cracking, and a ductile failure mechanism which is associated with crushing. But in biaxial tests, these failure mechanisms are not clear because the material can fail in the unconstrained direction which prevents a ductile behavior of concrete in compression. However, it is assumed that two failure mechanisms can be distinguished, one associated with a localized fracture process and one associated with a more distributed fracture process which can be termed as crushing of the material. It is assumed that the internal damage due to these failure mechanisms can be represented with two internal parameters κ_C and κ_T for damage in compression and tension respectively, which are in general related to the inelastic strain.

The behavior of plain and reinforced concrete in tension is governed by the same

failure mechanism but the total internal damage in concrete with reinforcement is in general larger because of the formation of secondary cracks. It is assumed that the increase of the internal damage can be estimated by the average crack spacing which is a function of the reinforcement properties. It is also assumed that the behavior in compression of plain and reinforced concrete can be modeled with the same approach. The reduction of the compressive strength of reinforced concrete due to cracks in the lateral direction could not be observed, but the compressive strength will be reduced with a constant factor which reflects the effect of different boundary conditions and the size effect.

The formulation of the constitutive model for plain concrete which will be developed in the next Chapter should have the ability to model the damage in the material with internal parameters, which are in general functions of the inelastic strain. These inelastic strains result from a dissipative process in which fracture energy is released during the process of internal fracture.

4. MODELING OF PLAIN CONCRETE

The mathematical description of material behavior is commonly named a constitutive model. In this study, two different types of constitutive models will be used for the description of plain concrete, firstly constitutive models based on an incremental or a rate formulation, and secondly constitutive models based on a total formulation. The advantages of the first model are that the model allows for a transparent combination with other nonlinear phenomena, such as creep, shrinkage and thermal loading, and that it incorporates path-dependent behavior which allows for non-proportional loading. The advantage of the second model is the conceptual simplicity.

A well established incremental formulation is the fixed multi-directional crack model, De Borst and Nauta (1985), Rots (1988), which allows for a number of non-orthogonal cracks. In this model, a crack is formed perpendicular to the direction of the major principal stress if this stress violates the tensile strength. After the first crack, another crack is allowed to form if the tensile strength is again violated by the major principal stress, and if the angle between the existing crack and the direction of the major principal stress exceeds a certain value, the threshold angle. Usually, this threshold angle is set equal to 30° which implies a maximum number of cracks which are allowed to form of six. However, numerical difficulties have been reported when state changes occur, Crisfield and Wills (1987). To analyze structures which are in a state of compression-tension, e.g. shear wall panels, the crack model can be combined with a plasticity model to describe crack formation and plasticity, De Borst and Nauta (1985), but this combination has been reported to result in numerical difficulties, Wang, Van der

Vorm and Blaauwendraad (1990). Because the major goal of this study is the development of stable numerical tools to analyze reinforced concrete structures, a different model has been formulated to solve both the problem of overestimation of the failure load with the fixed smeared crack model, Rots (1988), and the numerical problems in the tension-compression region. A constitutive model has been developed which describes the formation of cracks within the framework of plasticity. The theory of plasticity is well established and sound numerical algorithms have been developed, see for instance Simo, Kennedy and Govindjee (1988).

The rotating crack model is usually presented in a total strain formulation, see Willam, Pramono and Sture (1987), and this model has been used in the analyses of reinforced concrete structures, Crisfield and Wills (1987), Kollegger (1988). If the Poisson effect is neglected after cracking, the model is probably the most appealing approach for engineers to describe the nonlinear behavior of concrete in tension and compression. A nonlinear compressive behavior is easily implemented in such model, because the algebraic formulation can be extended with a compressive branch. The second model within a total strain formulation which will be considered is the Rankine yield criterion based on the deformation theory of plasticity. This model will be discussed merely to show the analogy with the rotating crack model, because it is difficult to modify the Rankine model based on a deformation theory to allow for unloading. Even for monotonic proportional loading, local unloading is possible on integration point level, and for this reason the deformation plasticity model is not considered as an alternative for the rotating crack model.

4.1 Incremental formulations

A constitutive model formulated in an incremental form gives the possibility to model the history of the material implicitly with the definition of internal variables. If an additive decomposition of the strain rate vector $\dot{\epsilon}$ is assumed into an elastic, reversible part $\dot{\epsilon}_e$ and an inelastic, irreversible part $\dot{\epsilon}_c$,

$$\dot{\epsilon} = \dot{\epsilon}_e + \dot{\epsilon}_c \quad (4.1)$$

the basic formulation is given. The elastic strain rate vector determines the stress rate vector through the elastic stiffness matrix D_e

$$\dot{\sigma} = D_e \dot{\epsilon}_e \quad (4.2)$$

The evolution of the inelastic strain is dependent upon the assumption of the constitutive model and is in general a function of the stress and strain vector and the internal variables. The inelastic strain will now be determined with an incremental formulation based on the flow theory of plasticity.

A fundamental notion of plasticity theory is the existence of a yield function

$$f(\boldsymbol{\sigma}, \boldsymbol{\eta}, \mathbf{q}) = 0 \quad (4.3)$$

which depends on the stress vector $\boldsymbol{\sigma}$, the back-stress vector $\boldsymbol{\eta}$, which allows for a kinematic hardening behavior, and on a number of scalar-valued internal variables, conveniently collected in a vector \mathbf{q} . The evolution of the inelastic strain rate is given by the associated flow rule

$$\dot{\boldsymbol{\varepsilon}}_c = \dot{\lambda} \partial_{\boldsymbol{\sigma}} f \quad (4.4)$$

where the notation $\partial_{\boldsymbol{\sigma}} f$ is used to denote the derivative of the yield function f with respect to the stress vector $\boldsymbol{\sigma}$. The rate of the inelastic multiplier $\dot{\lambda}$ has to comply with the Kuhn-Tucker conditions

$$\dot{\lambda} \geq 0$$

$$f \leq 0 \quad (4.5)$$

$$\dot{\lambda} f = 0$$

The evolution of the back stress is assumed to be given by a generalization of Prager's kinematic hardening rule with the direction of the back stress rate determined by a loading function g

$$\dot{\boldsymbol{\eta}} = (1 - \gamma) E_k \dot{\lambda} \partial_{\boldsymbol{\sigma}} g \quad (4.6)$$

in which E_k the kinematic tangential hardening modulus and γ the proportion of isotropic and kinematic hardening, $\gamma = 0$ implying full kinematic hardening and $\gamma = 1$ setting the other limiting case of pure isotropic hardening. The evolution of the internal variable vector is assumed to be given by a general evolutionary equation

$$\dot{\mathbf{q}} = \dot{\lambda} \mathbf{h}(\boldsymbol{\sigma}, \boldsymbol{\eta}, \mathbf{q}) \quad (4.7)$$

The evolution equations given above can be regarded as strain driven in the sense that the total strain vector, the inelastic strain vector and the internal variables are known at time t and that the incremental strain vector $\Delta \boldsymbol{\varepsilon}^{(i+1)}$ follows from the loading regime. The basic problem in computational elasto-plasticity is that the elasto-plastic constitutive equations have to be updated in a consistent manner

$$(\boldsymbol{\sigma}^t, \boldsymbol{\varepsilon}^t, \boldsymbol{\eta}^t, \mathbf{q}^t; \Delta \boldsymbol{\varepsilon}^{(i+1)}) \rightarrow (\boldsymbol{\sigma}^{t+\Delta t}, \boldsymbol{\varepsilon}^{t+\Delta t}, \boldsymbol{\eta}^{t+\Delta t}, \mathbf{q}^{t+\Delta t})$$

By applying the fully implicit Euler backward algorithm this problem is transformed into a constrained optimization problem governed by discrete Kuhn-Tucker conditions as shown by Simo, Kennedy and Govindjee (1988). It has been shown in different

studies, e.g. Krieg and Krieg (1977), Schreyer, Kulak and Kramer (1979), Ortiz and Popov (1985), Simo and Taylor (1986), that the implicit Euler-backward algorithm is stable and accurate for J_2 -plasticity. But even when the yield surface is highly distorted the Euler-backward algorithm is unconditionally stable, Ortiz and Popov (1985), and accurate, De Borst and Feenstra (1990), Schellekens and De Borst (1991). Application of the Euler-backward algorithm results in a discrete set of equations

$$\begin{aligned}
 \boldsymbol{\varepsilon}^{(i+1)} &= {}^t\boldsymbol{\varepsilon} + \Delta\boldsymbol{\varepsilon}^{(i+1)} \\
 \boldsymbol{\sigma}^{(i+1)} &= \mathbf{D}_e (\boldsymbol{\varepsilon}^{(i+1)} - \boldsymbol{\varepsilon}_c^{(i+1)}) \\
 \boldsymbol{\varepsilon}_c^{(i+1)} &= {}^t\boldsymbol{\varepsilon}_c + \Delta\lambda^{(i+1)} \partial_{\boldsymbol{\sigma}} f^{(i+1)} \\
 \mathbf{q}^{(i+1)} &= {}^t\mathbf{q} + \Delta\lambda^{(i+1)} \mathbf{h}^{(i+1)} \\
 \boldsymbol{\eta}^{(i+1)} &= {}^t\boldsymbol{\eta} + \Delta\lambda^{(i+1)} (1 - \gamma) E_{ks} \partial_{\boldsymbol{\sigma}} g^{(i+1)}
 \end{aligned} \tag{4.8}$$

with E_{ks} the secant hardening modulus. The superscript $t + \Delta t$ has been dropped for convenience. The discrete Kuhn-Tucker conditions are given by

$$\begin{aligned}
 \Delta\lambda^{(i+1)} &\geq 0 \\
 f(\boldsymbol{\sigma}^{(i+1)}, \boldsymbol{\eta}^{(i+1)}, \mathbf{q}^{(i+1)}) &\leq 0 \\
 \Delta\lambda^{(i+1)} f(\boldsymbol{\sigma}^{(i+1)}, \boldsymbol{\eta}^{(i+1)}, \mathbf{q}^{(i+1)}) &= 0
 \end{aligned} \tag{4.9}$$

Because the algorithm is considered within an elastic predictor-plastic corrector algorithm an elastic trial state is introduced as

$$\begin{aligned}
 \boldsymbol{\varepsilon}_E &= {}^t\boldsymbol{\varepsilon}_e + \Delta\boldsymbol{\varepsilon}^{(i+1)} \\
 \boldsymbol{\sigma}_E &= \mathbf{D}_e \boldsymbol{\varepsilon}_E \\
 \boldsymbol{\eta}_E &= {}^t\boldsymbol{\eta} \\
 \mathbf{q}_E &= {}^t\mathbf{q}
 \end{aligned} \tag{4.10}$$

which can be obtained by freezing inelastic flow during the time step.

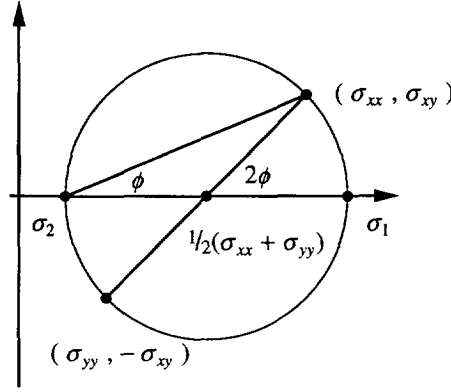


Figure 4.1 Mohr's circle.

4.1.1 The Rankine yield criterion

The maximum tensile stress criterion of Rankine can be used to determine the tensile strength of concrete. Consider a plane-stress situation in which the major principal stress σ_1 and the minor principal stress σ_2 are defined by means of a Mohr's circle, see Figure 4.1. The hardening behavior is assumed to be described by two internal variables κ_1 and κ_2 which govern the corresponding principal stresses. The yield functions are then given by the principal stress σ_j and an equivalent stress $\bar{\sigma}_j$ as a function of an internal variable κ_j according to

$$\begin{cases} f_1 = \sigma_1 - \bar{\sigma}_1(\kappa_1) \\ f_2 = \sigma_2 - \bar{\sigma}_2(\kappa_2) \end{cases} \quad (4.11)$$

The yield surface is depicted in Figure 4.2 in the principal stress space. The problem which occurs with the two yield functions is that the transformation between the stress space and the principal stress space has to be defined uniquely for two yield functions with different hardening models. This concept has been used in infinitesimal plasticity, Simo (1992), where it is assumed that the directions of the principal stresses in the trial elastic state coincide with the directions of the principal stresses in the final state. However, it is difficult to distinguish already in the trial state which principal stress will be the major and minor principal stress and the corresponding equivalent stresses $\bar{\sigma}_1$ and $\bar{\sigma}_2$ in the final state. This problem can probably be solved using a strain-based plasticity model, see e.g. Naghdi and Trapp (1975), which is formulated in the principal strain space. In this study the formulation will be given by a single stress-based function

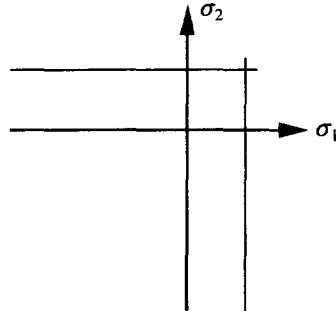


Figure 4.2 Rankine yield surface in the principal stress space.

which is governed by the first principal stress, and with an equivalent stress which describes the hardening behavior of the material. The assumption of isotropic hardening is not completely valid for a material such as concrete which can be loaded to the tensile strength even if in the perpendicular direction the stress has been reduced due to softening of the material. This problem can partially be solved using a kinematic hardening model in which the yield surface is shifted in the direction of the first principal stress.

In a plane-stress configuration the major principal stress will be expressed in terms of the stress vector with the aid of Mohr's circle. This results in a yield function with mixed hardening which reads

$$f = (1/2 \xi^T P \xi)^{1/2} + 1/2 \pi^T \xi - \bar{\sigma}(\gamma \kappa_T) \quad (4.12)$$

with the reduced stress vector $\xi = \sigma - \eta$ and the equivalent stress $\bar{\sigma}$ as a function of the internal parameter κ_T . The yield surface is depicted in Figure 4.3. The projection matrix P and the projection vector π are given by

$$P = \begin{bmatrix} 1/2 & -1/2 & 0 & 0 \\ -1/2 & 1/2 & 0 & 0 \\ 0 & 0 & 0 & 0 \\ 0 & 0 & 0 & 2 \end{bmatrix} \quad (4.13)$$

and

$$\pi = \{ 1, 1, 0, 0 \}^T \quad (4.14)$$

respectively. The equivalent stress $\bar{\sigma}(\gamma \kappa_T)$ is the uniaxial tensile strength which is assumed to be given by one of the tension-softening models given in eq.(3.13) and eq.(3.14). The incremental back-stress vector has been defined in eq.(4.8) as

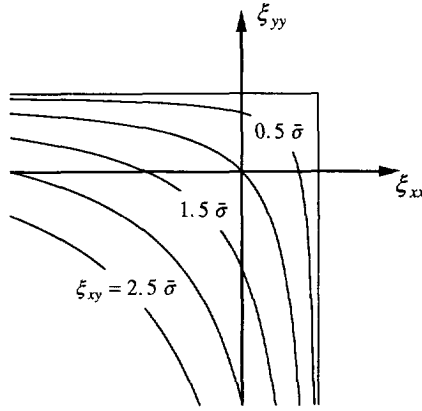


Figure 4.3 Rankine yield surface with iso-shear stress lines.

$$\Delta \eta = \Delta \lambda (1 - \gamma) E_{ks} \partial_{\sigma} g^{(i+1)}$$

in which the direction of the incremental back-stress vector is determined by the derivative of a loading function g with respect to the stress vector at the final stress. If it is assumed that the direction of the incremental back-stress vector is given by the major principal stress direction at the final stress, the loading function can be determined. Consider the following expression in which the stress vector σ is expressed as a transformation of the principal stress vector

$$\sigma = \begin{Bmatrix} \sigma_{xx} \\ \sigma_{yy} \\ \sigma_{zz} \\ \sigma_{xy} \end{Bmatrix} = \begin{bmatrix} \cos^2 \phi & \sin^2 \phi & 0 & -2 \sin \phi \cos \phi \\ \sin^2 \phi & \cos^2 \phi & 0 & 2 \sin \phi \cos \phi \\ 0 & 0 & 1 & 0 \\ \sin \phi \cos \phi & -\sin \phi \cos \phi & 0 & \cos^2 \phi - \sin^2 \phi \end{bmatrix} \begin{Bmatrix} \sigma_1 \\ \sigma_2 \\ \sigma_3 \\ 0 \end{Bmatrix}$$

which results in an expression of the stress vector in terms of the principal stresses and the angle ϕ

$$\sigma = \sigma_1 \begin{Bmatrix} \cos^2 \phi \\ \sin^2 \phi \\ 0 \\ \sin \phi \cos \phi \end{Bmatrix} + \sigma_2 \begin{Bmatrix} \sin^2 \phi \\ \cos^2 \phi \\ 0 \\ -\sin \phi \cos \phi \end{Bmatrix} + \sigma_3 \begin{Bmatrix} 0 \\ 0 \\ 1 \\ 0 \end{Bmatrix} \quad (4.15)$$

The direction of the incremental back stress vector is now assumed to be given by the direction vector which is related to the major principal stress σ_1 , so

$$\Delta \eta = \Delta \lambda (1 - \gamma) E_{ks} \begin{Bmatrix} \cos^2 \phi \\ \sin^2 \phi \\ 0 \\ \sin \phi \cos \phi \end{Bmatrix} \quad (4.16)$$

which can be expressed in terms of the gradient to the yield function $\partial_\sigma f$. The gradient of the yield surface is given by

$$\partial_\sigma f = \frac{\mathbf{P} \boldsymbol{\xi}}{2(\frac{1}{2} \boldsymbol{\xi}^T \mathbf{P} \boldsymbol{\xi})^{1/2}} + \frac{1}{2} \pi \quad (4.17)$$

which can be expressed in terms of the angle between the normal directions and the principal directions,

$$\partial_\sigma f = \begin{Bmatrix} \frac{1}{2} + \frac{1}{2} \cos 2\phi \\ \frac{1}{2} - \frac{1}{2} \cos 2\phi \\ 0 \\ \sin 2\phi \end{Bmatrix} = \begin{Bmatrix} \cos^2 \phi \\ \sin^2 \phi \\ 0 \\ 2 \sin \phi \cos \phi \end{Bmatrix} \quad (4.18)$$

The definition of the angles are given in Mohr's circle depicted in Figure 4.1. The derivative of the loading surface g with respect to the stress vector can be expressed in terms of the gradient to the yield function because

$$\begin{aligned} \partial_\sigma g &= \begin{Bmatrix} \cos^2 \phi \\ \sin^2 \phi \\ 0 \\ \sin \phi \cos \phi \end{Bmatrix} = \begin{bmatrix} 1 & 0 & 0 & 0 \\ 0 & 1 & 0 & 0 \\ 0 & 0 & 1 & 0 \\ 0 & 0 & 0 & 1/2 \end{bmatrix} \begin{Bmatrix} \cos^2 \phi \\ \sin^2 \phi \\ 0 \\ 2 \sin \phi \cos \phi \end{Bmatrix} \\ &= \boldsymbol{\Lambda}_M \partial_\sigma f \end{aligned} \quad (4.19)$$

The incremental back stress vector is finally given by

$$\Delta \eta = \Delta \lambda (1 - \gamma) E_{ks} \boldsymbol{\Lambda}_M \partial_\sigma f \quad (4.20)$$

which is a convenient formulation since the yield function and the loading function are equal.

It is assumed that the internal damage in the material is reflected in the internal parameter κ_T which is governed by a work-hardening hypothesis. For a work-hardening hypothesis the internal variable is determined by the inelastic work rate \dot{W}_c defined by

$$\dot{W}_c = \boldsymbol{\xi}^T \dot{\boldsymbol{\epsilon}}_c = \bar{\sigma}(\gamma \kappa_T) \dot{\kappa}_T \quad (4.21)$$

With the application of Euler's theorem this can be elaborated as

$$\dot{\kappa}_T = \dot{\lambda} \quad (4.22)$$

The assumption of a work-hardening hypothesis results in a linear relation between the inelastic multiplier $\dot{\lambda}$ and the internal parameter $\dot{\kappa}_T$ which has previously been defined by the general evolutionary equation, eq.(4.7), but can now be simplified as

$$\Delta \kappa_T^{(i+1)} = \Delta \lambda^{(i+1)} \quad (4.23)$$

in the case of the Rankine yield criterion.

The updated stress vector $\sigma^{(i+1)}$ and the updated back stress vector $\eta^{(i+1)}$ are obtained by substituting eqs.(4.10), (4.17) and (4.20) into the discrete set of equations, eq.(4.8). This results in a mapping procedure given by

$$\begin{cases} \sigma^{(i+1)} &= \sigma_E - \Delta \lambda^{(i+1)} \frac{D_e P}{2\Psi} \xi^{(i+1)} - 1/2 \Delta \lambda^{(i+1)} D_e \pi \\ \eta^{(i+1)} &= \eta_E + \Delta \lambda^{(i+1)} (1-\gamma) E_{ks} \frac{\Lambda_M P}{2\Psi} \xi^{(i+1)} + 1/2 \Delta \lambda^{(i+1)} (1-\gamma) E_{ks} \pi \end{cases}$$

with the denominator Ψ defined as

$$\Psi = (1/2 \xi^{(i+1)T} P \xi^{(i+1)})^{1/2} \quad (4.24)$$

The updated stress vector and the updated back-stress vector are now obtained by solving the following system of equations

$$\begin{Bmatrix} \sigma^{(i+1)} \\ \eta^{(i+1)} \end{Bmatrix} = \begin{bmatrix} A_{11} & A_{12} \\ A_{21} & A_{22} \end{bmatrix}^{-1} \begin{Bmatrix} \sigma_E - 1/2 \Delta \lambda^{(i+1)} D_e \pi \\ \eta_E + 1/2 \Delta \lambda^{(i+1)} (1-\gamma) E_{ks} \pi \end{Bmatrix} \quad (4.25)$$

with the matrices

$$A_{11} = I + \frac{\Delta \lambda^{(i+1)}}{2\Psi} D_e P$$

$$A_{12} = -\frac{\Delta \lambda^{(i+1)}}{2\Psi} D_e P$$

$$A_{21} = -\frac{\Delta \lambda^{(i+1)}}{2\Psi} (1-\gamma) E_{ks} \Lambda_M P$$

$$A_{22} = I + \frac{\Delta\lambda^{(i+1)}}{2\Psi} (1 - \gamma) E_{ks} \Lambda_M P$$

Eq.(4.24) for Ψ is not very convenient because the updated stress in eq.(4.25) is then not related linearly to the trial state. To arrive at a more suitable form we express the denominator Ψ in terms of the inelastic multiplier by pre-multiplication of $\sigma^{(i+1)}$ and $\eta^{(i+1)}$ with the vector π^T (cf. De Borst (1993)) which results in

$$\begin{cases} \pi^T \sigma^{(i+1)} = \pi^T \sigma_E - 1/2 \Delta\lambda^{(i+1)} \pi^T D_e \pi \\ \pi^T \eta^{(i+1)} = \pi^T \eta_E + 1/2 \Delta\lambda^{(i+1)} (1 - \gamma) \pi^T E_{ks} \pi \end{cases} \quad (4.26)$$

because $\pi^T D_e P = 0^T$. The denominator now reads

$$\begin{aligned} \Psi = & \bar{\sigma}(\gamma \kappa_T) - 1/2 \pi^T (\sigma_E - \eta_E) \\ & + 1/2 \Delta\lambda^{(i+1)} \left(\frac{E}{(1 + \nu)(1 - 2\nu)} + (1 - \gamma) E_{ks} \right) \end{aligned} \quad (4.27)$$

Now, Ψ is expressed solely in terms of the variables in the trial state and the inelastic multiplier. Accordingly, eq.(4.25) is a linear system of equations in the unknowns $\sigma^{(i+1)}$ and $\eta^{(i+1)}$.

The matrix defined in eq.(4.25) will henceforth be denoted as the mapping matrix. The calculation of the mapping matrix can result in numerical problems because the sub-matrices of the mapping matrix are calculated with a division by Ψ . This factor becomes equal to zero in the corner of the yield surface. If Ψ is equal to zero, the inverted mapping matrix is, however, still defined which can be shown if a spectral decomposition of the sub-matrices is applied, Simo and Taylor (1986), Matthies (1989). The algorithm for the regular region of the yield surface will be derived in the next paragraph whereafter the corner regime will be discussed.

Because of the assumption of isotropic elasticity, the linear-elastic stiffness matrix D_e and the projection matrix P have the same eigenvector space, which means that the spectral decomposition is given by the same transformation matrix, according to

$$D_e = Q \Lambda_D Q^T \quad (4.28)$$

and

$$P = Q \Lambda_P Q^T \quad (4.29)$$

with the orthogonal matrix

$$\mathbf{Q} = \begin{bmatrix} \frac{1}{\sqrt{6}} & \frac{-1}{\sqrt{2}} & \frac{1}{\sqrt{3}} & 0 \\ \frac{1}{\sqrt{6}} & \frac{1}{\sqrt{2}} & \frac{1}{\sqrt{3}} & 0 \\ \frac{-2}{\sqrt{6}} & 0 & \frac{1}{\sqrt{3}} & 0 \\ 0 & 0 & 0 & 1 \end{bmatrix} \quad (4.30)$$

which satisfies $\mathbf{Q}^{-1} = \mathbf{Q}^T$. The diagonal matrices $\mathbf{\Lambda}_D$ and $\mathbf{\Lambda}_P$ are given by

$$\mathbf{\Lambda}_D = \text{diag} \left[\frac{E}{(1+\nu)}, \frac{E}{(1+\nu)}, \frac{E}{(1-2\nu)}, \frac{E}{2(1+\nu)} \right] \quad (4.31)$$

and

$$\mathbf{\Lambda}_P = \text{diag} [0, 1, 0, 2] \quad (4.32)$$

respectively. Because the linear-elastic stiffness matrix and the projection matrix have the same eigenvectors, the matrices \mathbf{A}_{ij} simplify to

$$\mathbf{A}_{11} = \mathbf{Q} \left[\mathbf{I} + \frac{\Delta\lambda^{(i+1)}}{2\Psi} \mathbf{\Lambda}_D \mathbf{\Lambda}_P \right] \mathbf{Q}^T$$

$$\mathbf{A}_{12} = -\frac{\Delta\lambda^{(i+1)}}{2\Psi} \mathbf{Q} \mathbf{\Lambda}_D \mathbf{\Lambda}_P \mathbf{Q}^T$$

$$\mathbf{A}_{21} = -\frac{\Delta\lambda^{(i+1)}}{2\Psi} (1-\gamma) E_{ks} \mathbf{Q} \mathbf{\Lambda}_M \mathbf{\Lambda}_P \mathbf{Q}^T$$

$$\mathbf{A}_{22} = \mathbf{Q} \left[\mathbf{I} + \frac{\Delta\lambda^{(i+1)}}{2\Psi} (1-\gamma) E_{ks} \mathbf{\Lambda}_M \mathbf{\Lambda}_P \right] \mathbf{Q}^T$$

Setting,

$$\mathbf{\Lambda}_{11} = \mathbf{I} + \frac{\Delta\lambda^{(i+1)}}{2\Psi} \mathbf{\Lambda}_D \mathbf{\Lambda}_P$$

$$\mathbf{\Lambda}_{12} = -\frac{\Delta\lambda^{(i+1)}}{2\Psi} \mathbf{\Lambda}_D \mathbf{\Lambda}_P$$

$$\mathbf{\Lambda}_{21} = -\frac{\Delta\lambda^{(i+1)}}{2\Psi} (1-\gamma) E_{ks} \mathbf{\Lambda}_M \mathbf{\Lambda}_P$$

$$\mathbf{\Lambda}_{22} = \mathbf{I} + \frac{\Delta\lambda^{(i+1)}}{2\Psi} (1 - \gamma) E_{ks} \mathbf{\Lambda}_M \mathbf{\Lambda}_P$$

the mapping matrix can be written as

$$\begin{bmatrix} \mathbf{A}_{11} & \mathbf{A}_{12} \\ \mathbf{A}_{21} & \mathbf{A}_{22} \end{bmatrix} = \begin{bmatrix} \mathbf{Q} & \mathbf{0} \\ \mathbf{0} & \mathbf{Q} \end{bmatrix} \begin{bmatrix} \mathbf{\Lambda}_{11} & \mathbf{\Lambda}_{12} \\ \mathbf{\Lambda}_{21} & \mathbf{\Lambda}_{22} \end{bmatrix} \begin{bmatrix} \mathbf{Q}^T & \mathbf{0} \\ \mathbf{0} & \mathbf{Q}^T \end{bmatrix} \quad (4.33)$$

The inverted mapping matrix is calculated as

$$\begin{bmatrix} \mathbf{A}_{11} & \mathbf{A}_{12} \\ \mathbf{A}_{21} & \mathbf{A}_{22} \end{bmatrix}^{-1} = \begin{bmatrix} \mathbf{Q} & \mathbf{0} \\ \mathbf{0} & \mathbf{Q} \end{bmatrix} \begin{bmatrix} \mathbf{\Lambda}_{11} & \mathbf{\Lambda}_{12} \\ \mathbf{\Lambda}_{21} & \mathbf{\Lambda}_{22} \end{bmatrix}^{-1} \begin{bmatrix} \mathbf{Q}^T & \mathbf{0} \\ \mathbf{0} & \mathbf{Q}^T \end{bmatrix} \quad (4.34)$$

with the inverted tri-diagonal matrix given by

$$\begin{bmatrix} \mathbf{\Lambda}_{11} & \mathbf{\Lambda}_{12} \\ \mathbf{\Lambda}_{21} & \mathbf{\Lambda}_{22} \end{bmatrix}^{-1} = \begin{bmatrix} (\mathbf{\Lambda}_{11}\mathbf{\Lambda}_{22} - \mathbf{\Lambda}_{12}\mathbf{\Lambda}_{21})^{-1}\mathbf{\Lambda}_{22} & -(\mathbf{\Lambda}_{11}\mathbf{\Lambda}_{22} - \mathbf{\Lambda}_{12}\mathbf{\Lambda}_{21})^{-1}\mathbf{\Lambda}_{12} \\ -(\mathbf{\Lambda}_{11}\mathbf{\Lambda}_{22} - \mathbf{\Lambda}_{12}\mathbf{\Lambda}_{21})^{-1}\mathbf{\Lambda}_{21} & (\mathbf{\Lambda}_{11}\mathbf{\Lambda}_{22} - \mathbf{\Lambda}_{12}\mathbf{\Lambda}_{21})^{-1}\mathbf{\Lambda}_{11} \end{bmatrix} \quad (4.35)$$

The matrix product $(\mathbf{\Lambda}_{11}\mathbf{\Lambda}_{22} - \mathbf{\Lambda}_{12}\mathbf{\Lambda}_{21})^{-1}$ can be computed explicitly as

$$(\mathbf{\Lambda}_{11}\mathbf{\Lambda}_{22} - \mathbf{\Lambda}_{12}\mathbf{\Lambda}_{21})^{-1} = \left[\mathbf{I} + \frac{\Delta\lambda^{(i+1)} \mathbf{\Lambda}_D \mathbf{\Lambda}_P}{2\Psi} + \frac{\Delta\lambda^{(i+1)} (1 - \gamma) E_{ks} \mathbf{\Lambda}_M \mathbf{\Lambda}_P}{2\Psi} \right]^{-1} \quad (4.36)$$

With this procedure the return-mapping algorithm has been given and the updated stress vector and the updated back stress vector are both expressed in terms of the inelastic multiplier and the trial state variables. This provides a scalar expression in the inelastic multiplier which has to be determined by enforcing the constraint condition

$$f(\boldsymbol{\sigma}^{(i+1)}, \boldsymbol{\eta}^{(i+1)}, \boldsymbol{\kappa}_T^{(i+1)}) = f(\Delta\lambda^{(i+1)}) = 0 \quad (4.37)$$

which can be solved with a local Newton-Raphson iteration where the updated inelastic multiplier is calculated as

$$J(\Delta\lambda^{(i)}) (\Delta\lambda^{(i+1)} - \Delta\lambda^{(i)}) = -f(\Delta\lambda^{(i)}) \quad (4.38)$$

The gradient $J = \partial_{\Delta\lambda} f$ is difficult and expensive to calculate and is therefore replaced by a secant Newton-Raphson method which needs only a few scalar evaluations to approximate the derivative by the secant stiffness

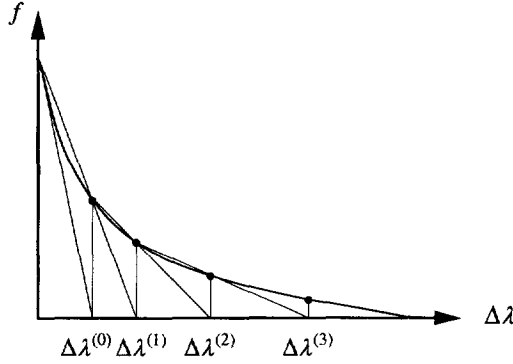


Figure 4.4 Local secant Newton-Raphson procedure.

$$J(\Delta\lambda^{(i)}) \approx \frac{f(\Delta\lambda^{(i-1)}) - f(\Delta\lambda^{(i)})}{\Delta\lambda^{(i-1)} - \Delta\lambda^{(i)}} \quad (4.39)$$

The local secant Newton-Raphson iteration for the inelastic multiplier has been depicted in Figure 4.4.

The initial gradient is calculated from the development of the yield function in a Taylor series. Neglecting second and higher order terms in the inelastic multiplier we obtain

$$f(\sigma_E, \eta_E, \kappa_E) - \Delta\lambda^{(0)} \partial_{\sigma_E} f^T D_e \partial_{\sigma_E} f + \partial_{\eta_E} f^T \Delta\eta^{(0)} + \partial_{\kappa_E} f \Delta\kappa_T^{(0)} = 0$$

With the relations

$$\Delta\eta^{(0)} = \Delta\lambda^{(0)} (1 - \gamma) E_k \partial_{\sigma} g$$

$$\Delta\kappa_T^{(0)} = \Delta\lambda^{(0)}$$

$$\partial_{\eta} f = -\partial_{\sigma} f$$

the initial gradient J is given by

$$J^{(0)} = -\partial_{\sigma_E} f^T D_e \partial_{\sigma_E} f - (1 - \gamma) E_k + \partial_{\kappa_E} f \quad (4.40)$$

The algorithm results in the final stress on the yield surface and the elastic strain vector is calculated with the elastic compliance matrix, C_e , as

$$\epsilon_e^{(i+1)} = C_e \sigma^{(i+1)} \quad (4.41)$$

The inelastic strain increment is finally calculated as

$$\Delta \boldsymbol{\varepsilon}_c^{(i+1)} = \boldsymbol{\varepsilon}_E - \boldsymbol{\varepsilon}_e^{(i+1)} \quad (4.42)$$

The solution of the nonlinear equations following from the finite element discretization will be solved using the Newton-Raphson method as has been discussed in Chapter 2. The nonlinear problem is then linearized in a sequence of iterations until the problem is converged. The linearization of the equations results in the tangent stiffness matrix which plays a crucial role in the performance and robustness of the Newton-Raphson method. It has been emphasized in the classical paper about consistent tangent operators for mathematical plasticity, Simo and Taylor (1985), that the crucial point is that the tangent stiffness matrix must be obtained by consistent linearization of the stress resulting from the return-mapping algorithm. The consistent tangent stiffness matrix has to be derived from the updated stress at the end of iteration $(i + 1)$

$$\boldsymbol{\sigma}^{(i+1)} = \mathbf{D}_e [\boldsymbol{\varepsilon}^{(i+1)} - {}^t \boldsymbol{\varepsilon}_c - \Delta \lambda^{(i+1)} \partial_{\sigma} f] \quad (4.43)$$

which is linearized by calculating the total derivative

$$d\boldsymbol{\sigma}^{(i+1)} = \mathbf{D}_e [d\boldsymbol{\varepsilon}^{(i+1)} - d\lambda \partial_{\sigma} f - \Delta \lambda^{(i+1)} \partial_{\sigma\sigma}^2 f d\boldsymbol{\sigma}^{(i+1)}] \quad (4.44)$$

With the consistency condition which has to be enforced at $(i + 1)$

$$df = \partial_{\sigma} f^T d\boldsymbol{\sigma} + \partial_{\eta} f^T d\boldsymbol{\eta} + \partial_{\kappa} f d\kappa = 0 \quad (4.45)$$

this can be written as

$$d\boldsymbol{\sigma}^{(i+1)} = \mathbf{H} [d\boldsymbol{\varepsilon}^{(i+1)} - \frac{1}{E_s} \partial_{\sigma} f \partial_{\sigma} f^T d\boldsymbol{\sigma}^{(i+1)}] \quad (4.46)$$

with the hardening parameter

$$E_s = -\partial_{\kappa} f + (1 - \gamma) E_k \quad (4.47)$$

and the modified stiffness matrix

$$\mathbf{H} = [\mathbf{C}_e + \Delta \lambda^{(i+1)} \partial_{\sigma\sigma}^2 f]^{-1} \quad (4.48)$$

The consistent tangent stiffness relation is finally obtained with the use of the Sherman-Morrison-Woodbury formula and reads

$$d\boldsymbol{\sigma}^{(i+1)} = \left[\mathbf{H} - \frac{\mathbf{H} \partial_{\sigma} f \partial_{\sigma} f^T \mathbf{H}}{E_s + \partial_{\sigma} f^T \mathbf{H} \partial_{\sigma} f} \right] d\boldsymbol{\varepsilon}^{(i+1)} \quad (4.49)$$

The Rankine yield criterion has been discussed so far without special attention for

the apex of the yield surface. The yield surface, depicted in Figure 4.3, shows a corner at the stress point $\xi_{xx} = \xi_{yy}$, $\xi_{xy} = 0$ which may cause numerical difficulties because Ψ is equal to zero at the apex. Difficulties associated with corners in yield surfaces have been dealt with for the Mohr-Coulomb criterion, De Borst (1986), Crisfield (1987), Pankaj (1990), where the Euler backward algorithm has been applied to obtain a stable return-mapping procedure. The consistent tangent stiffness matrix has also been derived for the Mohr-Coulomb criterion, Crisfield (1987), where it has been shown that the consistent tangent stiffness matrix reduces to the null-matrix at the apex.

The stress update in the apex regime of the Rankine yield surface can be treated without modifications of the return-mapping procedure given in eq.(4.25) with the explicitly computed inverted mapping matrix given in eq.(4.34). The inverted mapping matrix is always determined even if the factor Ψ is equal to zero. Without loss of generality it is shown here for isotropic hardening that the mapping procedure is unconditionally stable in the singular region of the yield surface. The matrix product $(\mathbf{A}_{11}\mathbf{A}_{22} - \mathbf{A}_{12}\mathbf{A}_{21})^{-1}$ now reduces to (cf. eq.(4.36))

$$(\mathbf{A}_{11}\mathbf{A}_{22} - \mathbf{A}_{12}\mathbf{A}_{21})^{-1} = \left[\mathbf{I} + \frac{\Delta\lambda}{2\Psi} \mathbf{A}_D \mathbf{A}_P \right]^{-1}$$

and the inverted tri-diagonal matrix becomes

$$\begin{bmatrix} \mathbf{A}_{11} & \mathbf{A}_{12} \\ \mathbf{A}_{21} & \mathbf{A}_{22} \end{bmatrix}^{-1} = \begin{bmatrix} 1 & 0 & 0 & 0 & 0 & 0 & 0 & 0 \\ 0 & \frac{\Psi}{\Psi + \Delta\lambda G} & 0 & 0 & 0 & \frac{\Delta\lambda G}{\Psi + \Delta\lambda G} & 0 & 0 \\ 0 & 0 & 1 & 0 & 0 & 0 & 0 & 0 \\ 0 & 0 & 0 & \frac{\Psi}{\Psi + \Delta\lambda G} & 0 & 0 & 0 & \frac{\Delta\lambda G}{\Psi + \Delta\lambda G} \\ 0 & 0 & 0 & 0 & 1 & 0 & 0 & 0 \\ 0 & 0 & 0 & 0 & 0 & 1 & 0 & 0 \\ 0 & 0 & 0 & 0 & 0 & 0 & 1 & 0 \\ 0 & 0 & 0 & 0 & 0 & 0 & 0 & 1 \end{bmatrix}$$

with $G = E / 2(1 + \nu)$. Transformation from the eigenvector space to the stress space results in the limit

$$\lim_{\Psi \rightarrow 0} \begin{bmatrix} \mathbf{A}_{11} & \mathbf{A}_{12} \\ \mathbf{A}_{21} & \mathbf{A}_{22} \end{bmatrix}^{-1} = \begin{bmatrix} 1/2 & 1/2 & 0 & 0 & 1/2 & -1/2 & 0 & 0 \\ 1/2 & 1/2 & 0 & 0 & -1/2 & 1/2 & 0 & 0 \\ 0 & 0 & 1 & 0 & 0 & 0 & 0 & 0 \\ 0 & 0 & 0 & 0 & 0 & 0 & 0 & 1 \\ 0 & 0 & 0 & 0 & 1 & 0 & 0 & 0 \\ 0 & 0 & 0 & 0 & 0 & 1 & 0 & 0 \\ 0 & 0 & 0 & 0 & 0 & 0 & 1 & 0 \\ 0 & 0 & 0 & 0 & 0 & 0 & 0 & 1 \end{bmatrix} \quad (4.50)$$

so that the update of the stress vector is given by

$$\sigma^{(i+1)} = \begin{bmatrix} 1/2 & 1/2 & 0 & 0 \\ 1/2 & 1/2 & 0 & 0 \\ 0 & 0 & 1 & 0 \\ 0 & 0 & 0 & 0 \end{bmatrix} \{ \sigma_E - 1/2 \Delta \lambda D_e \pi \}$$

see Figure 4.5. The return-mapping procedure is stable even in the corner-regime where the stress is returned to the yield surface in approximately 10 iterations with an accuracy of 10^{-4} with respect to the initial equivalent stress. The calculation of the mapping matrix is also possible with a numerical scheme, e.g. Gauß-decomposition, which results already in the limit of eq.(4.50) even if the factor $\Delta \lambda / 2\Psi$ is equal to 10. For this factor, with a Young's modulus equal to $30000 \text{ [N/mm}^2\text{]}$ and a Poisson ratio equal to 0.15, the mapping matrix is given by

$$\left[I + \frac{\Delta \lambda}{2\Psi} D P \right]^{-1} = \begin{bmatrix} 5.000e-01 & 5.000e-01 & 0.000e+00 & 0.000e+00 \\ 5.000e-01 & 5.000e-01 & 0.000e+00 & 0.000e+00 \\ 0.000e+00 & 0.000e+00 & 1.000e+00 & 0.000e+00 \\ 0.000e+00 & 0.000e+00 & 0.000e+00 & 3.833e-06 \end{bmatrix}$$

which can be considered as accurate. The calculation of the inverted mapping matrix can now be performed with a numerical scheme in which the factor $\Delta \lambda / 2\Psi$ should be less or equal 10. The calculation of the inverted mapping matrix with a numerical scheme is accurate even if the Poisson ratio is equal to 0.49, Groen (1993).

The next issue which has to be treated for the apex is the modified stiffness matrix, eq.(4.48), which is not defined in the apex of the yield surface. We first consider the second derivative of the yield function

$$\partial_{\sigma\sigma}^2 f = \frac{P}{2\Psi} - \frac{P \xi \xi^T P}{4\Psi^3} \quad (4.51)$$

This expression indeed becomes singular if $\Psi = [1/2 \xi^T P \xi]^{1/2}$ equals zero. Substitution of the second derivative in the expression for the modified stiffness matrix H , eq.(4.48) results after some algebraic manipulations in

$$H = \left[C_e + \frac{\Delta \lambda}{2\Psi} \left(P - \frac{1}{2\Psi^2} s s^T \right) \right]^{-1} \quad (4.52)$$

with $s = P \xi$. We now introduce the normalized vector \hat{s} such that

$$s = \| P \xi \| \hat{s} = (\xi^T P P \xi)^{1/2} \hat{s} = (\beta \xi^T P \xi)^{1/2} \hat{s} = \Psi \sqrt{2\beta} \hat{s} \quad (4.53)$$

with $\| \cdot \|$ the symbol designating the L_2 -norm. For the Rankine criterion β equals

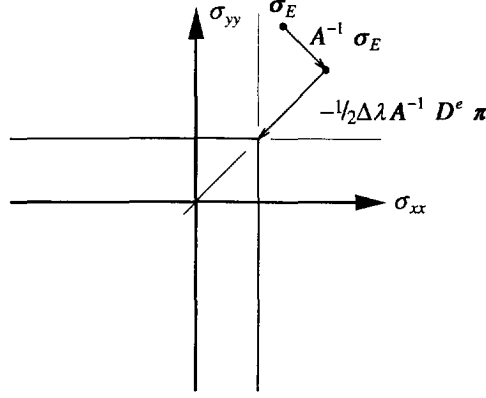


Figure 4.5 Return-mapping of the trial stress to the apex.

$\beta = 1 + 2 \xi_{xy}^2 / s^T s$. With eq.(4.53), the modified stiffness matrix becomes

$$H = \left[C_e + \frac{\Delta \lambda}{2\Psi} \left(P - \beta \hat{s} \hat{s}^T \right) \right]^{-1} \quad (4.54)$$

The apex of the yield surface is determined by the condition $\xi_{xx} = \xi_{yy}$; $\xi_{xy} = 0$. Then the stress vector \hat{s} reduces to the null-vector and the limit of the modified stiffness matrix in the apex is given by

$$\lim_{\Psi \rightarrow 0} H = \lim_{\Psi \rightarrow 0} \left[C_e + \frac{\Delta \lambda}{2\Psi} P \right]^{-1} = A_{11}^{-1} D_e \quad (4.55)$$

because of the assumption of isotropic elasticity. The gradient of the yield surface is also not defined for the apex, but it is assumed that the gradient is given by

$$\partial_{\sigma} f = 1/2 \sqrt{2} \pi \quad (4.56)$$

with the factor $1/2\sqrt{2}$ to obtain a consistent length of the gradient vector in the apex. Whereas the return-mapping algorithm is unconditionally stable even if the apex is encountered, the modified stiffness matrix cannot be calculated without a numerical approximation of the apex regime. It is therefore assumed in the algorithm for the calculation of the tangent stiffness matrix that a stress point lies within the apex region of the yield surface if the factor Ψ becomes less than 10^{-4} times the initial equivalent stress.

For the corner regime, the tangent stiffness relation, eq.(4.49) is computed with the limit of the modified stiffness matrix, eq.(4.55) and the limit of the gradient vector assumed to be given by eq.(4.56). For $E_s = 0$ then the tangent stiffness matrix can then be elaborated as

$$d\sigma = \begin{bmatrix} 0 & 0 & 0 & 0 \\ 0 & 0 & 0 & 0 \\ 0 & 0 & E & 0 \\ 0 & 0 & 0 & 0 \end{bmatrix} d\epsilon$$

This tangent stiffness matrix may result in numerical difficulties because mechanisms are likely to occur, but the expansion-compression algorithm does not fail because of dividing by zero, and the compressed tangent stiffness matrix for the plane-stress condition, eq.(2.34), is given by

$$\tilde{D} = \begin{bmatrix} 0 & 0 & 0 \\ 0 & 0 & 0 \\ 0 & 0 & 0 \end{bmatrix}$$

4.1.2 A composite yield criterion

The return-mapping algorithm described in the previous paragraph is also applicable to a situation where the constitutive model consists of two different yield surfaces, one bounding the tensile stresses, the other applicable in the compressive region, which can be represented by

$$\begin{cases} f_1 = 0 \\ f_2 = 0 \end{cases} \quad (4.57)$$

In hardening plasticity with negative hardening moduli it is complicated to identify whether only one, or whether both surfaces are active. The location of the intersection between the two yield surfaces is unknown in the beginning of the step and the initial configuration cannot provide a sufficient criterion for determination which surface is active at the end of the time step. Simo, Kennedy and Govindjee (1988) proposed an algorithm in which the assumption is made that the number of active yield surfaces in the final stress state is less than or equal to the number of active yield surfaces in the trial stress state. Each active yield surface is deactivated when the corresponding inelastic multiplier turns out to be negative. The opposite approach has been proposed by Pramono and Willam (1989) in which each active yield surface is evaluated one by one. The most dominant active yield surface is chosen and the trial stress is mapped back onto the yield surface. If the stress state also violates the second yield surface, the return-mapping from the trial stress state is repeated with both yield surfaces active. In

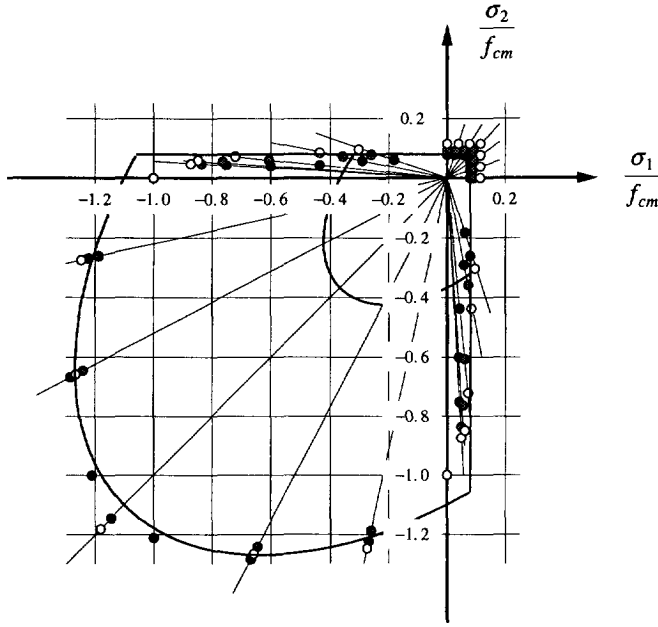


Figure 4.6 Comparison of a Rankine-Von Mises yield surface with experimental data of Kupfer and Gerstle (1974). $\bar{\sigma}_1 = f_{ct,m}$, $\bar{\sigma}_2 = 1.1 f_{cm}$

this study a direct approach is applied to solve the return-mapping to the combined yield surface. In the trial state, the yield functions are both linearized to obtain the initial Jacobian which is used to iterate with a local Newton-Raphson iteration to the final stress state for which the discrete Kuhn-Tucker conditions hold

$$\begin{cases} \Delta \lambda_j^{(i+1)} \geq 0 \\ f_j(\sigma^{(i+1)}, \eta^{(i+1)}, \kappa_j^{(i+1)}) \leq 0 \\ \Delta \lambda_j^{(i+1)} f_j(\sigma^{(i+1)}, \eta^{(i+1)}, \kappa_j^{(i+1)}) = 0 \end{cases} \quad j = 1, 2 \quad (4.58)$$

Comparison with the experimental data of Kupfer and Gerstle (1974) indicates that a composite yield contour can be defined such that a Rankine yield criterion is used to model the tension-tension region and a Von Mises yield function models the compressive stress states, Figure 4.6. The formulation of the composite yield criterion is given by the function of the Rankine yield function which has been discussed in the previous paragraph and by the function for the Von Mises yield criterion in the stress space, which results in

$$\begin{cases} f_1 = (1/2 \boldsymbol{\xi}^T \mathbf{P}_1 \boldsymbol{\xi})^{1/2} + 1/2 \boldsymbol{\pi}^T \boldsymbol{\xi} - \bar{\sigma}_1(\gamma \kappa_T) \\ f_2 = (1/2 \boldsymbol{\sigma}^T \mathbf{P}_2 \boldsymbol{\sigma})^{1/2} - \bar{\sigma}_2(\kappa_C) \end{cases} \quad (4.59)$$

with a mixed hardening rule for the Rankine criterion and an isotropic hardening rule for the Von Mises criterion. The Von Mises yield function is determined by the projection matrix

$$\mathbf{P}_2 = \begin{bmatrix} 2 & -1 & -1 & 0 \\ -1 & 2 & -1 & 0 \\ -1 & -1 & 2 & 0 \\ 0 & 0 & 0 & 6 \end{bmatrix} \quad (4.60)$$

and the equivalent stress $\bar{\sigma}_2$ which is the uniaxial compressive strength of the material. The composite yield surface is shown in Figure 4.7 with iso-shear stress lines in the stress space.

The inelastic strain rate is determined by Koiter's rule, Koiter (1953), which allows for a summation of the inelastic strain of each yield function according to

$$\dot{\boldsymbol{\varepsilon}}_c = \dot{\boldsymbol{\varepsilon}}_{c,1} + \dot{\boldsymbol{\varepsilon}}_{c,2} = \dot{\lambda}_1 \partial_{\boldsymbol{\sigma}} f_1 + \dot{\lambda}_2 \partial_{\boldsymbol{\sigma}} f_2 \quad (4.61)$$

The damage in the material is reflected in the two internal parameters, one for damage in tension, κ_T , and one for the damage in compression, κ_C . For a work-hardening hypothesis, the internal parameters are determined by the inelastic work rate for the two respective yield functions, i.e.

$$\begin{cases} \dot{W}_{c,1} = \boldsymbol{\xi}^T \dot{\boldsymbol{\varepsilon}}_{c,1} + \zeta_{12} \frac{\bar{\sigma}_1}{\bar{\sigma}_2} \boldsymbol{\sigma}^T \dot{\boldsymbol{\varepsilon}}_{c,2} = \bar{\sigma}_1(\gamma \kappa_T) \dot{\kappa}_T \\ \dot{W}_{c,2} = \boldsymbol{\sigma}^T \dot{\boldsymbol{\varepsilon}}_{c,2} + \zeta_{21} \frac{\bar{\sigma}_2}{\bar{\sigma}_1} \boldsymbol{\xi}^T \dot{\boldsymbol{\varepsilon}}_{c,1} = \bar{\sigma}_2(\kappa_C) \dot{\kappa}_C \end{cases} \quad (4.62)$$

with scalars ζ_{12} and ζ_{21} which represent the coupling of the damage in the materials in tension and compression. With the application of Euler's theorem eqs.(4.59)-(4.62) result in the following expression for the evolution of the internal parameters

$$\begin{cases} \dot{\kappa}_T = \dot{\lambda}_1 + \zeta_{12} \dot{\lambda}_2 \\ \dot{\kappa}_C = \zeta_{21} \dot{\lambda}_1 + \dot{\lambda}_2 \end{cases} \quad (4.63)$$

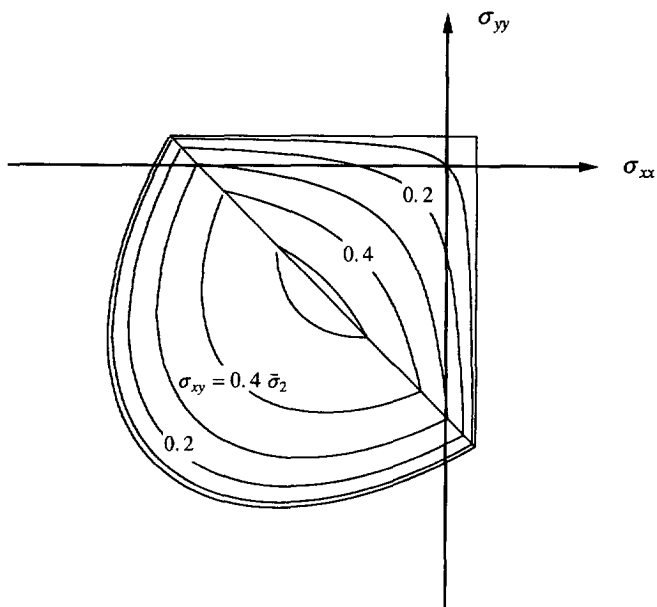


Figure 4.7 Composite yield surface with iso-shear stress lines.

With

$$\dot{\mathbf{q}} = \begin{Bmatrix} \dot{\kappa}_T \\ \dot{\kappa}_C \end{Bmatrix} \quad \mathbf{h}_1 = \begin{Bmatrix} 1 \\ \zeta_{21} \end{Bmatrix} \quad \mathbf{h}_2 = \begin{Bmatrix} \zeta_{12} \\ 1 \end{Bmatrix} \quad (4.64)$$

eq.(4.63) can formally be expressed as

$$\dot{\mathbf{q}} = \dot{\lambda}_1 \mathbf{h}_1 + \dot{\lambda}_2 \mathbf{h}_2 \quad (4.65)$$

Because the hardening functions are given by a scalar expression, the incremental internal parameter vector is determined by

$$\Delta \mathbf{q}^{(i+1)} = \Delta \lambda_1^{(i+1)} \mathbf{h}_1 + \Delta \lambda_2^{(i+1)} \mathbf{h}_2 \quad (4.66)$$

for a coupled system of two yield surfaces.

The return-mapping procedure described in the previous paragraph is now extended and reads

$$\begin{cases} \boldsymbol{\sigma}^{(i+1)} &= \boldsymbol{\sigma}_E - \Delta\lambda_1^{(i+1)} \mathbf{D}_e \partial_\sigma f_1^{(i+1)} - \Delta\lambda_2^{(i+1)} \mathbf{D}_e \partial_\sigma f_2^{(i+1)} \\ \boldsymbol{\eta}^{(i+1)} &= \boldsymbol{\eta}_E + \Delta\lambda_1^{(i+1)} (1-\gamma) E_{ks} \partial_\sigma g_1^{(i+1)} \end{cases} \quad (4.67)$$

The updated stress and the updated back stress are now given by the solution of the following system of equations

$$\begin{Bmatrix} \boldsymbol{\sigma}^{(i+1)} \\ \boldsymbol{\eta}^{(i+1)} \end{Bmatrix} = \begin{bmatrix} \mathbf{A}_{11} & \mathbf{A}_{12} \\ \mathbf{A}_{21} & \mathbf{A}_{22} \end{bmatrix}^{-1} \begin{Bmatrix} \boldsymbol{\sigma}_E - 1/2 \Delta\lambda_1^{(i+1)} \mathbf{D}_e \boldsymbol{\pi} \\ \boldsymbol{\eta}_E + 1/2 \Delta\lambda_1^{(i+1)} (1-\gamma) E_{ks} \boldsymbol{\pi} \end{Bmatrix} \quad (4.68)$$

with the matrices

$$\mathbf{A}_{11} = \mathbf{I} + \frac{\Delta\lambda_1^{(i+1)}}{2\Psi_1} \mathbf{D}_e \mathbf{P}_1 + \frac{\Delta\lambda_2^{(i+1)}}{2\Psi_2} \mathbf{D}_e \mathbf{P}_2$$

$$\mathbf{A}_{12} = -\frac{\Delta\lambda_1^{(i+1)}}{2\Psi_1} \mathbf{D}_e \mathbf{P}_1$$

$$\mathbf{A}_{21} = -\frac{\Delta\lambda_1^{(i+1)}}{2\Psi_1} (1-\gamma) E_{ks} \boldsymbol{\Lambda}_M \mathbf{P}_1$$

$$\mathbf{A}_{22} = \mathbf{I} + \frac{\Delta\lambda_1^{(i+1)}}{2\Psi_1} (1-\gamma) E_{ks} \boldsymbol{\Lambda}_M \mathbf{P}_1$$

The denominators Ψ_1 and Ψ_2 are given by

$$\begin{cases} \Psi_1 &= \bar{\sigma}_1(\gamma\kappa_T) - 1/2 \boldsymbol{\pi}^T (\boldsymbol{\sigma}^{(i+1)} - \boldsymbol{\eta}^{(i+1)}) \\ \Psi_2 &= \bar{\sigma}_2(\kappa_C) \end{cases} \quad (4.69)$$

which is again not very convenient because the updated stress cannot be related linearly to the trial state. To arrive at a more suitable form we multiply $\boldsymbol{\sigma}^{(i+1)}$ and $\boldsymbol{\eta}^{(i+1)}$ with the vector $\boldsymbol{\pi}^T$ so that

$$\begin{cases} \pi^T \sigma^{(i+1)} = \pi^T \sigma_E - \frac{1}{2} \Delta \lambda_1^{(i+1)} \pi^T D_e \pi - \frac{\Delta \lambda_2^{(i+1)}}{2 \bar{\sigma}_2} \pi^T D_e P_2 \sigma^{(i+1)} \\ \pi^T \eta^{(i+1)} = \pi^T \eta_E - \frac{1}{2} \Delta \lambda_1^{(i+1)} (1 - \gamma) \pi^T E_{ks} \pi \end{cases} \quad (4.70)$$

because $\pi^T D_e P_1 = 0^T$. The factor $\pi^T \eta$ is now expressed in terms of the trial variables and the plastic multiplier $\Delta \lambda_1$, but the factor $\pi^T \sigma$ is still a function of the final stress because $\pi^T D_e P_2 = 2 G \{ 1, 1, -2, 0 \} \neq 0^T$ with G the linear-elastic shear modulus. Substitution of this relation into eq.(4.70) results in

$$\begin{aligned} \pi^T \sigma^{(i+1)} = \pi^T \sigma_E - \frac{1}{2} \Delta \lambda_1^{(i+1)} \pi^T D_e \pi \\ - \frac{\Delta \lambda_2^{(i+1)} G}{\bar{\sigma}_2} \pi^T \sigma^{(i+1)} + \frac{2 \Delta \lambda_2^{(i+1)} G}{\bar{\sigma}_2} \sigma_{zz}^{(i+1)} \end{aligned} \quad (4.71)$$

The return-mapping of the stress in the z -direction is given by (cf. eq.(4.67)),

$$\begin{aligned} \sigma_{zz}^{(i+1)} = \sigma_{zz,E} - \Delta \lambda_1^{(i+1)} \frac{\nu E}{(1 + \nu)(1 - 2\nu)} \\ + \frac{\Delta \lambda_2^{(i+1)} G}{\bar{\sigma}_2} \pi^T \sigma^{(i+1)} - \frac{2 \Delta \lambda_2^{(i+1)} G}{\bar{\sigma}_2} \sigma_{zz}^{(i+1)} \end{aligned} \quad (4.72)$$

The factor $\pi^T \sigma^{(i+1)}$ is obtained by substituting eq.(4.72) into eq.(4.71) which results in

$$\begin{aligned} \pi^T \sigma^{(i+1)} = \frac{\bar{\sigma}_2 + 2 \Delta \lambda_2^{(i+1)} G}{\bar{\sigma}_2 + 3 \Delta \lambda_2^{(i+1)} G} \left(\pi^T \sigma_E - \frac{1}{2} \Delta \lambda_1^{(i+1)} \pi^T D_e \pi \right) \\ + \frac{2 \Delta \lambda_2^{(i+1)} G}{\bar{\sigma}_2 + 3 \Delta \lambda_2^{(i+1)} G} \left(\sigma_{zz,E} - \Delta \lambda_1^{(i+1)} \frac{\nu E}{(1 + \nu)(1 - 2\nu)} \right) \end{aligned} \quad (4.73)$$

With this result the denominators are solely expressed in terms of the trial state variables and the inelastic multipliers.

With the spectral decomposition described in the preceding section, the matrices are expressed as

$$\begin{aligned} D_e &= Q \Lambda_D Q^T \\ P_1 &= Q \Lambda_{P1} Q^T \\ P_2 &= Q \Lambda_{P2} Q^T \end{aligned} \quad (4.74)$$

with the diagonal matrices

$$\begin{aligned}
\Lambda_D &= \text{diag} \left[\frac{E}{(1+\nu)}, \frac{E}{(1+\nu)}, \frac{E}{(1-2\nu)}, \frac{E}{2(1+\nu)} \right] \\
\Lambda_{P_1} &= \text{diag} [0, 1, 0, 2] \\
\Lambda_{P_2} &= \text{diag} [3, 3, 0, 6]
\end{aligned} \tag{4.75}$$

and the orthogonal matrix Q as given by eq.(4.30). We can now elaborate A_{ij} as

$$\begin{aligned}
A_{11} &= Q \left[I + \frac{\Delta\lambda_1^{(i+1)}}{2\Psi_1} \Lambda_D \Lambda_{P_1} + \frac{\Delta\lambda_2^{(i+1)}}{2\Psi_2} \Lambda_D \Lambda_{P_2} \right] Q^T \\
A_{12} &= - \frac{\Delta\lambda_1^{(i+1)}}{2\Psi_1} Q \Lambda_D \Lambda_{P_1} Q^T \\
A_{21} &= - \frac{\Delta\lambda_1^{(i+1)}}{2\Psi_1} (1-\gamma) E_{ks} Q \Lambda_M \Lambda_{P_1} Q^T \\
A_{22} &= Q \left[I + \frac{\Delta\lambda_1^{(i+1)}}{2\Psi_1} (1-\gamma) E_{ks} \Lambda_M \Lambda_{P_1} \right] Q^T
\end{aligned} \tag{4.76}$$

The mapping matrix can be inverted using eq.(4.34) with the inverted tri-diagonal matrix given by eq.(4.35). The matrix product $(\Lambda_{11}\Lambda_{22} - \Lambda_{12}\Lambda_{21})^{-1}$ is now computed explicitly as

$$(\Lambda_{11}\Lambda_{22} - \Lambda_{12}\Lambda_{21})^{-1} = \left[I + \frac{\Delta\lambda_1^{(i+1)}}{2\Psi_1} \Lambda_D \Lambda_{P_1} + \frac{\Delta\lambda_2^{(i+1)}}{2\Psi_2} \Lambda_D \Lambda_{P_2} + \frac{\Delta\lambda_1^{(i+1)} (1-\gamma) E_{ks} \Lambda_M \Lambda_{P_1}}{2\Psi_1} \right]^{-1}$$

Upon substitution of $\sigma^{(i+1)}$ and $\eta^{(i+1)}$ as given in eq.(4.68), we observe that the yield functions are now solely expressed in terms of the inelastic multipliers $\Delta\lambda_1$ and $\Delta\lambda_2$. The constraint equations

$$\begin{cases} c_1 f_1(\Delta\lambda_1^{(i+1)}, \Delta\lambda_2^{(i+1)}) = 0 \\ c_2 f_2(\Delta\lambda_1^{(i+1)}, \Delta\lambda_2^{(i+1)}) = 0 \end{cases} \tag{4.77}$$

have to be solved to obtain the final stress state. This is done using a local Newton-Raphson iteration with a Broyden update of the Jacobian, see Dennis and Schnabel (1983). The scalars c_1 and c_2 are equal to one when the corresponding yield function is active, else the scalars are equal to zero. The initial Jacobian is determined from the linearization of both yield functions in the trial state

$$\begin{cases} f_1^{(i+1)} = f_1(\sigma_E - \sum_j^2 \Delta\lambda_j^{(0)} D_e \partial_\sigma f_j, \eta_E + \Delta\eta, \kappa_{T,E} + \Delta\kappa_T) \\ f_2^{(i+1)} = f_2(\sigma_E - \sum_j^2 \Delta\lambda_j^{(0)} D_e \partial_\sigma f_j, \kappa_{C,E} + \Delta\kappa_C) \end{cases} \quad (4.78)$$

which results in the following system of equations

$$J^{(0)} s_0 = -f(x_0) \quad (4.79)$$

with the initial Jacobian

$$\begin{aligned} J_{11}^{(0)} &= -\partial_\sigma f_1^T D_e \partial_\sigma f_1 - (1-\gamma) E_{ks} + \partial_q f_1^T h_1 \\ J_{12}^{(0)} &= -\partial_\sigma f_1^T D_e \partial_\sigma f_2 + \partial_q f_1^T h_2 \\ J_{21}^{(0)} &= -\partial_\sigma f_2^T D_e \partial_\sigma f_1 + \partial_q f_2^T h_1 \\ J_{22}^{(0)} &= -\partial_\sigma f_2^T D_e \partial_\sigma f_2 + \partial_q f_2^T h_2 \end{aligned} \quad (4.80)$$

and the vectors

$$\begin{aligned} s^{(0)} &= \{ \Delta\lambda_1^{(0)}, \Delta\lambda_2^{(0)} \}^T \\ f^{(0)} &= \{ c_1 f_1(\sigma_E, \eta_E, \kappa_{T,E}), c_2 f_2(\sigma_E, \kappa_{C,E}) \}^T \end{aligned} \quad (4.81)$$

Initially the constraints are determined by the violation of the yield criterion in the trial state, i.e.

$$\begin{cases} c_1 = 1 & \text{if } f_1(\sigma_E, \eta_E, \kappa_{T,E}) > 0 \\ c_2 = 1 & \text{if } f_2(\sigma_E, \kappa_{C,E}) > 0 \end{cases}$$

During the return-mapping the active yield functions are determined with conditions

$$c_j = 1 \quad \text{if } \Delta\lambda_j^{(i+1)} > 0 \quad \text{else} \quad c_j = 0$$

With this algorithm it is possible to return to a single active yield surface within a maximum of approximately 10 iterations in most cases, even if in the trial state both yield conditions are violated.

The consistent tangent stiffness matrix for the Newton-Raphson iteration is again

most conveniently derived from the updated stress at time $(i + 1)$

$$\boldsymbol{\sigma}^{(i+1)} = \mathbf{D}_e [\boldsymbol{\varepsilon}^{(i+1)} - \boldsymbol{\varepsilon}_c - \Delta\lambda_1^{(i+1)} \partial_{\sigma} f_1 - \Delta\lambda_2^{(i+1)} \partial_{\sigma} f_2] \quad (4.82)$$

The total derivative then reads

$$\begin{aligned} d\boldsymbol{\sigma}^{(i+1)} = \mathbf{D}_e [d\boldsymbol{\varepsilon}^{(i+1)} - d\lambda_1 \partial_{\sigma} f_1 - \Delta\lambda_1^{(i+1)} \partial_{\sigma\sigma}^2 f_1 d\boldsymbol{\sigma}^{(i+1)} \\ - d\lambda_2 \partial_{\sigma} f_2 - \Delta\lambda_2^{(i+1)} \partial_{\sigma\sigma}^2 f_2 d\boldsymbol{\sigma}^{(i+1)}] \end{aligned} \quad (4.83)$$

which is written as

$$d\boldsymbol{\sigma}^{(i+1)} = \mathbf{H} [d\boldsymbol{\varepsilon}^{(i+1)} - d\lambda_1 \partial_{\sigma} f_1 - d\lambda_2 \partial_{\sigma} f_2] \quad (4.84)$$

Applying the general formulation of Riggs and Powel (1990), the tangent stiffness matrix is written as

$$d\boldsymbol{\sigma}^{(i+1)} = \mathbf{H} [d\boldsymbol{\varepsilon}^{(i+1)} - \mathbf{U} d\boldsymbol{\lambda}] \quad (4.85)$$

with the matrix \mathbf{U} given by

$$\mathbf{U} = \begin{bmatrix} c_1 \partial_{\sigma} f_1, c_2 \partial_{\sigma} f_2 \end{bmatrix} \quad (4.86)$$

and the vector $d\boldsymbol{\lambda}$ in which the plastic multipliers are collected, i.e. $d\boldsymbol{\lambda} = \{ d\lambda_1, d\lambda_2 \}^T$. The modified stiffness matrix \mathbf{H} is given by

$$\mathbf{H} = [\mathbf{C}_e + \Delta\lambda_1^{(i+1)} \partial_{\sigma\sigma}^2 f_1 + \Delta\lambda_2^{(i+1)} \partial_{\sigma\sigma}^2 f_2]^{-1} \quad (4.87)$$

The consistency conditions determined by the active yield surfaces, give the relations for the inelastic multipliers

$$c_1 (\partial_{\sigma} f_1^T d\boldsymbol{\sigma} + \partial_{\eta} f_1^T d\boldsymbol{\eta} + \partial_q f_1^T d\mathbf{q}) + (1 - c_1) d\lambda_1 = 0 \quad (4.88)$$

and

$$c_2 (\partial_{\sigma} f_2^T d\boldsymbol{\sigma} + \partial_q f_2^T d\mathbf{q}) + (1 - c_2) d\lambda_2 = 0 \quad (4.89)$$

If the relations $d\mathbf{q} = c_1 \mathbf{h}_1 d\lambda_1 + c_2 \mathbf{h}_2 d\lambda_2$ and $d\boldsymbol{\eta} = c_1 d\lambda_1 (1 - \gamma) E_k \partial_{\sigma} g_1$ are substituted, the consistency conditions are expressed in the following system of equations

$$d\boldsymbol{\lambda} = \mathbf{E}^{-1} \mathbf{V}^T d\boldsymbol{\sigma} \quad (4.90)$$

with

$$E = \begin{bmatrix} -c_1 \partial_q f_1^T \mathbf{h}_1 + c_1 (1 - \gamma) E_k + (1 - c_1) & -c_1 c_2 \partial_q f_1^T \mathbf{h}_2 \\ -c_1 c_2 \partial_q f_2^T \mathbf{h}_1 & -c_2 \partial_q f_2^T \mathbf{h}_2 + (1 - c_2) \end{bmatrix}$$

and

$$V^T = \begin{bmatrix} c_1 \partial_\sigma f_1^T \\ c_2 \partial_\sigma f_2^T \end{bmatrix}$$

Substituting eq.(4.90) into eq.(4.85) results in

$$\left[H^{-1} + U E^{-1} V^T \right] d\sigma^{(i+1)} = d\epsilon^{(i+1)} \quad (4.91)$$

The consistent tangent stiffness matrix can be calculated with the application of the Sherman-Morrison-Woodbury formula which results in

$$d\sigma^{(i+1)} = \left[H - H U (E + V^T H U)^{-1} V^T H \right] d\epsilon^{(i+1)} \quad (4.92)$$

It is noted that if the yield functions are coupled through the hardening functions given in eq.(4.64), the tangent stiffness matrix is in general non-symmetric.

The corners in the composite yield surface require special attention since they may cause numerical difficulties. The apex of the composite yield surface is completely governed by the Rankine yield function and the analysis of the apex given in the previous paragraph remains valid for the composite yield surface.

The second possible situation which may cause numerical problems is the situation where the equivalent stress of the Von Mises yield function has been reduced to zero and the yield surface has shrunk to a single point in the origin of the stress space. If the equivalent stress of the Von Mises yield function is equal to zero, it implies that the factor Ψ_2 is equal to zero, cf. eq.(4.69). Suppose that only the Von Mises yield function is active, then the matrices Λ_{ij} of the mapping matrix are given by

$$\begin{aligned} \Lambda_{11} &= I + \frac{\Delta\lambda_2}{2\Psi_2} \Lambda_D \Lambda_{P2} \\ \Lambda_{12} &= 0 \\ \Lambda_{21} &= 0 \\ \Lambda_{22} &= I \end{aligned} \quad (4.93)$$

and the matrix product $(\Lambda_{11}\Lambda_{22} - \Lambda_{12}\Lambda_{21})^{-1}$ is equal to

$$(\mathbf{A}_{11}\mathbf{A}_{22} - \mathbf{A}_{12}\mathbf{A}_{21})^{-1} = \left[\mathbf{I} + \frac{\Delta\lambda_2 \mathbf{A}_D \mathbf{A}_{P2}}{2\Psi_2} \right]^{-1}$$

Substitution of these expressions in the inverted tri-diagonal matrix results in

$$\begin{bmatrix} \mathbf{A}_{11} & \mathbf{A}_{12} \\ \mathbf{A}_{21} & \mathbf{A}_{22} \end{bmatrix}^{-1} = \begin{bmatrix} \frac{\Psi_2}{\Psi_2 + 3\Delta\lambda_2 G} & & & & & & & \\ & \frac{\Psi_2}{\Psi_2 + 3\Delta\lambda_2 G} & & & & & & \\ & & 1 & & & & & \\ & & & \frac{\Psi_2}{\Psi_2 + 3\Delta\lambda_2 G} & & & & \\ & & & & 1 & & & \\ & & & & & 1 & & \\ & & & & & & 1 & \\ & & & & & & & 1 \end{bmatrix}$$

with $G = E / 2(1 + \nu)$. Transformation from the eigenvector space to the stress space results in the limit

$$\lim_{\Psi_2 \rightarrow 0} \begin{bmatrix} \mathbf{A}_{11} & \mathbf{A}_{12} \\ \mathbf{A}_{21} & \mathbf{A}_{22} \end{bmatrix}^{-1} = \begin{bmatrix} 1/3 & 1/3 & 1/3 & 0 & 0 & 0 & 0 & 0 \\ 1/3 & 1/3 & 1/3 & 0 & 0 & 0 & 0 & 0 \\ 1/3 & 1/3 & 1/3 & 0 & 0 & 0 & 0 & 0 \\ 0 & 0 & 0 & 0 & 0 & 0 & 0 & 0 \\ 0 & 0 & 0 & 0 & 1 & 0 & 0 & 0 \\ 0 & 0 & 0 & 0 & 0 & 1 & 0 & 0 \\ 0 & 0 & 0 & 0 & 0 & 0 & 1 & 0 \\ 0 & 0 & 0 & 0 & 0 & 0 & 0 & 1 \end{bmatrix} \quad (4.94)$$

The return-mapping procedure of the stress vector is then given by

$$\boldsymbol{\sigma}^{(i+1)} = \begin{bmatrix} 1/3 & 1/3 & 1/3 & 0 \\ 1/3 & 1/3 & 1/3 & 0 \\ 1/3 & 1/3 & 1/3 & 0 \\ 0 & 0 & 0 & 0 \end{bmatrix} \boldsymbol{\sigma}_E$$

which is a return-mapping onto the hydrostatic axis in the stress space. Also in this case a numerical scheme can be utilized to calculate the mapping matrix.

The next situation which has to be treated is the situation in which both yield functions are active and both Ψ_1 and Ψ_2 are equal to zero. In this case, the mapping procedure is determined by the full expression of eq.(4.68) for which the different matrices are given by, restricting for simplicity sake the analysis to the case of isotropic hardening,

$$\begin{aligned}
 \Lambda_{11} &= I + \frac{\Delta\lambda_1}{2\Psi_1} \Lambda_D \Lambda_{P1} + \frac{\Delta\lambda_2}{2\Psi_2} \Lambda_D \Lambda_{P2} \\
 \Lambda_{12} &= \frac{\Delta\lambda_1}{2\Psi_1} \Lambda_D \Lambda_{P1} \\
 \Lambda_{21} &= 0 \\
 \Lambda_{22} &= I
 \end{aligned} \tag{4.95}$$

The matrix product $(\Lambda_{11}\Lambda_{22} - \Lambda_{12}\Lambda_{21})^{-1}$ is then equal to

$$(\Lambda_{11}\Lambda_{22} - \Lambda_{12}\Lambda_{21})^{-1} = \left[I + \frac{\Delta\lambda_1}{2\Psi_1} \Lambda_D \Lambda_{P1} + \frac{\Delta\lambda_2}{2\Psi_2} \Lambda_D \Lambda_{P2} \right]^{-1} \tag{4.96}$$

Substitution of eqs.(4.95) and (4.96) in the inverted tri-diagonal matrix results in

$$\begin{bmatrix} \Lambda_{11} & \Lambda_{12} \\ \Lambda_{21} & \Lambda_{22} \end{bmatrix}^{-1} = \begin{bmatrix} \frac{\Psi_2}{\Psi_2 + 3\Delta\lambda_2 G} & & & & & \\ & \frac{\Psi_1\Psi_2}{\Psi_1\Psi_2 + \Psi_2\Delta\lambda_1 G + 3\Psi_1\Delta\lambda_2 G} & & & & \\ & & 1 & & & \\ & & & \frac{\Psi_1\Psi_2}{\Psi_1\Psi_2 + \Psi_2\Delta\lambda_1 G + 3\Psi_1\Delta\lambda_2 G} & & \\ & & & & 1 & \\ & & & & & 1 \\ & & & & & & 1 \\ & & & & & & & 1 \end{bmatrix}$$

with $G = E / 2(1 + \nu)$. The limit of the mapping matrix, $\Psi_1 \rightarrow 0$ and $\Psi_2 \rightarrow 0$, for isotropic hardening is given by

$$\lim_{\substack{\Psi_1 \rightarrow 0 \\ \Psi_2 \rightarrow 0}} \begin{bmatrix} \mathbf{A}_{11} & \mathbf{A}_{12} \\ \mathbf{A}_{21} & \mathbf{A}_{22} \end{bmatrix}^{-1} = \begin{bmatrix} 1/3 & 1/3 & 1/3 & 0 & 0 & 0 & 0 & 0 \\ 1/3 & 1/3 & 1/3 & 0 & 0 & 0 & 0 & 0 \\ 1/3 & 1/3 & 1/3 & 0 & 0 & 0 & 0 & 0 \\ 0 & 0 & 0 & 0 & 0 & 0 & 0 & 0 \\ 0 & 0 & 0 & 0 & 1 & 0 & 0 & 0 \\ 0 & 0 & 0 & 0 & 0 & 1 & 0 & 0 \\ 0 & 0 & 0 & 0 & 0 & 0 & 1 & 0 \\ 0 & 0 & 0 & 0 & 0 & 0 & 0 & 1 \end{bmatrix} \quad (4.97)$$

which is again the return-mapping to the hydrostatic axis of the stress space. The return-mapping algorithm has been found to be stable although the number of local iterations increases if the trial stress violates the yield function severely in the vertex region of the yield surface. If only the Von Mises yield surface is active the return to the yield surface is achieved in a single iteration which is a property of J_2 -plasticity in a square-root formulation, De Borst (1986), De Borst and Feenstra (1990).

The final issue which has to be treated is the modified stiffness matrix \mathbf{H} for the composite yield function. The case that only the Rankine yield function is active and Ψ_1 is equal to zero has been discussed previously. If only the Von Mises yield function is active and $\Psi_2 \rightarrow 0$, the yield surface reduces to the volumetric stress in the unconstrained stress space and to a single point in the constrained stress space. The limit of the combined yield surface when both yield functions are active is equal to the limit of the single active Von Mises yield function, which has also been shown for the limit of the mapping matrix. Following the same considerations as for the Rankine criterion, the limit of the modified stiffness matrix \mathbf{H} for the Von Mises criterion is given by

$$\lim_{\Psi_2 \rightarrow 0} \mathbf{H} = \lim_{\Psi_2 \rightarrow 0} \mathbf{A}_{11}^{-1} \mathbf{D}_e = \frac{E}{3(1-2\nu)} \begin{bmatrix} 1 & 1 & 1 & 0 \\ 1 & 1 & 1 & 0 \\ 1 & 1 & 1 & 0 \\ 0 & 0 & 0 & 0 \end{bmatrix} \quad (4.98)$$

The consistent tangent stiffness matrix for the limit of the combined yield surface has to be calculated with the limit of the gradient to the yield surface which is not determined. Because the equivalent stress has reduced to zero if the factor Ψ_2 is equal to zero and consequently $\partial \bar{\sigma} / \partial \kappa$ also equals zero, the consistency condition reduces to

$$df_2 = \partial_\sigma f_2^T d\sigma = 0$$

The gradient to the yield surface is always expressed as a vector in the deviatoric plane for associated plastic flow and reads

$$\partial_\sigma f_2 = \beta \mathbf{P}_D \sigma \quad (4.99)$$

with the matrix

$$P_D = \begin{bmatrix} 2 & -1 & -1 & 0 \\ -1 & 2 & -1 & 0 \\ -1 & -1 & 2 & 0 \\ 0 & 0 & 0 & 3 \end{bmatrix}$$

and the scalar β such that a consistent length of the gradient vector is obtained. The total derivative of the updated stress is calculated as

$$d\sigma^{(i+1)} = H [d\varepsilon^{(i+1)} - d\lambda_2 \partial_\sigma f_2]$$

Since the product $H \partial_\sigma f_2$ vanishes in the limit, the consistent tangent is given by

$$d\sigma^{(i+1)} = H d\varepsilon^{(i+1)} \quad (4.100)$$

Clearly, the expansion-compression algorithm does not fail because of dividing by zero, but the tangent stiffness matrix for plane-stress conditions is given by

$$\tilde{D} = \begin{bmatrix} 0 & 0 & 0 \\ 0 & 0 & 0 \\ 0 & 0 & 0 \end{bmatrix}$$

Of course, use of this tangent stiffness matrix may result in numerical difficulties because of the possibility of mechanisms.

4.2 Total formulations

The fundamental difference between the total formulation of the constitutive model and the incremental formulation discussed in the previous paragraphs is the formulation in strains rather than in strain rates. If again an additive decomposition of the total strain vector is assumed into an elastic, reversible part ε_e , and an inelastic, irreversible part ε_c , the strain vector is given by

$$\varepsilon = \varepsilon_e + \varepsilon_c \quad (4.101)$$

The stress vector is given in the final state

$$\sigma = D_e \varepsilon_e \quad (4.102)$$

with D_e the linear-elastic stiffness matrix. The inelastic strain vector is dependent upon the assumption of the constitutive model and is in general a function of the strain vector. In this study two types of total formulations will be used, the deformation theory of plasticity and the elasticity-based total strain crack models.

4.2.1 Deformation theory of plasticity

The fundamental notion of the existence of a yield function is also used in the deformation theory of plasticity and the basic difference with the flow theory is the assumption that the plastic strain vector is given by a total rather than by a rate formulation, i.e.

$$\boldsymbol{\varepsilon}_c = \lambda \partial_{\sigma} f \quad (4.103)$$

with the plastic multiplier λ to be determined by satisfaction of the Kuhn-Tucker conditions

$$\lambda \geq 0$$

$$f(\boldsymbol{\sigma}, \boldsymbol{\eta}, \boldsymbol{q}) \leq 0 \quad (4.104)$$

$$\lambda f(\boldsymbol{\sigma}, \boldsymbol{\eta}, \boldsymbol{q}) = 0$$

The internal variables are again collected in a vector \boldsymbol{q} and evolve according to the general hardening law

$$\boldsymbol{q} = \lambda \boldsymbol{h}(\boldsymbol{\sigma}, \boldsymbol{\eta}, \boldsymbol{q}) \quad (4.105)$$

The system of equations which is obtained after applying the Euler-backward algorithm reads

$$\begin{aligned} \boldsymbol{\varepsilon}^{(i+1)} &= {}^t \boldsymbol{\varepsilon} + \Delta \boldsymbol{\varepsilon}^{(i+1)} \\ \boldsymbol{\sigma}^{(i+1)} &= \boldsymbol{D}_{\varepsilon} (\boldsymbol{\varepsilon}^{(i+1)} - \boldsymbol{\varepsilon}_c^{(i+1)}) \\ \boldsymbol{\varepsilon}_c^{(i+1)} &= \lambda^{(i+1)} \partial_{\sigma} f^{(i+1)} \\ \boldsymbol{q}^{(i+1)} &= \lambda^{(i+1)} \boldsymbol{h}^{(i+1)} \\ \boldsymbol{\eta}^{(i+1)} &= \lambda^{(i+1)} (1 - \gamma) E_{ks} \partial_{\sigma} g^{(i+1)} \end{aligned} \quad (4.106)$$

with E_{ks} the secant stiffness modulus. The discrete Kuhn-Tucker conditions are given by

$$\begin{aligned} \lambda^{(i+1)} &\geq 0 \\ f(\boldsymbol{\sigma}^{(i+1)}, \boldsymbol{\eta}^{(i+1)}, \boldsymbol{q}^{(i+1)}) &\leq 0 \\ \lambda^{(i+1)} f(\boldsymbol{\sigma}^{(i+1)}, \boldsymbol{\eta}^{(i+1)}, \boldsymbol{q}^{(i+1)}) &= 0 \end{aligned} \quad (4.107)$$

If the algorithm is again considered within an elastic predictor-plastic corrector algorithm the elastic trial state is assumed as

$$\begin{aligned}
 \boldsymbol{\varepsilon}_E &= {}^i \boldsymbol{\varepsilon} + \Delta \boldsymbol{\varepsilon}^{(i+1)} \\
 \boldsymbol{\sigma}_E &= \mathbf{D}_e \boldsymbol{\varepsilon}_E \\
 \boldsymbol{\eta}_E &= \mathbf{0} \\
 \mathbf{q}_E &= \mathbf{0}
 \end{aligned} \tag{4.108}$$

with the elastic trial strain vector $\boldsymbol{\varepsilon}_E$ now given by the total strain at time $(i + 1)$ and the assumption that the internal variables, collected in the vector \mathbf{q} , and the back-stress vector $\boldsymbol{\eta}$ are equal to zero, which implies that the nonlinear behavior is completely determined in the considered time step. In the algorithm the total, updated strain vector is applied as the incremental strain vector without updating of the internal variables and the plastic strain vector. Formulated in this fashion, the deformation type plasticity models can be analyzed without major modifications of the algorithm described for the flow theory of plasticity. The only modification is a different definition of the trial state.

The damage in the material is reflected in the internal parameter κ which can be derived from the assumption of work hardening

$$W_c = \boldsymbol{\xi}^T \boldsymbol{\varepsilon}_c = \bar{\sigma}(\gamma \kappa) \kappa$$

which can be elaborated as

$$\lambda = \kappa$$

The tangent stiffness matrix is again developed from the updated stress at $(i + 1)$

$$\boldsymbol{\sigma}^{(i+1)} = \mathbf{D}_e [\boldsymbol{\varepsilon}^{(i+1)} - \lambda^{(i+1)} \partial_{\boldsymbol{\sigma}} f] \tag{4.109}$$

The total derivative then reads

$$d\boldsymbol{\sigma}^{(i+1)} = \mathbf{D}_e [d\boldsymbol{\varepsilon}^{(i+1)} - d\lambda \partial_{\boldsymbol{\sigma}} f - \lambda^{(i+1)} \partial_{\boldsymbol{\sigma}\boldsymbol{\sigma}}^2 f d\boldsymbol{\sigma}^{(i+1)}] \tag{4.110}$$

During the process of plastic loading the consistency condition has to be satisfied

$$df = \partial_{\boldsymbol{\sigma}} f^T d\boldsymbol{\sigma} + \partial_{\boldsymbol{\eta}} f^T d\boldsymbol{\eta} + \partial_{\mathbf{q}} f^T d\mathbf{q} = 0$$

which can be elaborated to

$$d\lambda = \frac{1}{E_s} \partial_\sigma f^T d\sigma^{(i+1)} \quad (4.111)$$

with the hardening parameter

$$E_s = -\partial_q f^T \mathbf{h} + (1 - \gamma) E_k \quad (4.112)$$

The consistent tangent stiffness matrix is finally obtained by substituting eq.(4.111) into eq.(4.110) and reads

$$d\sigma^{(i+1)} = \left[\mathbf{H} - \frac{\mathbf{H} \partial_\sigma f \partial_\sigma f^T \mathbf{H}}{E_s + \partial_\sigma f^T \mathbf{H} \partial_\sigma f} \right] d\epsilon^{(i+1)} \quad (4.113)$$

with the modified stiffness matrix

$$\mathbf{H} = [\mathbf{C}_e + \lambda^{(i+1)} \partial_{\sigma\sigma}^2 f]^{-1} \quad (4.114)$$

The limit of the consistent tangent stiffness matrix discussed for the models based on the flow theory of plasticity is also valid for deformation type plasticity, because the structure of the yield function remains unaltered.

4.2.2 Co-rotational formulation

The co-rotational formulation is usually related to the elasticity-based rotating crack model, Willam, Pramono and Sture (1986), Rots (1988), Crisfield and Wills (1989). In this study the co-rotational formulation is used with the assumption that the local constitutive model which describes the relation between the local stress vector and the local strain vector, is transformed into the global coordinate system with a transformation matrix which is determined by the principal directions of the strain vector. The strain vector in the global coordinate system ϵ is updated as

$$\epsilon^{(i+1)} = {}^t \epsilon + \Delta \epsilon^{(i+1)} \quad (4.115)$$

which is transformed to the strain vector in the local coordinate system $\epsilon_{n,s}$ with the strain transformation matrix $T(\phi)$

$$\epsilon_{n,s}^{(i+1)} = T(\phi) \epsilon^{(i+1)} \quad (4.116)$$

with

$$T(\phi) = \begin{bmatrix} \cos^2 \phi & \sin^2 \phi & 0 & \sin \phi \cos \phi \\ \sin^2 \phi & \cos^2 \phi & 0 & -\sin \phi \cos \phi \\ 0 & 0 & 1 & 0 \\ -2 \sin \phi \cos \phi & 2 \sin \phi \cos \phi & 0 & \cos^2 \phi - \sin^2 \phi \end{bmatrix}$$

The constitutive model has to be formulated in the local coordinate system and should give a relation between the local strain vector $\epsilon_{n,s}$ and the local stress vector $\sigma_{n,s}$. In an unconstrained stress situation the general format reads

$$\sigma_{n,s}^{(i+1)} = D(\epsilon_{n,s}) \epsilon_{n,s}^{(i+1)} \quad (4.117)$$

The updated stress vector in the global coordinate system is then given by

$$\sigma^{(i+1)} = T(\phi)^T \sigma_{n,s}^{(i+1)} \quad (4.118)$$

This general formulation does not necessarily maintain co-axiality, because the principal axes of stress do not need to coincide with the principal axes of strain. The formulation presented here is merely a framework for the treatment of the rotating and the fixed crack models within a total strain formulation, in order to compare the incremental and total approaches.

The constitutive model before cracking is usually assumed to be governed by a linear-elastic model with a Young's modulus and a Poisson ratio unequal to zero. After crack initiation the Poisson effect is usually neglected and the Poisson ratio is set equal to zero. The post-crack behavior is then described by an orthotropic, uncoupled stiffness matrix, i.e.

$$\begin{Bmatrix} \sigma_{nn} \\ \sigma_{ss} \\ \sigma_{tt} \\ \sigma_{ns} \end{Bmatrix} = \begin{bmatrix} E_n(\epsilon_{nn}) & 0 & 0 & 0 \\ 0 & E_s(\epsilon_{ss}) & 0 & 0 \\ 0 & 0 & E_t(\epsilon_{tt}) & 0 \\ 0 & 0 & 0 & \beta G \end{bmatrix} \begin{Bmatrix} \epsilon_{nn} \\ \epsilon_{ss} \\ \epsilon_{tt} \\ \gamma_{ns} \end{Bmatrix}$$

Although the assumption of zero Poisson ratio after cracking is generally accepted in the literature, it seems rather arbitrary. The usual engineering approach to the problem is to define the stresses directly as a function of the strain components with an equivalent uniaxial stress-strain model, Crisfield and Wills (1989), Cervenka, Pukl and Eligehausen (1990), but with this approach a comparison between the different formulations would not be sensible. Therefore it is assumed in this study that the Poisson effect remains after cracking as has also been assumed for the incremental formulations.

The constitutive model based on a total formulation is most conveniently developed with the assumption of a bounding surface for each stress component which reads

$$f_j = \sigma_j - \bar{\sigma}_j \quad (4.119)$$

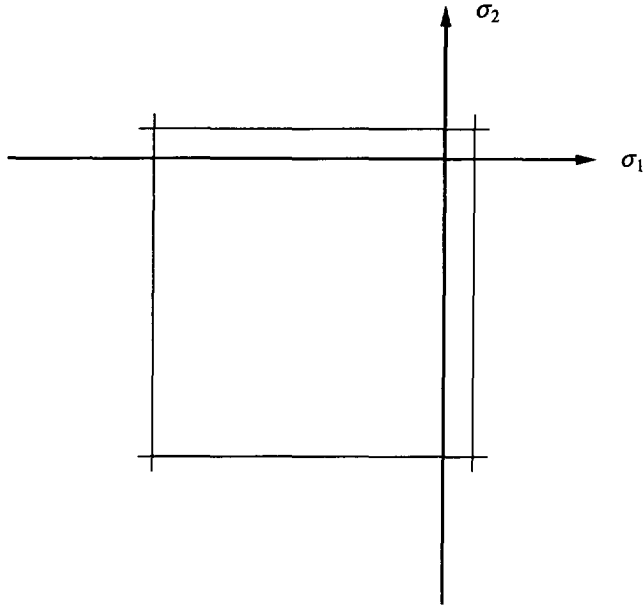


Figure 4.8 Failure surface in principal stress space

in which $\bar{\sigma}_j$ the equivalent stress. This formulation allows for a consistent treatment of the Poisson effect after crack initiation without difficulties in a multi-axial strain situation. The formulation results in an algorithm which is equivalent to the return-mapping procedure used in the mathematical plasticity theory. The stress state is bounded by seven independent functions, three in tension, three in compression and one in shear, i.e.

$$\left\{ \begin{array}{l} f_1 = \sigma_{nn} - \bar{\sigma}_1 = 0 \\ f_2 = \sigma_{ss} - \bar{\sigma}_2 = 0 \\ f_3 = \sigma_{tt} - \bar{\sigma}_3 = 0 \\ f_4 = |\sigma_{ns}| - \bar{\sigma}_4 = 0 \\ f_5 = -\sigma_{nn} - \bar{\sigma}_5 = 0 \\ f_6 = -\sigma_{ss} - \bar{\sigma}_6 = 0 \\ f_7 = -\sigma_{tt} - \bar{\sigma}_7 = 0 \end{array} \right. \quad (4.120)$$

The behavior in shear is assumed to be equal in positive and negative shear stresses. The resulting failure surface is depicted in Figure 4.8 for a principal stress space. The total formulation has a draw-back that unloading and reloading cannot be modeled by in a plasticity-like format. Although this study does not consider cyclic loading, where it is of utmost importance to model the hysteresis, Hordijk (1991), it is still possible that at a local level unloading takes place due to redistribution of the stresses in the structure. However, it is relatively simple to model unloading and reloading in a total strain

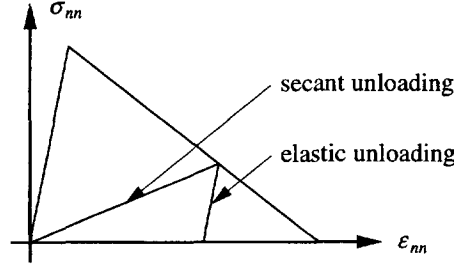


Figure 4.9 Unloading models.

formulation with unloading constraints based on the maximum strain in the direction which is considered. Because the loading/unloading conditions are a function of the updated strain components, the conditions are known before the calculation of the updated stress vector which implies that unloading can be taken into account by a modification of the equivalent stress $\bar{\sigma}_j$. In this study two types of unloading will be considered, i.e. secant and elastic unloading, see Figure 4.9, which can be considered as the two extremes of the true unloading model, Rots (1988). Introducing the vectors

$$\begin{aligned} \mathbf{v}_1 &= \{ 1, 0, 0, 0 \}^T \\ \mathbf{v}_2 &= \{ 0, 1, 0, 0 \}^T \\ \mathbf{v}_3 &= \{ 0, 0, 1, 0 \}^T \\ \mathbf{v}_4 &= \{ 0, 0, 0, \frac{\sigma_{ns}}{|\sigma_{ns}|} \}^T \\ \mathbf{v}_5 &= \{ -1, 0, 0, 0 \}^T \\ \mathbf{v}_6 &= \{ 0, -1, 0, 0 \}^T \\ \mathbf{v}_7 &= \{ 0, 0, -1, 0 \}^T \end{aligned}$$

the general definition of the bounding surfaces is given by

$$f_j = \mathbf{v}_j^T \boldsymbol{\sigma}_{n,s} - \bar{\sigma}_j(\kappa_j, \boldsymbol{\varepsilon}_{n,s}) \quad (4.121)$$

With this notation, secant unloading can be modeled with the modification of the equivalent stress given by

$$\bar{\sigma}_j = \bar{\sigma}_j(\kappa_j^{(i+1)}) \left(1 - r_j \frac{\mathbf{v}_j^T (\boldsymbol{\varepsilon}_{n,s}^{\max} - \boldsymbol{\varepsilon}_{n,s}^{(i+1)})}{\mathbf{v}_j^T \boldsymbol{\varepsilon}_{n,s}^{\max}} \right) \quad (4.122)$$

and elastic unloading can be modeled with the relation

$$\bar{\sigma}_j = \bar{\sigma}_j(\kappa_j^{(i+1)}) \left(1 - r_j \frac{E_c}{\bar{\sigma}_j(\kappa_j^{(i+1)})} \mathbf{v}_j^T (\boldsymbol{\varepsilon}_{n,s}^{\max} - \boldsymbol{\varepsilon}_{n,s}^{(i+1)}) \right) \quad (4.123)$$

The maximum strain components $\varepsilon_{n,s}^{\max}$ are determined by the unloading constraints r_j which are defined by

$$r_j = \begin{cases} 0 & \text{if } |\varepsilon_j^{(i+1)}| > |\varepsilon_j^{\max}| \\ 1 & \text{if } |\varepsilon_j^{(i+1)}| \leq |\varepsilon_j^{\max}| \end{cases} \quad (4.124)$$

The equivalent stress $\bar{\sigma}_j$ is now considered as a function of an internal parameter κ_j and of the total strain vector in the local coordinate system $\boldsymbol{\varepsilon}_{n,s}$. The nonlinear material behavior due to internal damage of the material is then assumed to be governed by seven internal damage parameters, collected in a vector $\mathbf{q} = \{\kappa_1, \kappa_2, \dots, \kappa_7\}^T$ which are also assumed to be a function of the total strain vector in the local coordinate system, given by the relation

$$\mathbf{q}^{(i+1)} = \mathbf{M} \boldsymbol{\varepsilon}_{n,s}^{\max} \quad (4.125)$$

with $\varepsilon_{n,s}^{\max}$ the maximum strains in the local coordinate system. The coupling between damage in different directions is now possible in a transparent manner by setting the off-diagonal terms in matrix \mathbf{M} unequal to zero. In case of no coupling the matrix \mathbf{M} is given by

$$\mathbf{M} = \begin{bmatrix} 1 & 0 & 0 & 0 & 0 & 0 & 0 \\ 0 & 1 & 0 & 0 & 0 & 0 & 0 \\ 0 & 0 & 1 & 0 & 0 & 0 & 0 \\ 0 & 0 & 0 & 1 & 0 & 0 & 0 \\ 0 & 0 & 0 & 0 & -1 & 0 & 0 \\ 0 & 0 & 0 & 0 & 0 & -1 & 0 \\ 0 & 0 & 0 & 0 & 0 & 0 & -1 \end{bmatrix}$$

The evolution of the internal parameters is now expressed as

$$\mathbf{q}^{(i+1)} = \mathbf{W} \boldsymbol{\varepsilon}_{n,s}^{(i+1)}$$

in which the matrix $\mathbf{W} = \mathbf{M} \mathbf{U}$ with

$$U = \begin{bmatrix} 1-r_1 & 0 & 0 & 0 \\ 0 & 1-r_2 & 0 & 0 \\ 0 & 0 & 1-r_3 & 0 \\ 0 & 0 & 0 & 1 \\ 1-r_5 & 0 & 0 & 0 \\ 0 & 1-r_6 & 0 & 0 \\ 0 & 0 & 1-r_7 & 0 \end{bmatrix}$$

The updated stress vector can be calculated using a return-mapping algorithm if the active failure surfaces have been determined. The updated stress vector is given by

$$\sigma_{n,s}^{(i+1)} = D_e \epsilon_{e,n,s}^{(i+1)} = D_e (\epsilon_{n,s}^{(i+1)} - \epsilon_{c,n,s}^{(i+1)}) \quad (4.126)$$

in which the inelastic strain vector $\epsilon_{c,n,s}^{(i+1)}$ is determined by the summation of the inelastic strain vectors of the different active directions,

$$\epsilon_{c,n,s}^{(i+1)} = \sum_{j=1}^7 c_j \lambda_j^{(i+1)} \partial_{\sigma} f_j = \sum_{j=1}^7 c_j \lambda_j^{(i+1)} \mathbf{v}_j \quad (4.127)$$

with c_j the constraint which is equal to one if the failure surface is active else the constraint is equal to zero. The updated stress vector is then given by

$$\sigma_{n,s}^{(i+1)} = D_e \epsilon_{n,s}^{(i+1)} - \sum_{j=1}^7 c_j \lambda_j^{(i+1)} D_e \mathbf{v}_j \quad (4.128)$$

The inelastic multipliers λ_j are calculated by substituting the updated stress vector into the formulation of the bounding surface, eq.(4.121) which results in

$$c_i f_i = c_i \mathbf{v}_i^T D_e \epsilon_{n,s}^{(i+1)} - \sum_{j=1}^7 c_i c_j \lambda_j^{(i+1)} \mathbf{v}_i^T D_e \mathbf{v}_j$$

which is a linear set of equations

$$\mathbf{A} \mathbf{x} = \mathbf{b} \quad (4.129)$$

with

$$\begin{aligned} A_{ij} &= c_i c_j \mathbf{v}_i^T D_e \mathbf{v}_j \\ x_i &= \lambda_i \\ b_i &= c_i (\mathbf{v}_i^T D_e \epsilon_{n,s} - \bar{\sigma}_i(\kappa_i, \epsilon_{n,s})) \end{aligned}$$

from which λ_j can be solved. The updated stress vector $\sigma_{n,s}^{(i+1)}$ can be calculated with eq.(4.128) by substituting the inelastic multipliers λ_j .

The tangent stiffness matrix is derived consistently with the Newton-Raphson iteration scheme for obtaining global equilibrium starting from the updated stress vector in the global coordinate system

$$\sigma^{(i+1)} = T(\phi)^T \sigma_{n,s}^{(i+1)}$$

The total derivative of the updated stress is given by

$$d\sigma^{(i+1)} = d(T(\phi)^T) \sigma_{n,s}^{(i+1)} + T(\phi)^T d\sigma_{n,s}^{(i+1)} \quad (4.130)$$

With the angle $\phi = \phi(\epsilon)$ this can be written as

$$d\sigma^{(i+1)} = \left[\frac{\partial T(\phi)^T}{\partial \phi} \sigma_{n,s}^{(i+1)} \frac{\partial \phi^T}{\partial \epsilon^{(i+1)}} + T(\phi)^T \frac{\partial \sigma_{n,s}^{(i+1)}}{\partial \epsilon_{n,s}^{(i+1)}} \frac{\partial \epsilon_{n,s}^{(i+1)}}{\partial \epsilon^{(i+1)}} \right] d\epsilon^{(i+1)}$$

The strain vector in the local coordinate system has been defined previously as

$$\epsilon_{n,s}^{(i+1)} = T(\phi) \epsilon^{(i+1)}$$

so that

$$\frac{\partial \epsilon_{n,s}}{\partial \epsilon} = \frac{\partial T(\phi)}{\partial \phi} \epsilon \frac{\partial \phi^T}{\partial \epsilon} + T(\phi)$$

Substituting this relation into the tangent stiffness relation results in

$$\begin{aligned} d\sigma^{(i+1)} = & \left[T(\phi)^T \frac{\partial \sigma_{n,s}^{(i+1)}}{\partial \epsilon_{n,s}^{(i+1)}} T(\phi) \right] d\epsilon^{(i+1)} + \left[\frac{\partial T(\phi)^T}{\partial \phi} \sigma_{n,s}^{(i+1)} \frac{\partial \phi^T}{\partial \epsilon^{(i+1)}} \right] d\epsilon^{(i+1)} \\ & + \\ & \left[T(\phi)^T \frac{\partial \sigma_{n,s}^{(i+1)}}{\partial \epsilon_{n,s}^{(i+1)}} \frac{\partial T(\phi)}{\partial \phi} \epsilon^{(i+1)} \frac{\partial \phi^T}{\partial \epsilon^{(i+1)}} \right] d\epsilon^{(i+1)} \end{aligned} \quad (4.131)$$

The first term of the tangent stiffness matrix is equal to the tangent stiffness matrix in the local coordinate system transformed into the global coordinate system and can be considered as the material tangent stiffness matrix. The second and third terms are due to the spin of the local coordinate system. If the total strain model is considered as a fixed crack model, the transformation matrix is no longer a function of the strain vector in the global coordinate system and the second and third term of the tangent stiffness matrix vanish.

The local material tangent stiffness matrix is derived consistently from the updated

local stress vector

$$\boldsymbol{\sigma}_{n,s}^{(i+1)} = \mathbf{D}_e \boldsymbol{\varepsilon}_{n,s}^{(i+1)} - \sum_{j=1}^7 c_j \lambda_j^{(i+1)} \mathbf{D}_e \mathbf{v}_j \quad (4.132)$$

The total derivative is given by

$$d\boldsymbol{\sigma}_{n,s}^{(i+1)} = \mathbf{D}_e d\boldsymbol{\varepsilon}_{n,s}^{(i+1)} - \sum_{j=1}^7 c_j d\lambda_j^{(i+1)} \mathbf{D}_e \mathbf{v}_j \quad (4.133)$$

The consistency condition $df_i = 0$ gives the final relation between the variation of the inelastic multiplier $d\lambda$ and the strain variation

$$df_i = c_i (\mathbf{v}_i^T d\boldsymbol{\sigma}_{n,s}^{(i+1)} + \partial_q f_i^T d\mathbf{q}^{(i+1)} + \partial_\varepsilon f_i^T d\boldsymbol{\varepsilon}_{n,s}^{(i+1)}) = 0 \quad (4.134)$$

Substitution of eq.(4.133) results in

$$c_i (\mathbf{v}_i^T \mathbf{D}_e d\boldsymbol{\varepsilon}_{n,s}^{(i+1)} - \mathbf{v}_i^T \sum_{j=1}^7 c_j d\lambda_j^{(i+1)} \mathbf{D}_e \mathbf{v}_j + \partial_q f_i^T d\mathbf{q}^{(i+1)} + \partial_\varepsilon f_i^T d\boldsymbol{\varepsilon}_{n,s}^{(i+1)}) = 0 \quad (4.135)$$

which can be solved to obtain the variation of the inelastic multipliers $d\lambda_j$. The total derivative of the internal parameters is given by the relation

$$d\mathbf{q}^{(i+1)} = \mathbf{W} d\boldsymbol{\varepsilon}_{n,s}^{(i+1)} \quad (4.136)$$

because the matrix \mathbf{W} is a constant matrix. Substitution of eq.(4.136) into eq.(4.135) results in the system of equations

$$\mathbf{A} \mathbf{x} = \mathbf{b} \quad (4.137)$$

with

$$\begin{aligned} A_{ij} &= c_i c_j \mathbf{v}_i^T \mathbf{D}_e \mathbf{v}_j \\ x_i &= d\lambda_i \\ b_i &= c_i (\mathbf{v}_i^T \mathbf{D}_e + \partial_q f_i^T \mathbf{W} + \partial_\varepsilon f_i^T) d\boldsymbol{\varepsilon}_{n,s}^{(i+1)} \end{aligned}$$

which can be solved for $d\lambda_i$. The variation of the inelastic multipliers is now given by

$$d\lambda_j^{(i+1)} = \sum_{k=1}^7 A_{jk}^{-1} b_k$$

which can be substituted in eq.(4.133) resulting in the local tangent stiffness matrix

$$d\sigma_{n,s}^{(i+1)} = \left[D_e - \sum_{j=1}^7 c_j D_e v_j \sum_{k=1}^7 c_k A_{jk}^{-1} \left(v_k^T D_e + \partial_q f_k^T W \partial_\varepsilon f_k^T \right) \right] d\varepsilon_{n,s}^{(i+1)}$$

which is in general nonsymmetric.

In case of secant unloading the derivatives of the functions with respect to the internal parameters and with respect to the strain vector are given by

$$\partial_q f_k = - \frac{\partial \bar{\sigma}_k(\kappa_k)}{\partial q} \left((1 - r_k) + r_k \frac{v_k^T \varepsilon_{n,s}^{(i+1)}}{v_k^T \varepsilon_{n,s}^{\max}} \right) \quad (4.138)$$

and

$$\partial_\varepsilon f_k = - \bar{\sigma}_k(\kappa_k) r_k \frac{|v_k|}{v_k^T \varepsilon_{n,s}^{\max}} \quad (4.139)$$

respectively. If elastic unloading is assumed, the derivatives are given by

$$\partial_q f_k = - \frac{\partial \bar{\sigma}_k(\kappa_k)}{\partial q} \quad (4.140)$$

and

$$\partial_\varepsilon f_k = - r_k E_c |v_k| \quad (4.141)$$

respectively.

The second term in the tangent stiffness matrix, eq.(4.131), can be elaborated for the coaxial rotating crack model by the calculation of the partial derivative of the transformation matrix T to the rotating angle ϕ

$$\frac{\partial T^T}{\partial \phi} = \begin{bmatrix} -\sin 2\phi & \sin 2\phi & 0 & -2 \cos 2\phi \\ \sin 2\phi & -\sin 2\phi & 0 & 2 \cos 2\phi \\ 0 & 0 & 0 & 0 \\ \cos 2\phi & -\cos 2\phi & 0 & -2 \sin 2\phi \end{bmatrix} \quad (4.142)$$

in which the angle ϕ is given by the coaxiality condition

$$\phi = 1/2 \operatorname{atan}\left(\frac{\gamma_{xy}}{\varepsilon_{xx} - \varepsilon_{yy}} \right) \quad (4.143)$$

The partial derivative of the angle ϕ to the global strain vector is given by

$$\frac{\partial \phi}{\partial \epsilon} = \begin{Bmatrix} \frac{-1/2 \gamma_{xy}}{(\epsilon_{xx} - \epsilon_{yy})^2 + \gamma_{xy}^2} \\ \frac{1/2 \gamma_{xy}}{(\epsilon_{xx} - \epsilon_{yy})^2 + \gamma_{xy}^2} \\ 0 \\ \frac{1/2(\epsilon_{xx} - \epsilon_{yy})}{(\epsilon_{xx} - \epsilon_{yy})^2 + \gamma_{xy}^2} \end{Bmatrix} \quad (4.144)$$

Because the shear stress in the local coordinate system σ_{ns} is equal to zero by definition, the second term of the tangent stiffness matrix, eq.(4.131), can be expressed as

$$\left[\frac{\partial T(\phi)^T}{\partial \phi} \sigma_{n,s} \frac{\partial \phi^T}{\partial \epsilon} \right] = \frac{1/2 \gamma_{xy} (\sigma_{nn} - \sigma_{ss})}{(\epsilon_{xx} - \epsilon_{yy})^2 + \gamma_{xy}^2} \begin{bmatrix} \sin 2\phi & -\sin 2\phi & 0 & -\cos 2\phi \\ -\sin 2\phi & \sin 2\phi & 0 & \cos 2\phi \\ 0 & 0 & 0 & 0 \\ -\cos 2\phi & \cos 2\phi & 0 & \frac{\cos^2 2\phi}{\sin 2\phi} \end{bmatrix} \quad (4.145)$$

This equation is not very convenient in a finite element program where it is more appropriate to develop the tangent stiffness matrix in the local coordinate system and then transform the matrix to the global coordinate system. Using multiple-angle transformations, it follows that

$$\frac{1/2 \gamma_{xy} (\sigma_{nn} - \sigma_{ss})}{(\epsilon_{xx} - \epsilon_{yy})^2 + \gamma_{xy}^2} = 1/2 \sin 2\phi \frac{\sigma_{nn} - \sigma_{ss}}{\epsilon_{nn} - \epsilon_{ss}}$$

and the second part of the tangent stiffness matrix, eq.(4.131), is finally written as

$$\left[\frac{\partial T(\phi)^T}{\partial \phi} \sigma_{n,s} \frac{\partial \phi^T}{\partial \epsilon} \right] = T^T(\phi) \begin{bmatrix} 0 & 0 & 0 & 0 \\ 0 & 0 & 0 & 0 \\ 0 & 0 & 0 & 0 \\ 0 & 0 & 0 & \omega \end{bmatrix} T(\phi) \quad (4.146)$$

with

$$\omega = 1/2 \frac{\sigma_{nn} - \sigma_{ss}}{\epsilon_{nn} - \epsilon_{ss}}$$

which has also been given by Bažant (1983), Willam, Pramono and Sture (1987), Rots (1988), Crisfield and Wills (1989).

The third part of the tangent stiffness matrix, eq.(4.131),

$$\left[T(\phi)^T \frac{\partial \sigma_{n,s}}{\partial \epsilon_{n,s}} \frac{\partial T(\phi)}{\partial \phi} \epsilon \frac{\partial \phi^T}{\partial \epsilon} \right]$$

can be reduced in the same manner. We firstly apply the multiple angle transformations to the matrix-vector product

$$\frac{\partial T(\phi)}{\partial \phi} \epsilon = \begin{Bmatrix} 0 \\ 0 \\ 0 \\ -2 \cos 2\phi \frac{(\epsilon_{xx} - \epsilon_{yy})^2 + \gamma_{xy}^2}{\epsilon_{xx} - \epsilon_{yy}} \end{Bmatrix} \quad (4.147)$$

Multiplication with the vector $\frac{\partial \phi^T}{\partial \epsilon}$ then results in

$$\frac{\partial T(\phi)}{\partial \phi} \epsilon \frac{\partial \phi^T}{\partial \epsilon} = \begin{bmatrix} 0 & 0 & 0 & 0 \\ 0 & 0 & 0 & 0 \\ 0 & 0 & 0 & 0 \\ \sin 2\phi & \sin 2\phi & 0 & -\cos 2\phi \end{bmatrix} \quad (4.148)$$

which is equal to

$$\begin{bmatrix} 0 & 0 & 0 & 0 \\ 0 & 0 & 0 & 0 \\ 0 & 0 & 0 & 0 \\ 0 & 0 & 0 & -1 \end{bmatrix} T(\phi) = -L T(\phi) \quad (4.149)$$

with the diagonal matrix $L = \text{diag} [0, 0, 0, 1]$. The consistent tangent stiffness matrix is now completely defined as

$$d\sigma^{(i+1)} = \left[T(\phi)^T \frac{\partial \sigma_{n,s}}{\partial \epsilon_{n,s}} (I - L) T(\phi) + T(\phi)^T \omega L T(\phi) \right] d\epsilon^{(i+1)} \quad (4.150)$$

These derivations are valid if the strain transformation matrix $T(\phi)$ is indeed a function of the total strain vector and if we assume a coaxial rotating crack model. For the fixed crack model, the consistent tangent stiffness matrix is simply given by

$$d\sigma^{(i+1)} = \left[T(\phi)^T \frac{\partial \sigma_{n,s}}{\partial \epsilon_{n,s}} T(\phi) \right] d\epsilon^{(i+1)} \quad (4.151)$$

and the reduced shear stiffness βG is determined by a function which is in general a

function of the normal and shear strain component. In this study it is assumed that the shear retention factor remains constant after the tensile strength has been violated.

4.3 Tension-shear model problem

The fundamental differences of the formulations discussed in this Chapter will be discussed with an elementary problem proposed by Willam, Pramono and Sture (1986), in which a plane-stress element with unit dimensions is loaded in biaxial tension and shear. This causes a continuous rotation of the principal strain axes after cracking, as is typical of crack propagation in smeared crack finite element analysis. The element is subjected to tensile straining in the x -direction accompanied by lateral Poisson contraction in the y -direction to simulate uniaxial loading. Immediately after the tensile strength has been violated, the element is loaded in combined biaxial tension and shear strain, see Figure 4.10. The ratio between the different strain components is given by $\Delta\epsilon_{xx} : \Delta\epsilon_{yy} : \Delta\gamma_{xy} = 0.5 : 0.75 : 1$. The material properties are given in Table 4.1. The analyses of Rots (1988) of this problem with the multi-directional crack model show that the shear response becomes softer with decreasing threshold angle, resulting in the limiting case of the rotating crack model with zero threshold angle as the most flexible response.

Table 4.1 Material properties tension-shear model problem.

	concrete	
E_c	10000	[N/mm ²]
ν	0.2	[-]
$f_{ct,m}$	1.0	[N/mm ²]
G_f	$0.15 \cdot 10^{-3}$ ¹⁾	[Nmm/mm ²]

1) linear softening

The behavior of the different formulations for smeared cracking which have been given in this study can be studied in detail with this problem. The constitutive behavior will be compared with respect to the shear stress - shear strain behavior and the normal stress - normal strain behavior in the x - and y -directions. Particularly the shear stress - shear strain response gives a good impression of the behavior of the model when applied to the analyses of structures. The first issue which will be treated is the different behavior of the models formulated in the total strain concept. The comparison between the rotating crack model and the fracture energy-based Rankine model with isotropic and kinematic hardening should elucidate if the fracture energy-based plasticity model is capable to predict a flexible shear stress - shear strain response. The second issue is the comparison of the rotating crack model and the fracture energy-based plasticity model within an incremental formulation. Because the response of models with a total

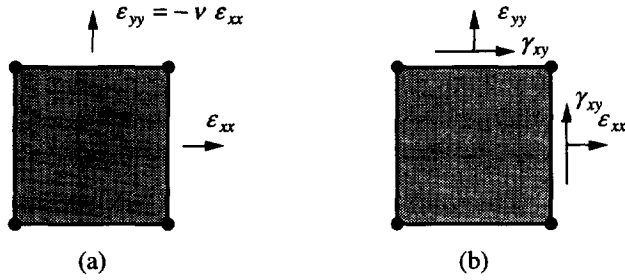


Figure 4.10 Tension - shear model problem: (a) tension up to cracking; (b) biaxial tension with shear beyond cracking.

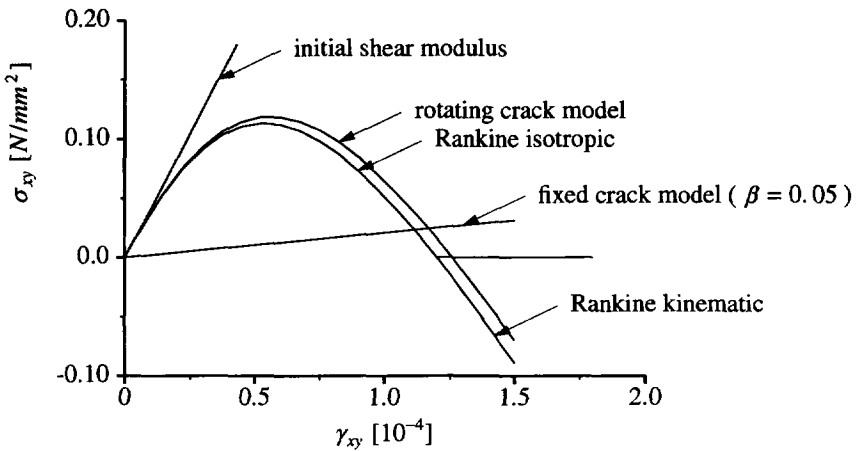


Figure 4.11 Total formulation of the constitutive models. $\sigma_{xy} - \gamma_{xy}$ response.

formulation is in general more flexible than the response of models with an incremental formulation, we expect that the Rankine plasticity model with an incremental formulation shows a less flexible shear stress - shear strain response, but the comparison should provide insight if this less flexible response is still acceptable.

4.3.1 Comparison of the total formulations

The shear stress - shear strain response for the different models described in a total formulation is shown in Figure 4.11. The fixed crack model has been used with a shear-retention factor equal to 0.05 which results in a constant increasing shear stress with increasing shear strain. The rotating crack model shows an implicit shear softening behavior which has been observed previously by Willam, Pramono and Sture (1985) and Rots (1988). It is interesting that the same behavior occurs for the fracture energy-based

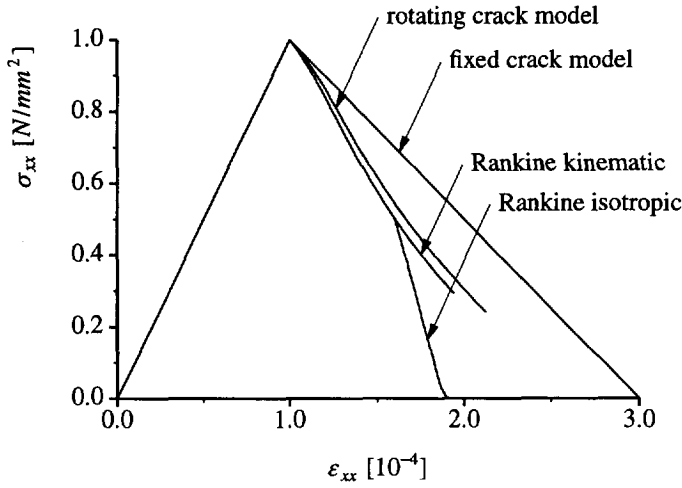


Figure 4.12 Total formulation of the constitutive models. $\sigma_{xx} - \varepsilon_{xx}$ response.

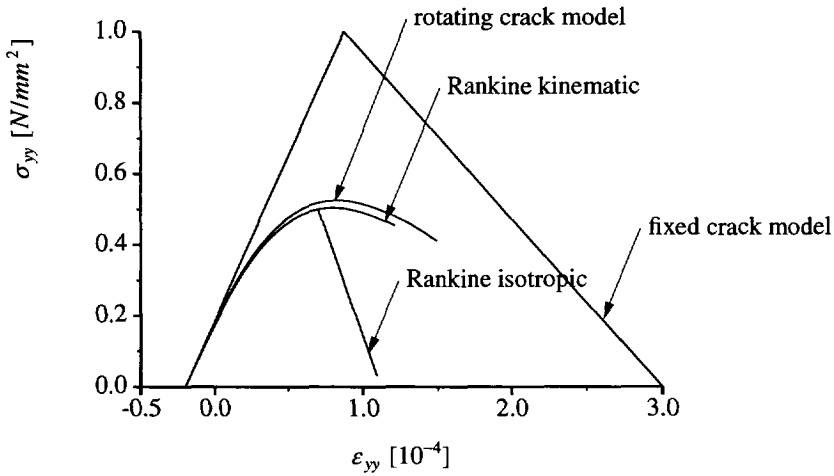


Figure 4.13 Total formulation of the constitutive models. $\sigma_{yy} - \varepsilon_{yy}$ response.

plasticity model with isotropic and kinematic hardening. The two formulations are in fact indiscernible until the shear stress has almost softened completely. Then the isotropic and the kinematic hardening models yield different responses which is due to the fact that with isotropic hardening it is impossible for the shear stress to become negative for positive increments of the shear strain component of the strain vector. It is obvious from Figure 4.11 that the differences between the rotating crack model, except for the fixed crack model, are very small.

The $\sigma_{xx} - \varepsilon_{xx}$ response depicted in Figure 4.12 shows that the input stress-strain softening diagram is exactly reproduced by the fixed crack model. This is logical, since the

softening has been monitored in the fixed crack directions which are aligned with the x - y -axes. The behavior of the other models shows an implicit normal stress-shear stress coupling. The Rankine plasticity model with isotropic hardening shows an increasing degradation of the stiffness when the stress has been decreased until approximately 50 % which is attended with a zero shear stress. At this stage the apex of the yield surface has been reached and the stress components in x and y -direction are softening in the direction of the origin. The response in the lateral y -direction is shown in Figure 4.13 which shows the formation of a secondary crack perpendicular to the first crack for the fixed crack model which again reflects the input softening diagram. The rotating crack model and the Rankine plasticity model with kinematic hardening show a gradual degradation of the stiffness in the y -direction. This can also be observed for the Rankine plasticity model with isotropic softening until the shear stress becomes equal to zero and the stress in y -direction begins to soften linearly which is in accordance with the input softening diagram.

The performance of the constitutive models based on a total formulation has been shown with the elementary tension-shear model problem. The formulation of a maximum principal stress criterion within the framework of elasticity or within the framework of plasticity does not result in major differences. In particular, the elasticity-based rotating crack model and the fracture energy-based Rankine plasticity model with kinematic hardening show an almost identical behavior. The behavior of the Rankine model with isotropic hardening is identical to the behavior of the Rankine model with kinematic hardening until the shear stress is equal to zero. At that stage the apex of the yield surface has been reached for the isotropic hardening model and the shear stress is equal to zero.

4.3.2 Comparison of incremental formulations with the rotating crack model

The limiting case with no softening ($G_f = \infty$) confirms that the different formulations within the total strain concept result in a similar behavior. The shear stress-shear strain responses of the rotating crack model and the Rankine plasticity model are shown in Figure 4.14. The response is identical for all models with a total formulation. It is clear from this figure that although no softening has been assumed, the shear stress-shear strain response shows an implicit softening behavior. Also depicted in Figure 4.14 is the response of the Rankine model formulated within an incremental concept, which shows a shear stress-shear strain response that is less flexible, but still shows an implicit shear softening. The coincidence between the rotating crack model and the Rankine plasticity model based on the deformation theory when compared for ideal plasticity has also been shown by Crisfield and Wills (1989). The plasticity model based on an incremental formulation has also been applied to the tension-shear model problem with the material properties given in Table 4.1 and compared with the rotating crack model in the

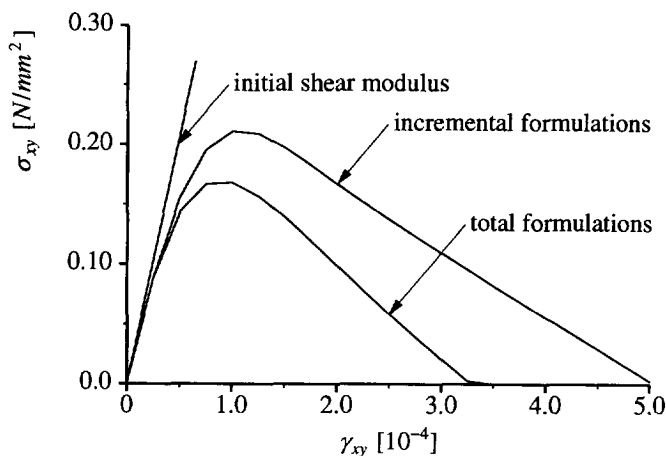


Figure 4.14 $G_f = \infty$. $\sigma_{xy} - \gamma_{xy}$ response.

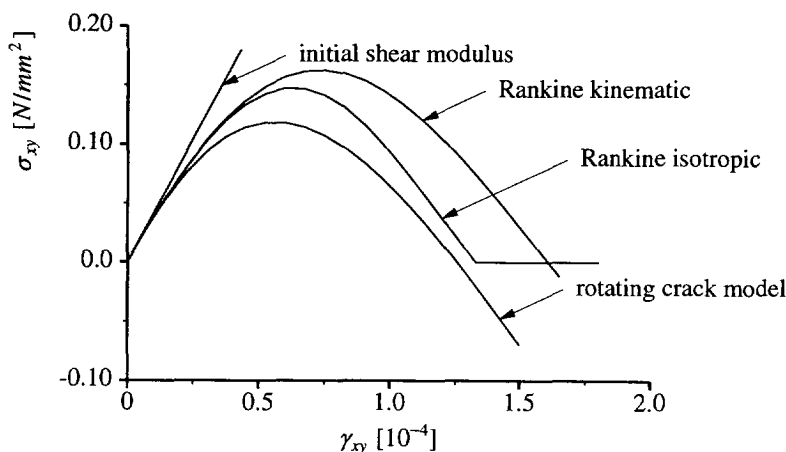


Figure 4.15 Tangential formulations and the rotating crack model. $\sigma_{xy} - \gamma_{xy}$ response.

following figures. The first interest concerns the behavior in shear which is depicted in Figure 4.15. It is clear from Figure 4.15 that the rotating crack model has the most flexible response in shear, but the differences between the rotating crack model and the fracture energy-based plasticity model are minor. Again, the Rankine plasticity model with isotropic hardening results in a shear stress equal to zero when the apex of the yield surface has been reached.

The normal stress-strain response in the x -direction, see Figure 4.16, again shows an implicit normal stress-shear stress coupling for the models based on an incremental formulation, with an even more pronounced coupling for the fracture energy-based plasticity model.

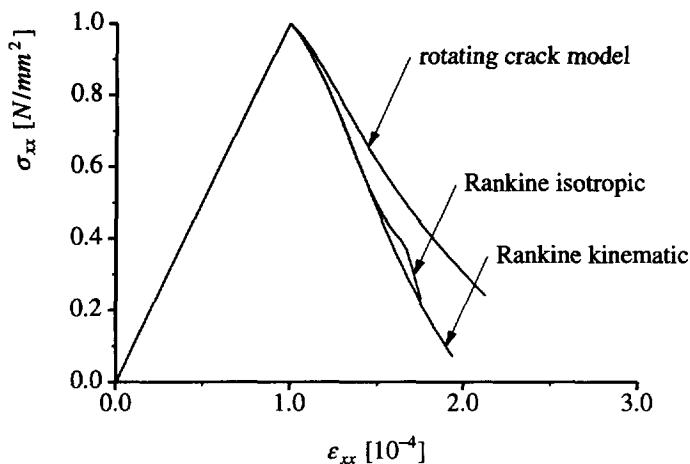


Figure 4.16 Tangential formulations and the rotating crack model. $\sigma_{xx} - \varepsilon_{xx}$ response.

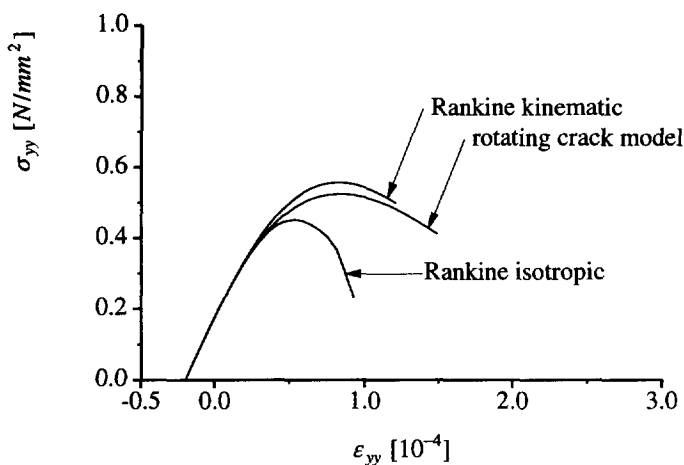


Figure 4.17 Tangential formulations and the rotating crack model. $\sigma_{yy} - \varepsilon_{yy}$ response.

The normal stress-normal strain response in the lateral direction, depicted in Figure 4.17 shows a similar behavior as for the models based on the total formulation, given in Figure 4.13. The response for the Rankine plasticity model with isotropic hardening again shows the linear softening relation when the apex of the yield surface has been reached. The response of the Rankine plasticity model with kinematic hardening shows a gradual degradation of the stiffness in the y -direction.

4.4 Summary

It has been shown that fracture energy-based plasticity models and the rotating crack model have a strong correlation. The Rankine model within an incremental formulation shows a similar behavior as the rotating crack model, which indicates that this model can be used to model crack formation in concrete. The differences between the Rankine model with kinematic and isotropic hardening are surprisingly small in the case of proportional loading. In the next Chapter, the rotating crack model and the fracture energy-based plasticity model with isotropic and kinematic hardening will be applied in the analysis of plain concrete structures to further compare the different approaches.

Appendix: Axisymmetrical formulation of the composite yield criterion

The composite yield contour which is composed of a Rankine criterion and a Von Mises criterion which has been formulated previously shows a reasonable agreement with experimental data on biaxial loaded specimen. The behavior of concrete loaded in a tri-axial stress state is, however, different from the behavior in biaxial stress states and is dominated by two mechanisms, firstly the behavior is pressure-sensitive in compression and secondly, the behavior is dilatant. This cannot be modeled with the composite yield criterion which has been discussed in the previous paragraph.

In order to remedy these deficiencies, an axisymmetrical formulation of a composite yield contour will be proposed which is defined by the Rankine yield criterion which bounds the in-plane tensile stresses and a non-associative Drucker-Prager yield criterion which is applicable in the compressive region. The tensile stress in the axisymmetrical direction will be bounded by a tension-cut-off criterion. The composite yield criterion is then given by

$$\left\{ \begin{array}{l} f_1 = (1/2 \xi^T P_1 \xi)^{1/2} + 1/2 \pi_1^T \xi - \bar{\sigma}_1(\gamma \kappa_T) \\ f_2 = (1/2 \sigma^T P_2 \sigma)^{1/2} + \alpha_f \pi_2^T \sigma - \bar{\sigma}_2(\kappa_C) \\ f_3 = \pi_3^T \sigma - \bar{\sigma}_3(\kappa_3) \end{array} \right. \quad (A.1)$$

with again a mixed hardening rule for the Rankine criterion and an isotropic hardening rule for the Drucker-Prager criterion. The equivalent stress $\bar{\sigma}_1$ is the uniaxial tensile strength as a function of the internal parameter κ_T . The equivalent stress $\bar{\sigma}_3$ is also the uniaxial tensile strength, but now as a function of the internal parameter κ_3 which allows for a different hardening behavior in-plane and in the axisymmetrical direction. Finally, the equivalent stress $\bar{\sigma}_2$ is determined by the material properties, the cohesion c and the angle of internal friction ϕ , according to

$$\bar{\sigma}_2(\kappa_2) = c(\kappa_C) \frac{6 \cos \varphi}{3 - \sin \varphi}$$

in which only the possibility of cohesion hardening is considered. The factor α_f is given by

$$\alpha_f = \frac{2 \sin \varphi}{3 - \sin \varphi}$$

The projection vectors are given by

$$\begin{aligned} \pi_1 &= \{ 1, 1, 0, 0 \}^T \\ \pi_2 &= \{ 1, 1, 1, 0 \}^T \\ \pi_3 &= \{ 0, 0, 1, 0 \}^T \end{aligned} \quad (\text{A.2})$$

respectively.

The inelastic strain rate is again determined by Koiter's rule, Koiter (1953), which allows for a summation of the inelastic strain of each yield function according to

$$\dot{\epsilon}_c = \dot{\epsilon}_{c,1} + \dot{\epsilon}_{c,2} + \dot{\epsilon}_{c,3} = \dot{\lambda}_1 \partial_\sigma f_1 + \dot{\lambda}_2 \partial_\sigma g_2 + \dot{\lambda}_3 \partial_\sigma f_3 \quad (\text{A.3})$$

in which the plastic potential function for the Drucker-Prager yield criterion g_2 is given by

$$g_2 = (1/2 \sigma^T P_2 \sigma)^{1/2} + \alpha_g \pi_2^T \sigma - \bar{\sigma}_2(\kappa_C) \quad (\text{A.4})$$

The plastic potential function differs from the yield function as the factor α_f , which is a function of the angle of internal friction φ , is replaced by a factor α_g which is now a function of the dilatancy angle ψ , according to

$$\alpha_g = \frac{2 \sin \psi}{3 - \sin \psi}$$

The damage in the material is now reflected in three internal parameters, one for damage in in-plane tension, κ_T , one for the damage in compression, κ_C , and one for tensile damage in the axisymmetrical direction κ_3 . For a work-hardening hypothesis, the internal parameters are determined by the inelastic work rate for the three respective yield functions, i.e.

$$\begin{cases} \dot{W}_{c,1} = \xi^T \dot{\epsilon}_{c,1} + \zeta_{12} \frac{\bar{\sigma}_1}{\bar{\sigma}_2} \sigma^T \dot{\epsilon}_{c,2} + \zeta_{13} \frac{\bar{\sigma}_1}{\bar{\sigma}_3} \sigma^T \dot{\epsilon}_{c,3} = \bar{\sigma}_1(\gamma \kappa_T) \dot{\kappa}_T \\ \dot{W}_{c,2} = \sigma^T \dot{\epsilon}_{c,2} + \zeta_{21} \frac{\bar{\sigma}_2}{\bar{\sigma}_1} \xi^T \dot{\epsilon}_{c,1} + \zeta_{23} \frac{\bar{\sigma}_2}{\bar{\sigma}_3} \sigma^T \dot{\epsilon}_{c,3} = \bar{\sigma}_2(\kappa_C) \dot{\kappa}_C \\ \dot{W}_{c,3} = \sigma^T \dot{\epsilon}_{c,3} + \zeta_{31} \frac{\bar{\sigma}_3}{\bar{\sigma}_1} \xi^T \dot{\epsilon}_{c,1} + \zeta_{32} \frac{\bar{\sigma}_3}{\bar{\sigma}_2} \sigma^T \dot{\epsilon}_{c,2} = \bar{\sigma}_3(\kappa_3) \dot{\kappa}_3 \end{cases} \quad (A.5)$$

with scalars ζ_{12} , ζ_{13} , ζ_{21} , ζ_{23} , ζ_{31} and ζ_{32} which represent the coupling of the damage in the material. With the application of Euler's theorem the eqs.(A.1)-(A.5) result in the following expression for the evolution of the internal parameters

$$\begin{cases} \dot{\kappa}_T = \dot{\lambda}_1 + \zeta_{12} \dot{\lambda}_2 + \zeta_{13} \dot{\lambda}_3 \\ \dot{\kappa}_C = \zeta_{21} \dot{\lambda}_1 + \dot{\lambda}_2 + \zeta_{23} \dot{\lambda}_3 \\ \dot{\kappa}_3 = \zeta_{31} \dot{\lambda}_1 + \zeta_{32} \dot{\lambda}_2 + \dot{\lambda}_3 \end{cases} \quad (A.6)$$

With

$$\dot{q} = \begin{Bmatrix} \dot{\kappa}_T \\ \dot{\kappa}_C \\ \dot{\kappa}_3 \end{Bmatrix} \quad h_1 = \begin{Bmatrix} 1 \\ \zeta_{21} \\ \zeta_{31} \end{Bmatrix} \quad h_2 = \begin{Bmatrix} \zeta_{12} \\ 1 \\ \zeta_{32} \end{Bmatrix} \quad h_3 = \begin{Bmatrix} \zeta_{13} \\ \zeta_{23} \\ 1 \end{Bmatrix} \quad (A.7)$$

eq.(A.6) can formally be expressed as

$$\dot{q} = \dot{\lambda}_1 h_1 + \dot{\lambda}_2 h_2 + \dot{\lambda}_3 h_3 \quad (A.8)$$

Because the hardening functions are given by a scalar expression, the incremental internal parameter vector is determined by

$$\Delta q^{(i+1)} = \Delta \lambda_1^{(i+1)} h_1 + \Delta \lambda_2^{(i+1)} h_2 + \Delta \lambda_3^{(i+1)} h_3 \quad (A.9)$$

for a coupled system of three yield surfaces.

The return-mapping procedure described in the previous paragraph is now extended and reads

$$\begin{cases} \sigma^{(i+1)} = \sigma_E - \Delta \lambda_1^{(i+1)} D_e \partial_{\sigma} f_1^{(i+1)} - \Delta \lambda_2^{(i+1)} D_e \partial_{\sigma} g_2^{(i+1)} - \Delta \lambda_3^{(i+1)} D_e \partial_{\sigma} f_3^{(i+1)} \\ \eta^{(i+1)} = \eta_E + \Delta \lambda_1^{(i+1)} (1 - \gamma) E_{ks} \partial_{\sigma} g_1^{(i+1)} \end{cases} \quad (A.10)$$

and the updated stress and updated back stress are again given by the solution of the

following system of equations

$$\begin{Bmatrix} \sigma^{(i+1)} \\ \eta^{(i+1)} \end{Bmatrix} = \begin{bmatrix} A_{11} & A_{12} \\ A_{21} & A_{22} \end{bmatrix}^{-1} \begin{Bmatrix} \sigma_E - 1/2 \Delta \lambda_1^{(i+1)} D_e \pi_1 - \alpha_g \Delta \lambda_2^{(i+1)} D_e \pi_2 - \Delta \lambda_3^{(i+1)} D_e \pi_3 \\ \eta_E + 1/2 \Delta \lambda_1^{(i+1)} (1 - \gamma) E_{ks} \pi_1 \end{Bmatrix}$$

with the matrices A_{ij} again given by

$$A_{11} = I + \frac{\Delta \lambda_1^{(i+1)}}{2\Psi_1} D_e P_1 + \frac{\Delta \lambda_2^{(i+1)}}{2\Psi_2} D_e P_2$$

$$A_{12} = -\frac{\Delta \lambda_1^{(i+1)}}{2\Psi_1} D_e P_1$$

$$A_{21} = -\frac{\Delta \lambda_1^{(i+1)}}{2\Psi_1} (1 - \gamma) E_{ks} \Lambda_M P_1$$

$$A_{22} = I + \frac{\Delta \lambda_1^{(i+1)}}{2\Psi_1} (1 - \gamma) E_{ks} \Lambda_M P_1$$

The denominators Ψ_1 and Ψ_2 are now given by

$$\begin{cases} \Psi_1 = \bar{\sigma}_1(\gamma \kappa_T) - 1/2 \pi_1^T (\sigma^{(i+1)} - \eta^{(i+1)}) \\ \Psi_2 = \bar{\sigma}_2(\kappa_C) - \alpha_f \pi_2^T \sigma^{(i+1)} \end{cases} \quad (A.11)$$

which is again not very convenient because the updated stress cannot be related linearly to the trial state. To arrive at a more suitable form we first multiply $\sigma^{(i+1)}$ with the vector π_2^T so that

$$\begin{aligned} \pi_2^T \sigma^{(i+1)} &= \pi_2^T \sigma_E - 1/2 \Delta \lambda_1^{(i+1)} \pi_2^T D_e \pi_1 \\ &\quad - \alpha_g \Delta \lambda_2^{(i+1)} \pi_2^T D_e \pi_2 \\ &\quad - \Delta \lambda_3^{(i+1)} \pi_2^T D_e \pi_3 \end{aligned} \quad (A.12)$$

because $\pi_2^T D_e P_1 = 0^T$ and $\pi_2^T D_e P_2 = 0^T$. The denominator Ψ_2 can now be expressed solely in terms of the trial state variables and the inelastic multipliers

$$\Psi_2 = \bar{\sigma}_2(\kappa_C) - \alpha_f \pi_2^T \sigma_E + \alpha_f \left(\frac{\Delta\lambda_1 E}{(1-2\nu)} + \frac{3 \alpha_g \Delta\lambda_2 E}{(1-2\nu)} + \frac{\Delta\lambda_3 E}{(1-2\nu)} \right) \quad (\text{A.13})$$

In order to calculate Ψ_1 , we multiply both $\sigma^{(i+1)}$ and $\eta^{(i+1)}$ with π_1^T which results in

$$\left\{ \begin{array}{l} \pi_1^T \sigma^{(i+1)} = \pi_1^T \sigma_E - 1/2 \Delta\lambda_1^{(i+1)} \pi_1^T D_e \pi_1 \\ \quad - \frac{\Delta\lambda_2^{(i+1)}}{2\Psi_2} \pi_1^T D_e P_2 \sigma^{(i+1)} - \alpha_g \Delta\lambda_2^{(i+1)} \pi_1^T D_e \pi_2 \\ \quad - \Delta\lambda_3^{(i+1)} \pi_1^T D_e \pi_3 \\ \pi_1^T \eta^{(i+1)} = \pi_1^T \eta_E - 1/2 \Delta\lambda_1^{(i+1)} (1-\gamma) \pi_1^T E_{ks} \pi_1 \end{array} \right. \quad (\text{A.14})$$

The factor $\pi_1^T \sigma$ is still a function of the final stress because $\pi_1^T D_e P_2 = 2 G \{ 1, 1, -2, 0 \} \neq 0^T$. Substitution of this relation into eq.(A.14) results in

$$\begin{aligned} \pi_1^T \sigma^{(i+1)} &= \pi_1^T \sigma_E - 1/2 \Delta\lambda_1^{(i+1)} \pi_1^T D_e \pi_1 - \alpha_g \Delta\lambda_2^{(i+1)} \pi_1^T D_e \pi_2 - \Delta\lambda_3^{(i+1)} \pi_1^T D_e \pi_3 \\ &\quad - \frac{\Delta\lambda_2^{(i+1)} G}{\Psi_2} \pi_1^T \sigma^{(i+1)} + \frac{2 \Delta\lambda_2^{(i+1)} G}{\Psi_2} \sigma_{zz}^{(i+1)} \end{aligned} \quad (\text{A.15})$$

The return-mapping of the stress in the z -direction is given by (cf. eq.(A.10)),

$$\begin{aligned} \sigma_{zz}^{(i+1)} &= \sigma_{zz,E} - \frac{\Delta\lambda_1^{(i+1)} \nu E}{(1+\nu)(1-2\nu)} - \frac{\alpha_g \Delta\lambda_2^{(i+1)} E}{(1-2\nu)} - \frac{\Delta\lambda_3^{(i+1)} (1-\nu) E}{(1+\nu)(1-2\nu)} \\ &\quad + \frac{\Delta\lambda_2^{(i+1)} G}{\Psi_2} \pi_1^T \sigma^{(i+1)} - \frac{2 \Delta\lambda_2^{(i+1)} G}{\Psi_2} \sigma_{zz}^{(i+1)} \end{aligned} \quad (\text{A.16})$$

The factor $\pi_1^T \sigma^{(i+1)}$ is finally obtained by substituting eq.(A.16) into eq.(A.15) which results in

$$\begin{aligned}
\pi_1^T \sigma^{(i+1)} &= \frac{\Psi_2 + 2 \Delta\lambda_2^{(i+1)} G}{\Psi_2 + 3 \Delta\lambda_2^{(i+1)} G} \left(\pi_1^T \sigma_E - \frac{\Delta\lambda_1^{(i+1)} E}{(1+\nu)(1-2\nu)} - \frac{2 \alpha_g \Delta\lambda_2^{(i+1)} E}{(1-2\nu)} - \frac{2 \Delta\lambda_3^{(i+1)} \nu E}{(1+\nu)(1-2\nu)} \right) \\
&+ \frac{2 \Delta\lambda_2^{(i+1)} G}{\Psi_2 + 3 \Delta\lambda_2^{(i+1)} G} \left(\sigma_{zz,E} - \frac{\Delta\lambda_1^{(i+1)} \nu E}{(1+\nu)(1-2\nu)} - \frac{\alpha_g \Delta\lambda_2^{(i+1)} E}{(1-2\nu)} - \frac{\Delta\lambda_3^{(i+1)} (1-\nu)E}{(1+\nu)(1-2\nu)} \right)
\end{aligned} \tag{A.17}$$

With this result the denominators are solely expressed in terms of the trial state variables and the inelastic multipliers.

Because the mapping matrix is equal to the return-mapping matrix given in the previous paragraph, the spectral decomposition discussed there can be applied without further modifications.

Upon substitution of $\sigma^{(i+1)}$ and $\eta^{(i+1)}$ as given in eq.(A.10), we observe that the yield functions are now solely expressed in terms of the inelastic multipliers $\Delta\lambda_1$, $\Delta\lambda_2$ and $\Delta\lambda_3$. The constraint equations

$$\begin{cases} c_1 f_1(\Delta\lambda_1^{(i+1)}, \Delta\lambda_2^{(i+1)}, \Delta\lambda_3^{(i+1)}) = 0 \\ c_2 f_2(\Delta\lambda_1^{(i+1)}, \Delta\lambda_2^{(i+1)}, \Delta\lambda_3^{(i+1)}) = 0 \\ c_3 f_3(\Delta\lambda_1^{(i+1)}, \Delta\lambda_2^{(i+1)}, \Delta\lambda_3^{(i+1)}) = 0 \end{cases} \tag{A.18}$$

have to be solved to obtain the final stress state. This is again done using a local Newton-Raphson iteration with a Broyden update of the Jacobian. The scalars c_1 , c_2 and c_3 are equal to one when the corresponding yield function is active, else the scalars are equal to zero. The initial Jacobian is determined from the linearization of the yield functions in the trial state

$$\begin{cases} f_1^{(i+1)} = f_1(\sigma_E - \sum_{j=1}^3 \Delta\lambda_j^{(0)} D_e \partial_\sigma f_j, \eta_E + \Delta\eta, \kappa_{T,E} + \Delta\kappa_T) \\ f_2^{(i+1)} = f_2(\sigma_E - \sum_{j=1}^3 \Delta\lambda_j^{(0)} D_e \partial_\sigma f_j, \kappa_{C,E} + \Delta\kappa_C) \\ f_3^{(i+1)} = f_3(\sigma_E - \sum_{j=1}^3 \Delta\lambda_j^{(0)} D_e \partial_\sigma f_j, \kappa_{3,E} + \Delta\kappa_3) \end{cases} \tag{A.19}$$

which results in the following system of equations

$$J^{(0)} s_0 = -f(x_0) \tag{A.20}$$

with the initial Jacobian given by

$$J_{ij}^{(0)} = -\partial_{\sigma} f_i^T \mathbf{D}_e \partial_{\sigma} f_j + \partial_q f_i^T \mathbf{h}_j \quad (\text{A.21})$$

except for $J_{11}^{(0)}$ which is given by

$$J_{11}^{(0)} = -\partial_{\sigma} f_1^T \mathbf{D}_e \partial_{\sigma} f_1 - (1 - \gamma) E_k + \partial_q f_1^T \mathbf{h}_1 \quad (\text{A.22})$$

The vectors $\mathbf{s}^{(0)}$ and $\mathbf{f}^{(0)}$ are given by

$$\mathbf{s}^{(0)} = \{ \Delta \lambda_1^{(0)}, \Delta \lambda_2^{(0)}, \Delta \lambda_3^{(0)} \}^T \quad (\text{A.23})$$

$$\mathbf{f}^{(0)} = \{ c_1 f_1(\boldsymbol{\sigma}_E, \boldsymbol{\eta}_E, \kappa_{T,E}), c_2 f_2(\boldsymbol{\sigma}_E, \kappa_{C,E}), c_3 f_3(\boldsymbol{\sigma}_E, \kappa_{3,E}) \}^T$$

Initially the constraints are determined by the violation of the yield criterion in the trial state, i.e.

$$\begin{cases} c_1 = 1 & \text{if } f_1(\boldsymbol{\sigma}_E, \boldsymbol{\eta}_E, \kappa_{T,E}) > 0 \\ c_2 = 1 & \text{if } f_2(\boldsymbol{\sigma}_E, \kappa_{C,E}) > 0 \\ c_3 = 1 & \text{if } f_3(\boldsymbol{\sigma}_E, \kappa_{3,E}) > 0 \end{cases}$$

During the return-mapping the active yield functions are determined with conditions

$$c_j = 1 \quad \text{if } \Delta \lambda_j^{(i+1)} > 0 \quad \text{else} \quad c_j = 0$$

The consistent tangent stiffness matrix for the Newton-Raphson iteration is again most conveniently derived from the updated stress at time $(i + 1)$

$$\boldsymbol{\sigma}^{(i+1)} = \mathbf{D}_e [\boldsymbol{\varepsilon}^{(i+1)} - {}^t \boldsymbol{\varepsilon}_c - \Delta \lambda_1^{(i+1)} \partial_{\sigma} f_1 - \Delta \lambda_2^{(i+1)} \partial_{\sigma} g_2 - \Delta \lambda_3^{(i+1)} \partial_{\sigma} f_3]$$

The total derivative then reads

$$\begin{aligned} d\boldsymbol{\sigma}^{(i+1)} = \mathbf{D}_e [d\boldsymbol{\varepsilon}^{(i+1)} - d\lambda_1 \partial_{\sigma} f_1 - \Delta \lambda_1^{(i+1)} \partial_{\sigma\sigma}^2 f_1 d\boldsymbol{\sigma}^{(i+1)} \\ - d\lambda_2 \partial_{\sigma} g_2 - \Delta \lambda_2^{(i+1)} \partial_{\sigma\sigma}^2 g_2 d\boldsymbol{\sigma}^{(i+1)} \\ - d\lambda_3 \partial_{\sigma} f_3] \end{aligned} \quad (\text{A.24})$$

which is written as

$$d\boldsymbol{\sigma}^{(i+1)} = \mathbf{H} [d\boldsymbol{\varepsilon}^{(i+1)} - d\lambda_1 \partial_{\sigma} f_1 - d\lambda_2 \partial_{\sigma} g_2 - d\lambda_3 \partial_{\sigma} f_3] \quad (\text{A.25})$$

with the modified stiffness matrix \mathbf{H} again given by

$$\mathbf{H} = [\mathbf{C}_e + \Delta\lambda_1^{(i+1)} \partial_{\sigma\sigma}^2 f_1 + \Delta\lambda_2^{(i+1)} \partial_{\sigma\sigma}^2 g_2]^{-1}$$

where it is noted that $\partial_{\sigma\sigma}^2 g_2 = \partial_{\sigma\sigma}^2 f_2$. Applying the generalized directional matrix \mathbf{U} , see Riggs and Powel (1990), eq.(A.25) is formally written as

$$d\boldsymbol{\sigma}^{(i+1)} = \mathbf{H} [d\boldsymbol{\epsilon}^{(i+1)} - \mathbf{U} d\boldsymbol{\lambda}] \quad (\text{A.26})$$

in which the matrix \mathbf{U} is given by

$$\mathbf{U} = \begin{bmatrix} c_1 \partial_{\sigma} f_1, c_2 \partial_{\sigma} g_2, c_3 \partial_{\sigma} f_3 \end{bmatrix} \quad (\text{A.27})$$

The plastic multipliers are collected in the vector $d\boldsymbol{\lambda} = \{ d\lambda_1, d\lambda_2, d\lambda_3 \}^T$. The consistency conditions determined by the active yield surfaces, give the relations for the inelastic multipliers

$$c_1 (\partial_{\sigma} f_1^T d\boldsymbol{\sigma} + \partial_{\eta} f_1^T d\boldsymbol{\eta} + \partial_q f_1^T d\mathbf{q}) + (1 - c_1) d\lambda_1 = 0 \quad (\text{A.28})$$

$$c_2 (\partial_{\sigma} f_2^T d\boldsymbol{\sigma} + \partial_q f_2^T d\mathbf{q}) + (1 - c_2) d\lambda_2 = 0 \quad (\text{A.29})$$

$$c_3 (\partial_{\sigma} f_3^T d\boldsymbol{\sigma} + \partial_q f_3^T d\mathbf{q}) + (1 - c_3) d\lambda_3 = 0 \quad (\text{A.30})$$

If the relations

$$d\mathbf{q} = c_1 \mathbf{h}_1 d\lambda_1 + c_2 \mathbf{h}_2 d\lambda_2 + c_3 \mathbf{h}_3 d\lambda_3$$

and

$$d\boldsymbol{\eta} = c_1 d\lambda_1 (1 - \gamma) E_k \partial_{\sigma} g_1$$

are substituted, the consistency conditions result in the following system of equations

$$d\boldsymbol{\lambda} = \mathbf{E}^{-1} \mathbf{V}^T d\boldsymbol{\sigma} \quad (\text{A.31})$$

with

$$\mathbf{E} = \begin{bmatrix} -c_1 \partial_q f_1^T \mathbf{h}_1 + c_1 (1 - \gamma) E_k + (1 - c_1) & -c_1 c_2 \partial_q f_1^T \mathbf{h}_2 & -c_1 c_3 \partial_q f_1^T \mathbf{h}_3 \\ -c_1 c_2 \partial_q f_2^T \mathbf{h}_1 & -c_2 \partial_q f_2^T \mathbf{h}_2 + (1 - c_2) & -c_2 c_3 \partial_q f_2^T \mathbf{h}_3 \\ -c_1 c_3 \partial_q f_3^T \mathbf{h}_1 & -c_2 c_3 \partial_q f_3^T \mathbf{h}_2 & -c_3 \partial_q f_3^T \mathbf{h}_3 + (1 - c_3) \end{bmatrix}$$

and

$$\mathbf{V}^T = \begin{bmatrix} c_1 \partial_{\sigma} f_1^T \\ c_2 \partial_{\sigma} f_2^T \\ c_3 \partial_{\sigma} f_3^T \end{bmatrix}$$

Substituting eq.(A.31) into eq.(A.26) results in

$$\left[\mathbf{H}^{-1} + \mathbf{U} \mathbf{E}^{-1} \mathbf{V}^T \right] d\boldsymbol{\sigma}^{(i+1)} = d\boldsymbol{\varepsilon}^{(i+1)} \quad (\text{A.32})$$

The consistent tangent stiffness matrix can now be calculated with the application of the Sherman-Morrison-Woodbury formula, which results in

$$d\boldsymbol{\sigma}^{(i+1)} = \left[\mathbf{H} - \mathbf{H} \mathbf{U} (\mathbf{E} + \mathbf{V}^T \mathbf{H} \mathbf{U})^{-1} \mathbf{V}^T \mathbf{H} \right] d\boldsymbol{\varepsilon}^{(i+1)} \quad (\text{A.33})$$

Again it is noted that if the yield function are coupled through the hardening functions given in eq.(A.7), the tangent stiffness matrix is in general nonsymmetric.

The corners in the composite yield surface in a axisymmetrical situation require also special attention since they may cause numerical difficulties. Now also two possible situations are possible, firstly the situation where $\Psi_1 = 0$ and secondly the situation where $\Psi_2 = 0$. Both situations have been treated in the previous paragraph and do not need any further discussion.

5. APPLICATION TO PLAIN CONCRETE

The objective of this Chapter is to compare the incremental formulation of the fracture energy-based plasticity model and the rotating crack model in applications to plain concrete structures. It will be shown that the fracture energy-based plasticity model is well capable to simulate crack propagation in plain concrete. The results will be presented with a load-displacement diagram of a representative degree-of-freedom and the pattern of active cracks, which are defined as the cracks at the integration points in which the internal parameter κ is equal or greater than half κ_a . If it is necessary to assess the behavior of structure, the total displacement will also be given.

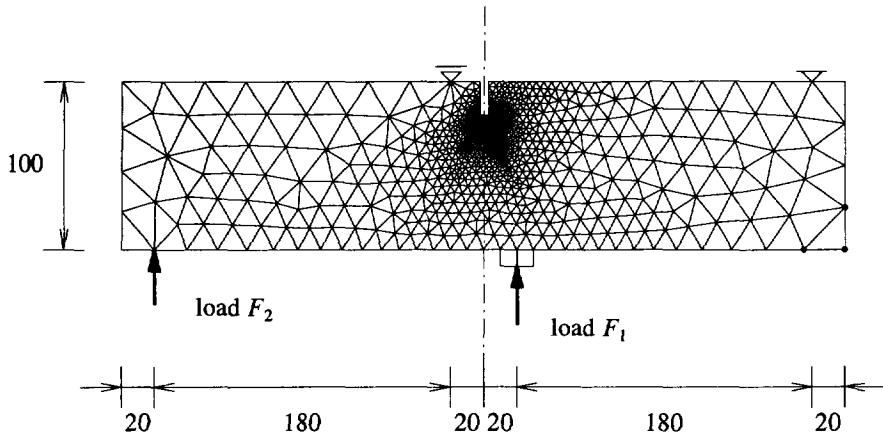


Figure 5.1 Single-edge-notched beam. Finite element mesh. Measures in [mm].

5.1 Single-edge-notched beam

The single-edge-notched geometry of the Iosipescu beam has been used in experiments on concrete beams for the first time by Arrea and Ingraffea (1982). The experiments show a curved crack propagating from the tip of the notched to the opposite side of the loading platen. The experiments on the SEN-specimen have been simulated extensively during the last decade, see De Borst (1986), Rots (1988), Rots (1992), Schlangen (1993). RILEM committee 89-FMT has also proposed an experimental round robin using the SEN-specimen to study the mixed-mode fracture process. The proposed experimental set-up has been improved such that the experiments could be performed without friction in the roller bearings, see for more details Schlangen (1993). The scatter of the experimental results is small which makes the experiments very suitable for numerical simulation. The stress state in the specimen is mainly tension-shear with small compressive stresses. The objective of the analyses presented here is to simulate curved mode I fracture propagation with the rotating crack model and the fracture energy-based plasticity model with isotropic and kinematic hardening in an incremental formulation.

The SEN-specimen are $400 \times 100 \times 100$ [mm³] with a notch of 5×20 [mm²]. The distance between the inner supports is equal to 40 [mm] and the distance between the outer supports is equal to 400 [mm]. The specimen has been discretized with 1655 three-noded plane-stress elements with a single integration point and a very dense distribution of elements around the tip of the notch, see Figure 5.1. The distribution of the loads has been modeled as described by Schlangen (1993), with $F_1 = 10/11 F$ at the center loading platen and $F_2 = 1/11 F$ at the outer loading platen, with F the total load. Only the center loading platen has been modeled because only this platen has an

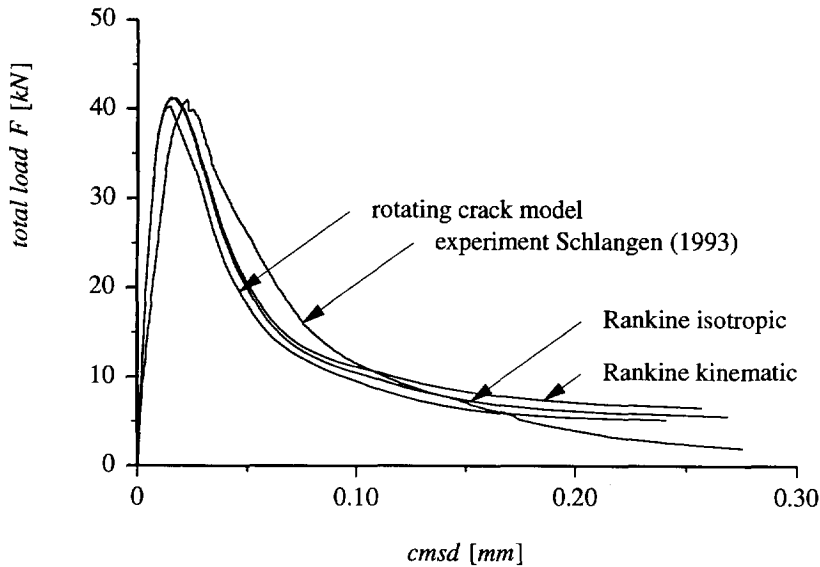


Figure 5.2 Single-edge-notched beam. Load-cmsd diagram.

Table 5.1 Material properties single-edge-notched beam.

	concrete	
f_{cm}	36.5	$[N/mm^2]$
E_c	35000	$[N/mm^2]$
ν	0.15	$[-]$
$f_{ct,m}$	2.8	$[N/mm^2]$
G_f	0.07 ¹⁾	$[Nmm/mm^2]$

1) exponential softening

influence on the stress distribution. The middle support has been fixed in the vertical direction and the outer support has been fixed in vertical and horizontal directions. The experiments on the small beams with normal weight concrete, maximum aggregate 8 [mm], have been chosen for the numerical simulation, with the material properties given in Table 5.1. The analyses have been performed using the solution technique which has been discussed in Chapter 2. The convergence characteristics of the calculations are good, although for the rotating crack model a number of line searches were necessary. The comparison of the experimental result and the numerical simulations focuses on the crack-mouth-sliding-displacement (cmsd) versus the total load which should be considered as a representative measure of the nonlinear behavior of the structure. The total load-cmsd diagram, Figure 5.2, shows a pre-peak behavior



Figure 5.3 Single-edge-notched beam. Active cracks at final load.

which is a little too stiff for all models and a failure load which is in accordance with the experimental result. The post-peak behavior is simulated within acceptable boundaries for all models. It appears that the different formulations of the constitutive models do not differ very much. Neither of the models is capable to predict a genuine separation with a full softening behavior which has been found in the experiment. An analysis with a discrete crack model, Rots (1988), of a similar beam shows a full softening behavior, but the analyses with other smeared crack models show the same tendency. At peak load the crack has been initiated at the right-hand-side of the notch with a direction of approximately 45° which has also been observed in the experiments, Schlangen (1993). At the final load the crack is propagated through the specimen from the notch to the right-hand-side of the loading platen which is shown in Figure 5.3 for the analysis with the Rankine model with isotropic hardening. The crack pattern of the analysis with kinematic hardening or the rotating crack model is almost equal to the crack pattern of the Rankine model with isotropic hardening. The differences between the models is small and only perceptible in the final load stage.

5.2 Pull-out of an anchor bolt

The pull-out analysis of an anchor bolt has been proposed by RILEM-committee TC90-FMA as a round-robin analysis in order to compare the different analytical and numerical methods. The geometry and material properties of the first proposal for the round-robin, Elfgren (1990), have been used to simulate the pull-out with the standard smeared crack models for both the plane-stress and the axisymmetrical case, Feenstra, Rots and De Borst (1990). The second, revised invitation also concerned the experimental analysis of the proposed geometry for both the plane-stress and axisymmetrical case with an embedded depth of 50, 150 and 450 [mm] respectively. In the Stevin Laboratory at Delft University of Technology experiments have been carried out on a plane-stress specimen with an embedded depth of 100 [mm], Vervuurt, Schlangen and Van Mier (1993). These experiments have been used in this study to investigate the behavior of the fracture energy-based plasticity model and the rotating crack model.

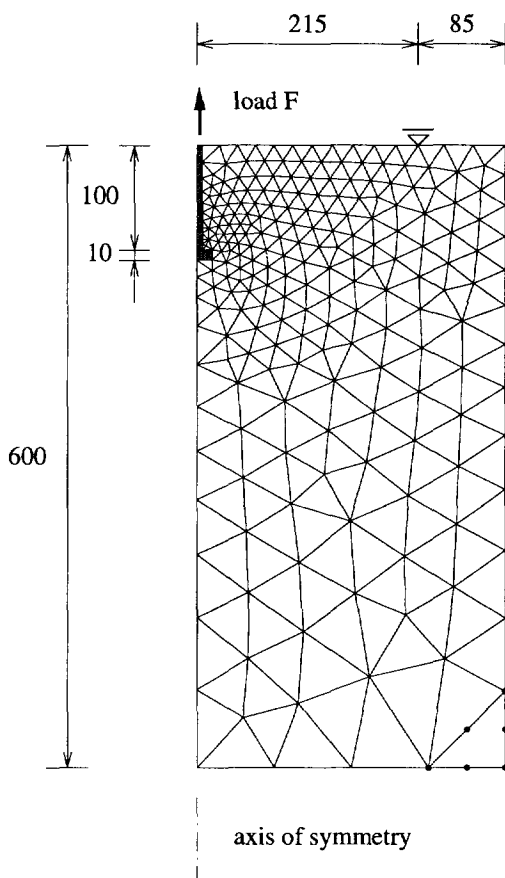


Figure 5.4 Pull-out of an anchor bolt. Finite element model. Measures in [mm].

Table 5.2 Material properties pull-out of an anchor bolt.

concrete		
f_{cm}	35.0	[N/mm ²]
E_c	37000	[N/mm ²]
ν	0.15	[-]
$f_{ct,m}$	2.5	[N/mm ²]
G_f	0.09 ¹⁾	[Nmm/mm ²]
G_c	5.0 ²⁾	[Nmm/mm ²]

1) exponential softening

2) parabolic softening

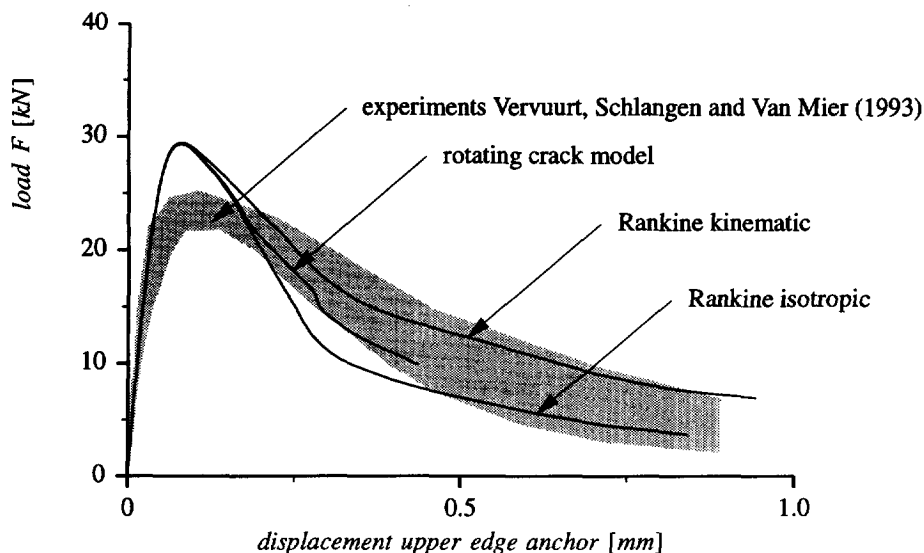


Figure 5.5 Pull-out of an anchor bolt. Load - displacement diagram.

The finite element discretization is given in Figure 5.4. Only the half of the specimen has been discretized with 402 six-noded plane-stress triangles with a seven-point integration. The anchor has been modeled using 13 four-noded plane-stress elements with a four-point integration. The material properties are given in Table 5.2. The analyses have been performed under the proposed solution strategy. The sign of the initial load increment has been determined using two methods. In the pre-peak regime, the sign has been determined using the displacement-based method of Crisfield. After the failure load the sign has been determined using the pivot method. The latter method could not be used in the pre-peak regime because one negative pivot occurred at a load of approximately 25 [kN], which caused spurious unloading. A possible descending branch could not be found at this point.

The results are given as the load versus the displacement of the upper-outer edge of the anchor head and the crack pattern at different stages of the calculation. The load displacement diagram is given in Figure 5.5 for the different constitutive models. Analyses with the composite yield surface show that the influence of the compressive nonlinearity on the load-displacement curve is negligible and these diagrams are not shown in Figure 5.5. The predicted failure load is approximately 20 % too high when compared with the experimental results, but the post-peak behavior is predicted in agreement with the experimental response. It is remarkable that the failure load is almost equal for all constitutive models but that the post-peak behavior shows substantial differences. The Rankine model with kinematic hardening shows a more ductile response than the Rankine model with isotropic hardening. These differences cannot be explained by a different failure mode because the crack pattern is almost equal for all analyses.

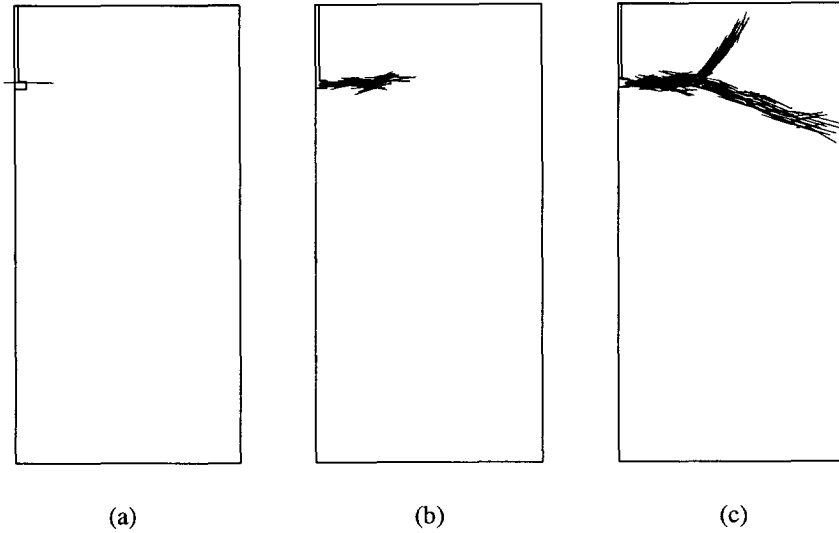


Figure 5.6 Pullout of an anchor bolt. Active cracks (a) just before maximum load ; (b) just after maximum load ; (c) final crack pattern

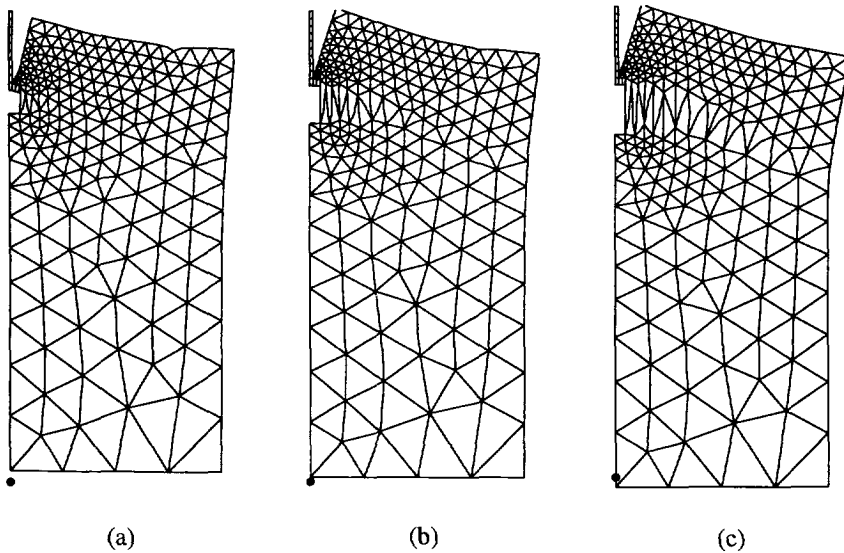


Figure 5.7 Pullout of an anchor bolt. Total displacements. (a) just before maximum load ; (b) just after maximum load ; (c) at final load.

The rotating crack model results in a load-displacement diagram which is between the other two curves. The calculations of the rotating crack model have been terminated at an early stage because convergence could no longer be achieved. The failure mode is a

sudden crack propagation which is clearly shown by the crack pattern of the Rankine model with isotropic hardening which is shown in Figure 5.6. Just before the maximum load the cracks localize in a small region around the anchor head and after the maximum load the crack propagates horizontally through the specimen which is accompanied with a decreasing load. When the crack has grown towards the support it branches into two cracks, one propagating in the direction of the support, and one propagating downwards. This crack branching has also been observed in the experiments where it is even more pronounced because the crack pattern in the specimen is nonsymmetric, see Vervuurt, Schlangen and Van Mier (1993). The crack propagating downwards is, however, the active crack which can be seen from the displacements plotted in Figure 5.7 for three different load stages. This analysis shows that the constitutive models which have been developed are capable to predict the failure load, the post-peak behavior and the failure mode accurate enough to be used in the analysis of a design problem which is formulated by RILEM-committee TC90-FMA as one of the goals.

5.3 Cylinder splitting test

The cylinder splitting test is often used as an indirect test for determining the tensile strength of concrete. However, the tensile strength which can be derived from this test is considerably influenced by the boundary conditions and failure is often induced by compressive softening under the loading platen, see Hannant, Buckley and Croft (1973). Although the stress state under the loading platen is considered to be triaxial, this example has been chosen to analyze the capability of the developed models to predict the failure mode in a tension-compression test. The geometry of the cylinder splitting test has been taken from a similar analysis of Saourides and Mazars (1989) who analyzed this example with a local and nonlocal damage model. Their conclusion was that it is not possible to obtain a splitting type of failure with a traditional local approach because damage localizes under the loading area. The fracture-energy based models which will be used in this study can provide a solution as will be shown in the following analysis.

The specimen which will be analyzed is a cylinder with a length of 160 [mm] and a cylinder radius of 40 [mm]. Only a quarter of the specimen is discretized because of symmetry conditions, with 105 six-noded plane-stress elements with a 7-point integration. The loading platen has been modeled with one 8-noded plane-stress element with a 9-point integration. The finite element discretization is shown in Figure 5.8 and the material properties which have been used are given in Table 5.3. The load versus the displacement of the loading platen is depicted in Figure 5.9 in which the influence of the compression softening is clearly shown. If no compression softening is modeled, the analysis does not show a limit load, but is monotonically increasing. The differences between the Rankine plasticity model with isotropic or kinematic hardening and the rotating crack model are negligible which is not surprising because the crack can be considered as a pure mode-I crack which does not rotate after cracking.

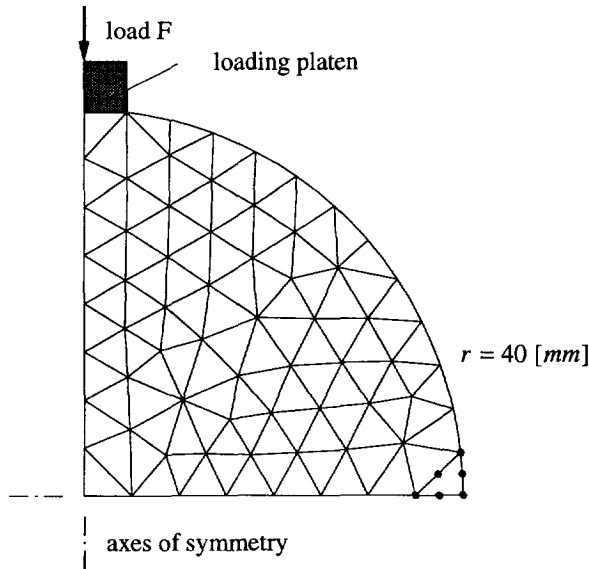


Figure 5.8 Cylinder splitting test. Finite element mesh.

Table 5.3 Material properties cylinder splitting test.

concrete		
f_{cm}	30.0	$[N/mm^2]$
E_c	37700	$[N/mm^2]$
ν	0.15	$[-]$
$f_{ct,m}$	3.0	$[N/mm^2]$
G_f	$0.10^{1)}$	$[Nmm/mm^2]$
G_c	$5.0^{2)}$	$[Nmm/mm^2]$

1) exponential softening

2) parabolic softening

If compression softening is taken into account the situation differs considerably. The ultimate load is smaller than the ultimate load of the composite yield function which is because of the different failure mechanism. The failure mechanism of the rotating crack model is completely governed by compression softening. On the other hand , a splitting crack is observed for the composite yield function and the biaxial stress state under the loading platen is clearly shown by the principal inelastic strain vectors which are plotted in Figure 5.10 at the maximum load and at the final state. At the maximum load the stress state under the loading platen is mainly mode-I compression with a starting splitting crack in the middle of the specimen. This crack propagates in the vertical direction

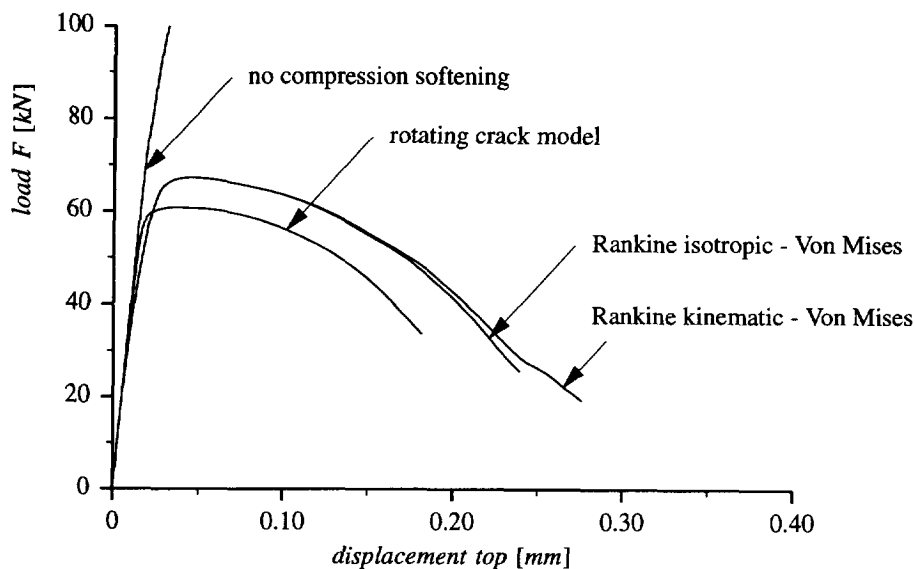


Figure 5.9 Cylinder splitting test. Load - displacement diagram.

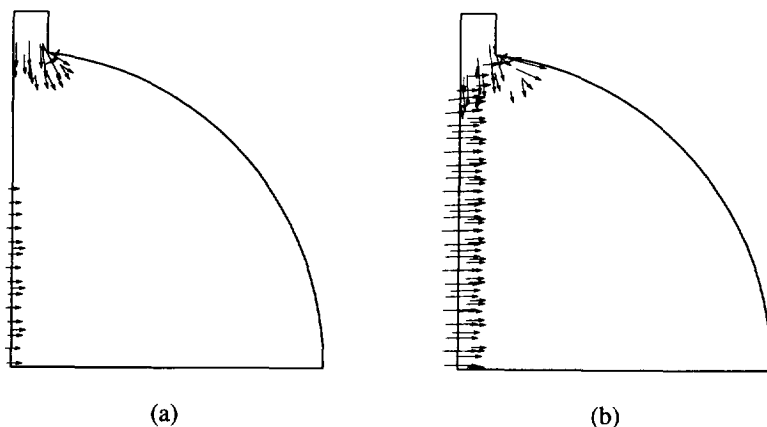


Figure 5.10 Cylinder splitting test. Principal plastic strain. (a) at maximum load ; (b) at final load.

what is attended with a descending load-displacement curve. The total displacements of the specimen, depicted in Figure 5.11, show clearly the crack in the middle of the specimen and the inelastic deformations under the loading platen. It is clear that the constitutive model which is used to analyze the cylinder splitting test is of utmost importance for the calculated response. If the nonlinear behavior due to compression softening is neglected, no limit load will be found, see also Labbane, Saha and Ting (1993).

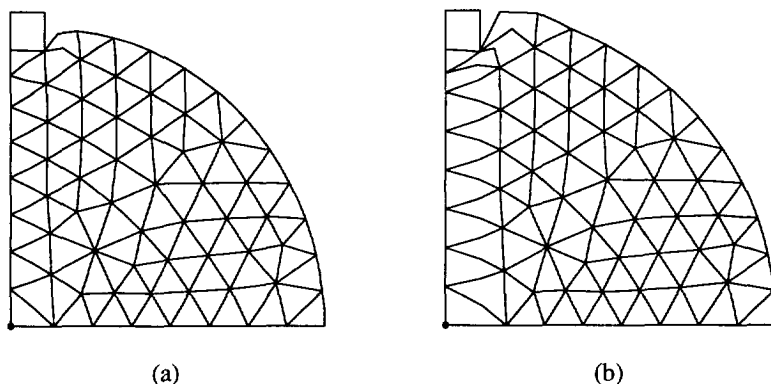


Figure 5.11 Cylinder splitting test. Total displacements. (a) at maximum load ; (b) at final load.

6. MODELING OF REINFORCED CONCRETE

The modeling of reinforcement in a finite element method is possible via three ways which have been used extensively during the last decades. A distributed representation of the reinforcement is probably the most frequently used method. In this approach the reinforcement is assumed to be distributed over the concrete element with a particular orientation angle. In slabs and shells, but also in panels, this method is implemented in a layered element where some layers represent the reinforcement and it is assumed that a state of plane-stress exists in each layer. An embedded formulation is often used in connection with iso-parametric elements, such that the displacements of the reinforcing bars or grids are the same as the displacement of the parent-element. Finally, a discrete representation of reinforcement is also possible. Uniaxial elements are superimposed to the elements representing the concrete with rigid connections or with interface elements. With the latter approach, bond slip between the concrete and the reinforcement can be modeled explicitly. With the two previous approaches it is generally assumed that perfect bond exists between concrete and reinforcement. In this study, an embedded formulation of reinforcement will be used with the assumption of perfect bond between concrete and reinforcement.

The reinforcement in concrete structures is usually applied in differently orientated layers of reinforcing grids. Because of the one-dimensional character of these grids, it is generally not necessary to introduce multiaxial constitutive models for the reinforcing steel, Chen (1982), and the experimental stress-strain curve for axial loading is idealized

as a uniaxial elasto-plastic constitutive model with work-hardening. The behavior in compression and tension is considered to be equal because buckling under compressive forces is prevented by the concrete cover.

In this Chapter, the embedded formulation of reinforcement will be discussed briefly and the constitutive model of reinforced concrete will be formulated and tested against some experimental data.

6.1 Embedded formulation

The numerically integrated, iso-parametric elements which are used to model the concrete structure are conveniently combined with an embedded formulation of the reinforcing elements. The reinforcing bars are considered to be uniaxial elements built into the iso-parametric parent-element, such that the displacements of the reinforcing bar are consistent with the displacements of the parent-element which implies the assumption of perfect bond between reinforcement and concrete.

The continuum incremental displacement vector $\Delta \mathbf{u}^e$ has been given by eq.(2.11)

$$\Delta \mathbf{u}^e = \mathbf{N}^e \Delta \mathbf{a}^e$$

with the superscript e to indicate the reference to the parent-element. The nodal incremental displacement vector with the nodal degrees-of-freedom of the parent-element is represented by the vector $\Delta \mathbf{a}^e$. The continuum incremental displacement vector for the reinforcement is now interpolated with the same interpolation matrix resulting in

$$\Delta \mathbf{u}^r = \mathbf{N}^e \Delta \mathbf{a}^e \quad (6.1)$$

with \mathbf{N}^e depending upon the iso-parametric coordinates of the integration points of the reinforcement. The incremental strain vector of the reinforcement is given by

$$\Delta \boldsymbol{\varepsilon}^r = \mathbf{B}^r \Delta \mathbf{a}^e \quad (6.2)$$

with the strain-discrete displacement matrix \mathbf{B}^r . This matrix has to be calculated with the iso-parametric coordinates of the integration points of the reinforcement which in general do not coincide with the integration points of the parent-element.

The constitutive relationship of the reinforcement is evaluated in the local coordinate system, i.e.

$$\sigma_{p,q} = \mathbf{D}(\boldsymbol{\varepsilon}_{p,q}) \boldsymbol{\varepsilon}_{p,q} \quad (6.3)$$

The incremental strain vector in the local coordinate system $\Delta \boldsymbol{\varepsilon}_{p,q}^r$ is calculated with the transformation of the strain vector $\Delta \boldsymbol{\varepsilon}^r$ in the element coordinate system. This transformation is given by

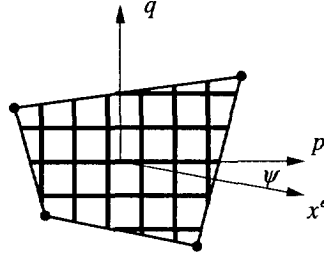


Figure 6.1 Element with embedded reinforcement in a plane-stress configuration

$$\Delta \epsilon'_{p,q} = T(\psi) \Delta \epsilon' \quad (6.4)$$

with ψ the angle between the local element coordinate system and the local reinforcement coordinate system, see Figure 6.1. The strain transformation matrix $T(\psi)$ in a plane-stress configuration is given by

$$T(\psi) = \begin{bmatrix} \cos^2 \psi & \sin^2 \psi & \sin \psi \cos \psi \\ \sin^2 \psi & \cos^2 \psi & -\sin \psi \cos \psi \\ -2 \sin \psi \cos \psi & 2 \sin \psi \cos \psi & \cos^2 \psi - \sin^2 \psi \end{bmatrix}$$

The internal force vector $f_r^{(i)}$ due to the stresses in the reinforcement is given by the relation

$$f_r^{(i)} = \int_{B'_0} (T(\psi) B^r)^T \sigma_{p,q}^{(i)} dV'_0 \quad (6.5)$$

and an additional term to the stiffness matrix, eq.(2.15)

$$K_r^{(i)} = \int_{B'_0} (T(\psi) B^r)^T D_{p,q}^{(i)} (T(\psi) B^r) dV'_0 \quad (6.6)$$

In conclusion, the embedded formulation of reinforcement results in the calculation of the element strain-nodal displacement matrix B^r for each integration point of the reinforcement, which is transformed to the reinforcement directions by a transformation matrix T as a function of the angle between the local element coordinate system and the local reinforcement coordinate system. This angle ψ is assumed to be constant because of the assumption of perfect bond which also implies that the direction of the reinforcement does not shift within the element.

6.2 Constitutive model of reinforced concrete

The behavior of reinforced concrete loaded in tension has been considered as the superposition of a material model for plain concrete, a material model for reinforcement and an additional stiffness which is referred to as the tension-stiffening component. The constitutive model for plain concrete, discussed in Chapter 4, has been derived as a fracture energy-based tension-softening model. The amount of fracture energy of a single crack has been assumed to be dissipated over an equivalent length which is related to the element size. In reinforced concrete usually a number of cracks develop during the process of loading until the cracking process stabilizes and no further cracks develop in the structure. The crack spacing at stabilized cracking is determined mainly by the amount of reinforcement. It is assumed in this study that the material model for plain concrete, based on fracture energy, can be applied to reinforced concrete with the total amount of fracture energy dissipated over the equivalent length. Because the fracture energy is assumed to be a material parameter, only the average crack spacing has to be determined.

The constitutive model of the reinforcement is assumed to be given by an elasto-plastic model with a linear-elastic stiffness matrix given by

$$D'_e = \begin{bmatrix} \rho_p E_s & 0 & 0 \\ 0 & \rho_q E_s & 0 \\ 0 & 0 & 0 \end{bmatrix} \quad (6.7)$$

in which ρ_p and ρ_q the reinforcement ratio in the p - and q -direction respectively and E_s the Young's modulus of the reinforcement. The shear stiffness of the reinforcing grid is assumed to be equal to zero.

In general, bond is assumed between reinforcement and concrete which is of fundamental importance for the constitutive model of reinforced concrete. Due to the bond action a series of cracks will develop in a reinforced member subjected to a tensile loading. The average crack spacing is in general a function of the amount and distribution of the reinforcement, concrete cover on the reinforcement and the tensile strength of the concrete. At a certain load stage the crack spacing will stabilize and a subsequent increase of the load no longer results in additional cracking. It is observed that also after stabilized cracking, the cracked reinforced concrete is still capable to carry stresses between two adjacent cracks which increases the overall stiffness of the structure. This phenomenon is called tension-stiffening and is related to the direction and properties of the reinforcement. In this study, the additional stiffness will be modeled with a constitutive model which describes the additional stiffness as a function of the strain in the direction of the reinforcement as discussed in Chapter 3 with a stiffness matrix given by

$$\mathbf{D}_{ia}^r = \begin{bmatrix} E_{b,p} & 0 & 0 \\ 0 & E_{b,q} & 0 \\ 0 & 0 & 0 \end{bmatrix} \quad (6.8)$$

in which $E_{b,p}$ and $E_{b,q}$ the bond stiffness in the p - and q -direction of the grid respectively. The constitutive model for tension-stiffening is in general a function of the reinforcement ratio, the diameter of the reinforcement and the average crack spacing.

The shear resistance of cracked reinforced concrete is determined by a combination of aggregate interlock, dowel action and the axial restraint stiffness of the reinforcement crossing a crack, see Walraven and Reinhardt (1981), Gambarova (1987), Vecchio and Nieto (1991). The resulting shear stress-shear strain response of aggregate interlock and dowel action shows a similar behavior, but in general it is assumed that aggregate interlock dominates over dowel action at small crack widths. The aggregate interlock models generally result in quite complex formulations even if the models are implemented in interface elements in which the constitutive relations are described in terms of crack opening and crack sliding, see e.g. Feenstra, de Borst and Rots (1991a, 1991b). Implementation in a smeared approach, in which average strains and stresses are considered, is not readily possible because a simple, mathematical model defined in terms of the strain vector is not available. It is therefore assumed that the shear stiffness of the interaction model is equal to zero.

As discussed in Chapter 3, the constitutive model of cracked reinforced concrete will be given by the superposition of the constitutive models of the plain concrete, the reinforcement and the interaction between concrete and reinforcement. In this manner, we have a phenomenological description of the material behavior of a composite material by describing the material models of the constituent materials and their mutual interaction in a separate manner.

6.3 Constitutive model for reinforcing steel

The material properties of reinforcing steel are well known in contrast to the material properties of concrete which are still a matter of debate. The reinforcing steel is usually classified on the basis of the geometrical properties, such as size and surface characteristics, and on the mechanical properties, such as characteristic yield stress and ductility, see CEB-FIP model code (1990). The material properties are defined on the basis of a standard tension test and the stress-strain diagram of the test is replaced by an idealized characteristic diagram according to Figure 6.2. The constitutive model of the reinforcement is assumed to be an elasto-plastic model with hardening. This idealized relation is equal in tension and compression with elastic unloading and reloading. The uniaxial elasto-plastic constitutive model can be derived from the multi-axial constitutive model described in Chapter 4. If an incremental formulation is used with a strain decomposition according to

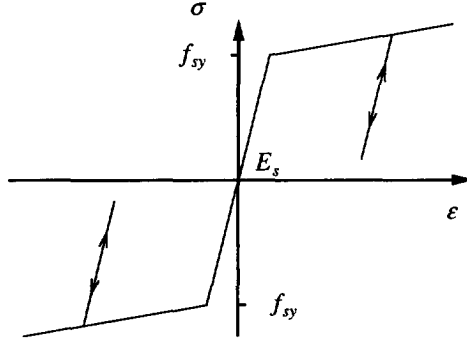


Figure 6.2 Uniaxial constitutive model of the reinforcement

$$\dot{\epsilon} = \dot{\epsilon}_e + \dot{\epsilon}_p \quad (6.9)$$

the stress rate in the reinforcement is given by

$$\dot{\sigma} = \rho_s E_s \dot{\epsilon}_e \quad (6.10)$$

with ρ_s the reinforcement ratio. The uniaxial formulation of the plasticity model is given by

$$f = [\sigma^2]^{1/2} - \bar{\sigma}(\kappa) \quad (6.11)$$

with the equivalent stress $\bar{\sigma}(\kappa)$ being the yield stress f_{sy} of the reinforcing steel as a function of the internal parameter κ . The evolution of the plastic strain is given by the associated flow rule

$$\dot{\epsilon}_p = \dot{\lambda} \partial_{\sigma} f = \frac{\dot{\lambda}}{\bar{\sigma}} \sigma \quad (6.12)$$

With the assumption of work hardening the evolution of the internal variable is given by

$$\dot{\kappa} = \dot{\lambda} \quad (6.13)$$

The return-mapping algorithm is now given by the scalar equation

$$\sigma^{(i+1)} = \left(\frac{\bar{\sigma}}{\bar{\sigma} + \Delta\lambda^{(i+1)} \rho_s E_s} \right) \sigma_E \quad (6.14)$$

which can be solved with a local Newton-Raphson procedure.

The consistent tangent stiffness matrix is derived from the updated stress

$$\sigma^{(i+1)} = E_s [\varepsilon^{(i+1)} - {}^t\varepsilon_p - \Delta\lambda^{(i+1)} \partial_\sigma f] \quad (6.15)$$

with the derivative given by

$$d\sigma^{(i+1)} = E_s [d\varepsilon^{(i+1)} - d\lambda \partial_\sigma f - \Delta\lambda^{(i+1)} \partial_{\sigma\sigma}^2 f d\sigma^{(i+1)}] \quad (6.16)$$

The consistency condition $df = \partial_\sigma f d\sigma + \partial_\kappa f d\kappa = 0$ then results in the relation

$$d\lambda = \frac{1}{E_p} \partial_\sigma f d\sigma \quad (6.17)$$

with the hardening parameter $E_p = \partial_\kappa \bar{\sigma}$. Because the second derivative of the yield function with respect to the stress is equal to zero, the consistent tangent stiffness matrix is identical to the continuum tangent stiffness matrix which reads

$$d\sigma^{(i+1)} = \left[E_s - \frac{E_s \partial_\sigma f \partial_\sigma f E_s}{E_p + \partial_\sigma f E_s \partial_\sigma f} \right] d\varepsilon^{(i+1)} \quad (6.18)$$

6.4 Constitutive model for plain concrete

The constitutive model for plain concrete has been discussed in preceding Chapters, where it became clear that in applications to plain concrete the fracture energy-based plasticity model gives good results. The constitutive model for the tension-softening component of reinforced concrete is again assumed to be given by either the incremental or the total formulation.

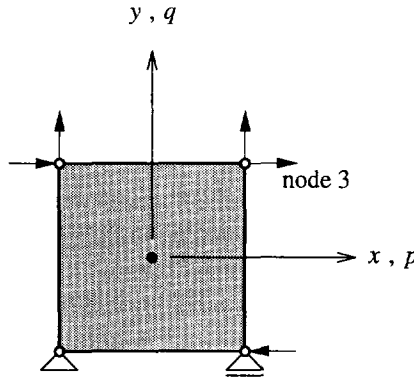


Figure 6.3 Idealized reinforced panel. Finite element configuration.

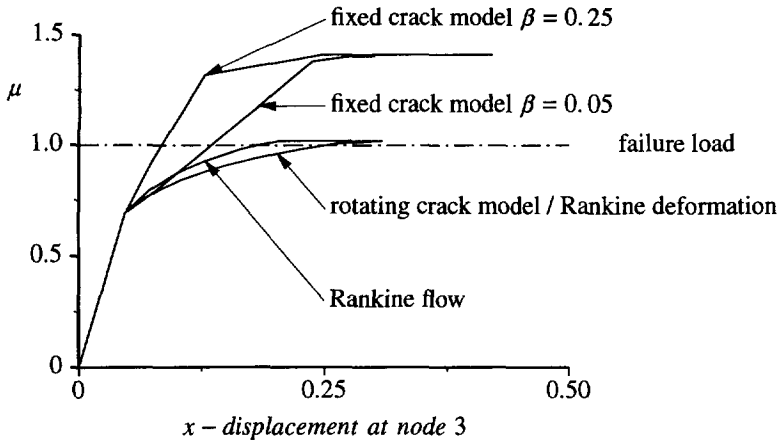


Figure 6.4 Idealized reinforced panel. Comparison of different concrete models.

Table 6.1 Material properties idealized panel.

	concrete	
E_c	20000	$[N/mm^2]$
ν	0.0	$[-]$
$f_{ct,m}$	0.0	$[N/mm^2]$
G_f	0.0	$[Nmm/mm^2]$
	reinforcement	
f_{sy}	500	$[N/mm^2]$
E_s	200000	$[N/mm^2]$

The different constitutive models have been applied to an idealized panel proposed by Crisfield and Wills (1987) in order to determine whether the same conclusion can be drawn regarding the constitutive model of plain concrete. The analysis concerns a single element, dimensions $10 \times 10 [mm^2]$ with a thickness of $1 [mm]$, reinforced with one layer of a reinforcing grid. The finite element configuration is shown in Figure 6.3. The reinforcement ratio in the p -direction is equal to 0.04232 and in the q -direction equal to 0.00768. The analysis concerns a no-tension analysis with linear-elastic behavior in compression which results in a limit analysis with the exact failure load. The material properties are given in Table 6.1. The panel is loaded in a combined biaxial tension-shear loading with $f_{xx} = f_{yy} = 2.5\mu [N/mm^2]$ and $f_{xy} = 5.0\mu [N/mm^2]$ with μ the loading parameter which is equal to one at the exact collapse load which is associated with yielding of the reinforcement, see Crisfield and Wills (1987). The results of the analyses are shown in Figure 6.4, where the loading parameter is plotted against the x -displacement of the upper-right node of the element. The comparison of the different

formulations of the constitutive model for plain concrete shows that the formulation is important even if the tensile strength is equal to zero and no tension-softening description is used. The interaction between the reinforcement and the concrete compressive struts after cracking results in different responses. The fixed crack model shows a collapse load which is too high, irrespective of the magnitude of the shear retention factor β . The rotating crack model and the plasticity-based models approximate the exact failure load. The responses of the rotating crack model and the Rankine plasticity model based on a deformation theory are identical, see also Crisfield and Wills (1987).

The choice of the constitutive model for plain concrete can be based on the fundamental difference which has been shown with this example. If the fixed crack model is adopted, the failure load will often be too high which has also been shown by Crisfield and Wills (1987) with the analyses of seven reinforced concrete panels tested by Vecchio and Collins (1982). The rotating crack model on the other hand gives failure loads which are in better agreement with the experimentally observed collapse loads. A deficiency of a total formulation, like the rotating crack model, is that a transparent combination with other nonlinear phenomena is often difficult and an incremental formulation is therefore preferred. The Rankine plasticity model with an incremental formulation shows a behavior which is quite similar to the behavior of the rotating crack model and can be used to model plain concrete. Because the Rankine model with isotropic hardening has shown to be accurate and stable in the previous Chapter, this model will be used in the remainder of this study.

6.5 Validation of the tension-stiffening model

The tension-stiffening effect is usually referred to in literature as the ability to gradually redistribute the load in a structure from concrete to steel under the formation of primary and secondary cracks. In this study however, the tension-stiffening effect is only used to define the additional stiffness due to the interaction between concrete and reinforcement whereas the formation of primary and secondary cracks has been modeled with the constitutive model of plain concrete, the tension-softening model.

The tension-stiffening model has been validated with experiments on reinforced concrete panels subjected to in-plane shear and normal loading. The loading regime and the properties of the reinforcement of the experiments are designed such that no rotation of the principal strain occurs after cracking. Only the model which describes the tension-stiffening effect is utilized and the dowel action is not activated. The panels are 890×890 [mm²] with a thickness of 70 [mm], reinforced with two layers of a reinforcing grid. The cover of the reinforcing grids is equal to 6 [mm] for all panels which have been analyzed. The finite element idealization for the analyses consists of a four-noded element with four integration points for both the reinforcement and the concrete, see Figure 6.5. The reinforcement in the panels is represented by the angle ψ between element x -axis and main reinforcement p -axis and the reinforcement ratio in p - and q -direction.

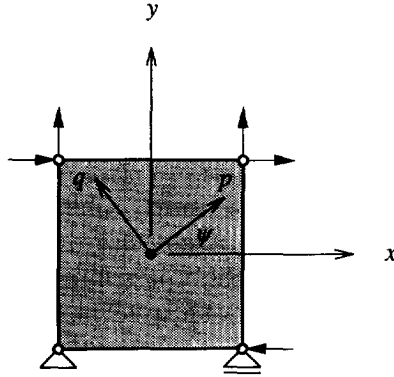


Figure 6.5 Finite element model of the reinforced concrete panels.

The tension-softening of the concrete has been applied with a linear diagram and the additional stress due to the tension-stiffening effect has been applied with the diagram given in Chapter 3.

The first analyses concern the panels of Bhide and Collins (1987) who tested a series of thirty-one, uniaxially reinforced concrete panels subjected to various combinations of tension and shear. For the validation of the tension-stiffening model two panels, panels pb13 and panel pb25, have been selected. Both panels have approximately the same material properties, but the reinforcement ratio of panel pb25 is twice the reinforcement ratio of panel pb13. The panels are both loaded in uniaxial tension in the direction of the reinforcement.

The reinforcement in panel pb13 is applied in two grids with a reinforcement ratio given by $\rho_p = 0.01085$ and $\rho_q = 0.0$ and an angle $\psi = 0^\circ$. The diameter of the deformed bars ϕ_p is equal to 6.55 [mm]. The material properties of panel pb13 are given in Table 6.2. The mean compressive strength of the concrete has been taken from the report of Bhide and Collins (1987) and the other material properties have been derived from this value with the formulas given in Chapter 3. The effective tension area determined by the geometrical properties of the reinforcement is equal to 23.2 [mm] and the average crack spacing is equal to 100 [mm]. Compared with the experimental stabilized crack spacing of approximately 111 [mm], the calculated value of the average crack spacing is reasonably accurate. The nominal tensile stress-strain diagram of panel pb13 is shown in Figure 6.6. The influence of the tension-stiffening component in the constitutive model is obvious from this diagram. The calculated force at cracking of the panel is too high which indicates that the tensile strength of the concrete is overestimated. This also influences the tension-stiffening effect which has been chosen with a value equal to one.

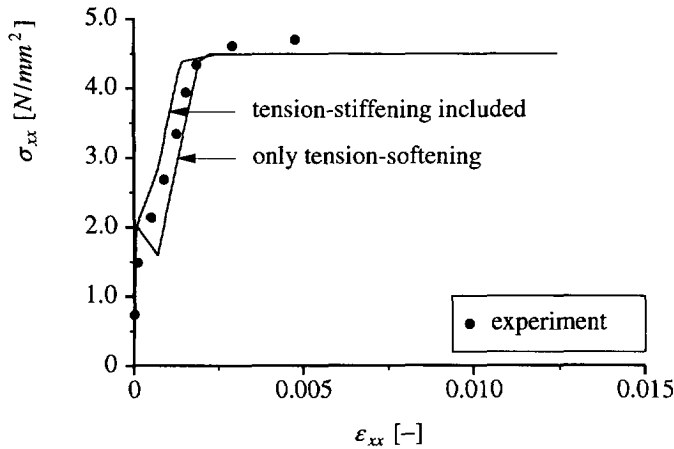


Figure 6.6 Influence of tension-stiffening on panel pb13 of Bhide and Collins.

Table 6.2 Material properties panel pb13.

concrete		
f_{cm}	23.4	$[N/mm^2]$
E_c	26000	$[N/mm^2]$
ν	0.15	$[-]$
$f_{ct,m}$	1.85	$[N/mm^2]$
G_f	0.06 ¹⁾	$[Nmm/mm^2]$
reinforcement		
f_{sy}	414	$[N/mm^2]$
E_s	210000	$[N/mm^2]$

1) linear softening

Panel pb25 has been designed to study the effect of the amount of reinforcement and this panel is the companion specimen of panel pb13. The reinforcement ratio of panel pb25 is twice the reinforcement ratio of panel pb13, i.e. $\rho_p = 0.02170$ with the same angle $\psi = 0^\circ$ and a diameter $\phi_p = 6.59 [mm]$. The reinforcement in the q -direction is again equal to zero. The material properties of panel pb25 are given in Table 6.3. The effective tension area determined by the geometrical properties of the reinforcement is equal to 23.2 $[mm]$ and the average crack spacing equal to 66.5 $[mm]$. Compared with the experimental crack spacing of approximately 81 $[mm]$, the calculated value of the average crack spacing is quite accurate. The nominal tensile stress-strain diagram of panel pb25 is shown in Figure 6.7. It is obvious from this diagram that the tension-softening component is more dominant for this panel than for panel pb13. The tension-stiffening is less important and has been modeled close to the experimental behavior.

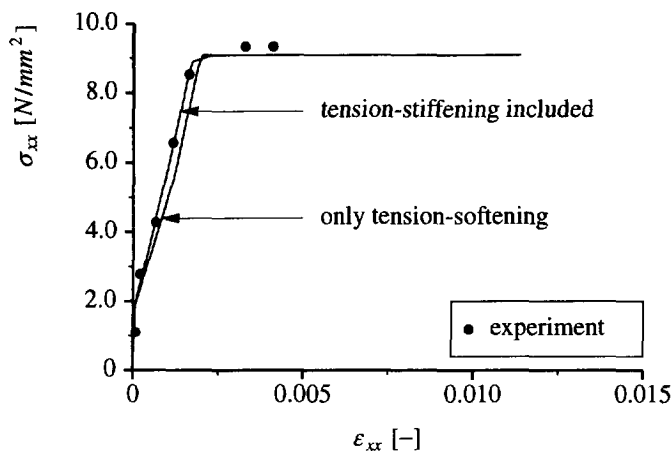


Figure 6.7 Influence of tension-stiffening on panel pb25 of Bhide and Collins.

Table 6.3 Material properties panel pb25.

concrete		
f_{cm}	20.0	[N/mm ²]
E_c	26000	[N/mm ²]
ν	0.15	[-]
$f_{ct,m}$	1.6	[N/mm ²]
G_f	0.06 ¹⁾	[Nmm/mm ²]
reinforcement		
f_{sy}	414	[N/mm ²]
E_s	210000	[N/mm ²]

1) linear softening

The influence of the angle between a crack and the reinforcement has been studied with the analyses of two panels tested by Kollegger (1988). It concerns two panels with the same material properties and equal reinforcement, but with a different reinforcement angle ψ . Panel pk03 has an angle ψ equal to 0°, whereas panel pk04 has an angle 45°. The material properties are given in Table 6.4. The reinforcement ratio in p - and q -direction is equal to 0.0106 with a diameter of 6.5 [mm]. The effective tension area is equal to 23.1 [mm] and the average crack spacing equal to 100 [mm] for panel pk03 and an average crack spacing equal to 70 [mm] for panel pk04 which is in agreement with the experimental value of the stabilized crack spacing. The nominal stress-strain response in the x -direction of panel pk03 has been depicted in Figure 6.8 and of panel pk04 in Figure 6.9.

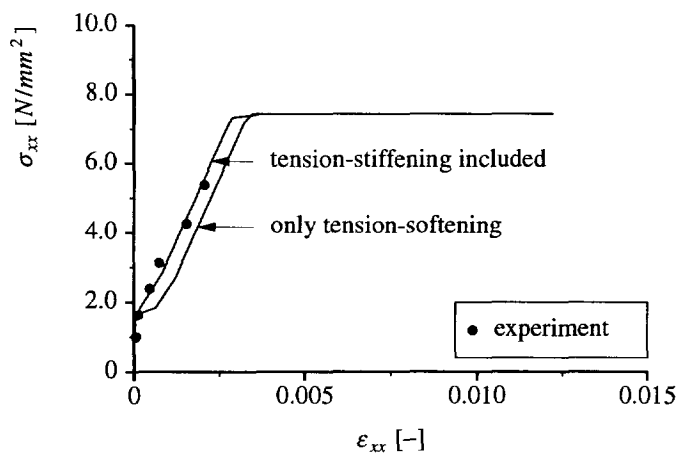


Figure 6.8 Influence of tension-stiffening on panel pk03 of Kollegger.

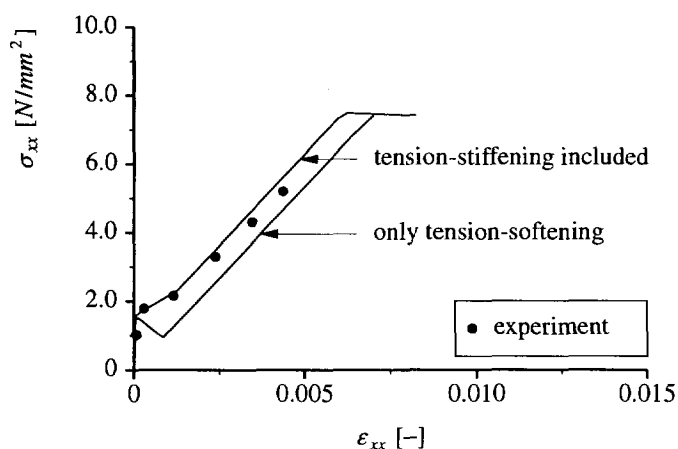


Figure 6.9 Influence of tension-stiffening on panel pk04 of Kollegger.

The assumption that the tension-stiffening component acts in the direction of reinforcement is supported by the analyses of the panels which show that the calculated behavior is close to the experimental behavior. The conclusion of Kollegger and Mehlhorn (1990b) that the influence of the angle between crack and reinforcement is negligible for the tension-stiffening model is confirmed by these analyses.

Table 6.4 Material properties panel pk03 and pk04.

concrete		
f_{cm}	20.0	$[N/mm^2]$
E_c	26000	$[N/mm^2]$
ν	0.15	$[-]$
$f_{ct,m}$	1.6	$[N/mm^2]$
G_f	0.06 ¹⁾	$[Nmm/mm^2]$
reinforcement		
f_{sy}	700	$[N/mm^2]$
E_s	210000	$[N/mm^2]$

1) linear softening

Finally, panel pv4 of Vecchio and Collins (1982) loaded in pure shear has been analyzed. Because of the isotropic reinforcement, the directions of the principal strain vector do not rotate and the behavior is completely determined by the tension-softening and tension-stiffening models. This panel is reinforced with two layers with a reinforcement ratio given by $\rho_p = \rho_q = 0.01056$ with a diameter $\phi_p = \phi_q = 3.45 [mm]$. The angle ψ between the reinforcement and the element axis is equal to 0° . The material properties of panel pv4 are given in Table 6.5. The effective tension area is equal to $19.3 [mm]$ and the average crack spacing equal to $44.8 [mm]$. The nominal shear stress-strain response of panel pv4 is shown in Figure 6.10. The calculated behavior of the panel is in close agreement with the experimental behavior which shows yielding of the reinforcement in both directions.

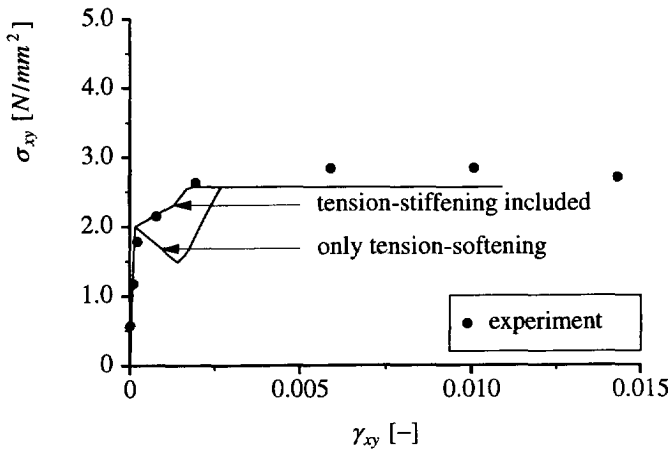


Figure 6.10 Influence of tension-stiffening on panel pv4 of Vecchio and Collins.

Table 6.5 Material properties panel pv4.

concrete		
f_{cm}	26.0	$[N/mm^2]$
E_c	30000	$[N/mm^2]$
ν	0.15	$[-]$
$f_{ct,m}$	2.0	$[N/mm^2]$
G_f	0.06 ¹⁾	$[Nmm/mm^2]$
reinforcement		
f_{sy}	242	$[N/mm^2]$
E_s	210000	$[N/mm^2]$

1) linear softening

The following analyses will concern reinforced panels of Vecchio and Collins (1982) which are anisotropically reinforced. Due to this anisotropy, the direction of the principal strain will change after crack initiation. The degree of anisotropy is defined by the ratio of the potential yield loads of the reinforcement, Crisfield and Wills (1989), as

$$\omega_r = \frac{\rho_p f_{sy,p}}{\rho_q f_{sy,q}} \quad (6.19)$$

The analyses are performed with the finite element configuration shown in Figure 6.5 and all panels are loaded in pure shear.

The first analysis concerns panel pv11 with a reinforcement ratio in the p -direction equal to 0.01785 with a diameter of 6.35 [mm] and in the q -direction equal to 0.01306 with a diameter of 5.44 [mm]. This results in an anisotropy factor of the reinforcement $\omega_r = 1.37$. The reinforcement properties result in an effective tension area of 22.9 [mm] in the p -direction and 21.8 [mm] in the q -direction. The average crack spacing is equal to 51.5 [mm] which is smaller than the experimentally observed crack spacing of 75 – 100 [mm]. The material properties are given in Table 6.6. The nominal shear stress-shear strain response is given in Figure 6.11. The agreement between analysis and experiment is reasonable if the tension-stiffening effect is taken into account. The tensile strength of 1.2 $[N/mm^2]$ which has been estimated by eq.(3.11) is lower than the experimentally observed tensile strength of approximately 1.6 $[N/mm^2]$. It is obvious in this case, with an anisotropy factor $\omega_r = 1.37$ that ignoring the shear resistance of the reinforced concrete is permitted.

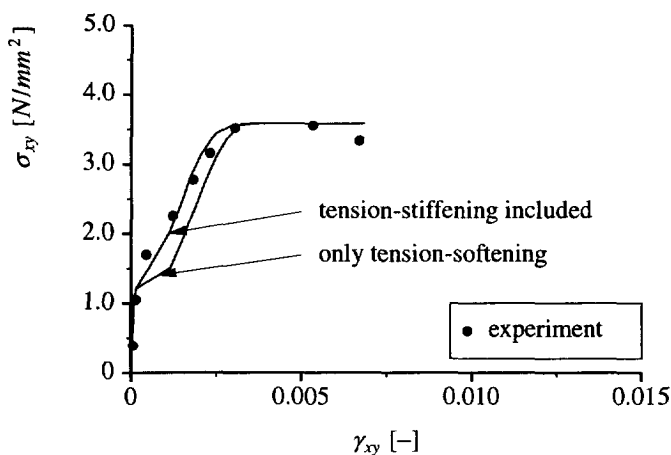


Figure 6.11 Influence of tension-stiffening on panel pv11 of Vecchio and Collins.

Table 6.6 Material properties panel pv11.

concrete		
f_{cm}	16.0	[N/mm ²]
E_c	25000	[N/mm ²]
ν	0.15	[-]
$f_{ct,m}$	1.2	[N/mm ²]
G_f	0.06 ¹⁾	[Nmm/mm ²]
reinforcement		
f_{sy}	235	[N/mm ²]
E_s	210000	[N/mm ²]

1) linear softening

The next panel concerns panel pv10 with an anisotropy factor $\omega_r = 1.79$. The reinforcement ratio in the p -direction is equal to 0.01785 with a diameter of 6.35 [mm] and in the q -direction equal to 0.00999 with a diameter of 4.70 [mm] which results in an effective tension area of 22.9 [mm] in the p -direction and 20.8 [mm] in the q -direction. The average crack spacing is equal to 51.4 [mm] which is in agreement with the experimentally observed crack spacing of 50 – 75 [mm]. The material properties are given in Table 6.7. The nominal shear stress-shear strain response is given in Figure 6.12. The comparison of the analysis with the experiment shows that the tensile strength is again estimated too low, but that the resemblance is reasonable. The influence of the tension-stiffening component is small because the amount of ultimate crack strain is almost equal to the failure strain of the element.

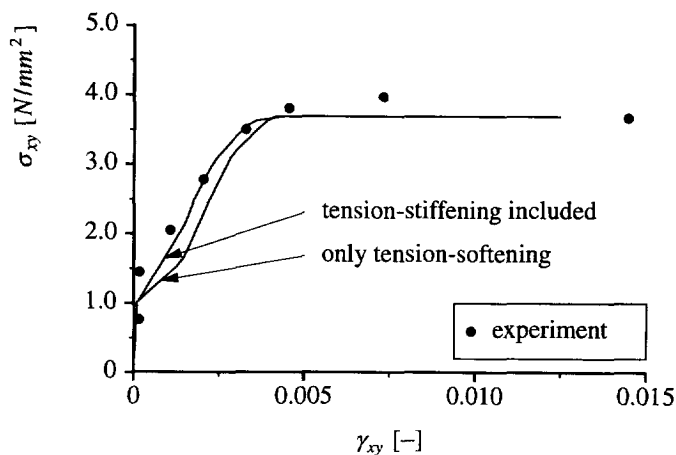


Figure 6.12 Influence of tension-stiffening on panel pv10 of Vecchio and Collins.

Table 6.7 Material properties panel pv10.

concrete		
f_{cm}	14.4	[N/mm ²]
E_c	24000	[N/mm ²]
ν	0.15	[-]
$f_{ct,m}$	1.0	[N/mm ²]
G_f	0.06 ¹⁾	[Nmm/mm ²]
reinforcement		
f_{sy}	276	[N/mm ²]
E_s	210000	[N/mm ²]

1) linear softening

The next panel concerns panel pv19 where the anisotropy factor ω_r is equal to 3.83 which is large, considering the pure shear loading. The reinforcement is applied in two layers of reinforcing grids with a reinforcement ratio in the p -direction equal to 0.01785 with a diameter of 6.35 [mm] and in the q -direction equal to 0.00713 with a diameter of 4.01 [mm]. These properties result in an effective tension area of 22.9 [mm]. The average crack spacing is equal to 51.4 [mm] which is in agreement with the experimentally observed crack spacing of 50 – 75 [mm]. The yield stress of the reinforcing steel is different in the p - and q -directions, see Table 6.8. The nominal shear stress-shear strain response given in Figure 6.13 shows that the agreement with the experimental response is quite accurate, considering that the shear resistance is neglected.

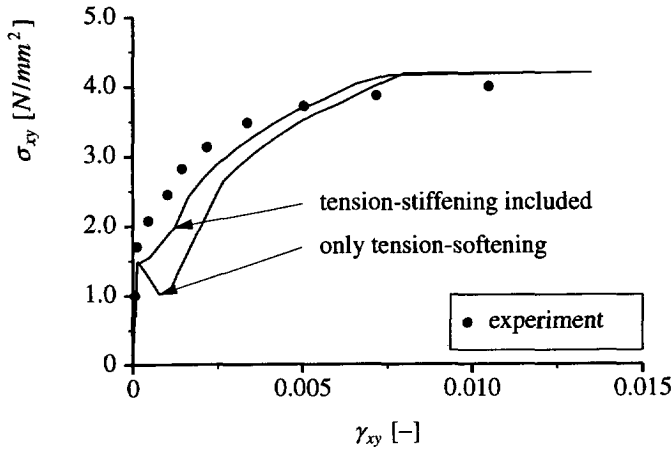


Figure 6.13 Influence of tension-stiffening on panel pv19 of Vecchio and Collins.

Table 6.8 Material properties panel pv19.

concrete		
f_{cm}	19.0	[N/mm ²]
E_c	26000	[N/mm ²]
ν	0.15	[-]
$f_{ct,m}$	1.5	[N/mm ²]
G_f	0.06 ¹⁾	[Nmm/mm ²]
reinforcement		
$f_{sy,p}$	458	[N/mm ²]
$f_{sy,q}$	299	[N/mm ²]
E_s	210000	[N/mm ²]

1) linear softening

The final panel which will be analyzed is panel pv12 which has a large anisotropy factor $\omega_r = 6.98$. This large anisotropy factor produces a significant change in the principal strain directions. The reinforcement is applied in two layers of reinforcing grids with a reinforcement ratio in the p -direction equal to 0.01785 with a diameter of 6.35 [mm] and in the q -direction equal to 0.00446 with a diameter of 3.18 [mm]. These properties result in an effective tension area of 22.4 [mm]. The average crack spacing is equal to 51.4 [mm] which is in agreement with the experimentally observed crack spacing of 50 – 75 [mm]. The yield stress of the reinforcing steel is different in the p - and q -direction, which are given in Table 6.9.

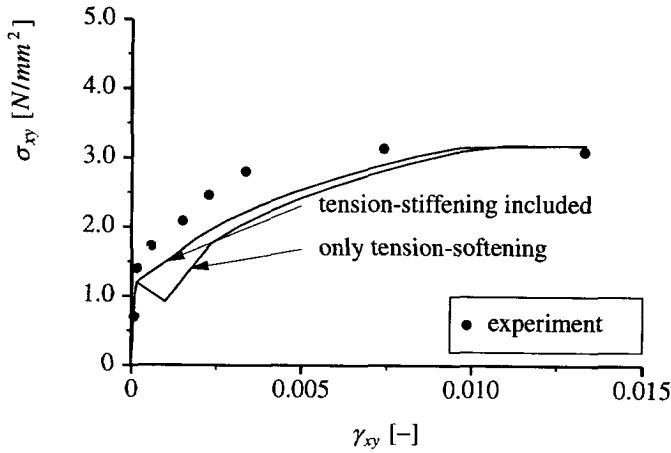


Figure 6.14 Influence of tension-stiffening on panel pv12 of Vecchio and Collins.

Table 6.9 Material properties panel pv12.

concrete		
f_{cm}	16.0	[N/mm ²]
E_c	25000	[N/mm ²]
ν	0.15	[-]
$f_{ct,m}$	1.2	[N/mm ²]
G_f	0.06 ¹⁾	[Nmm/mm ²]
reinforcement		
$f_{sy,p}$	469	[N/mm ²]
$f_{sy,q}$	269	[N/mm ²]
E_s	210000	[N/mm ²]

1) linear softening

The nominal shear stress-shear strain response is given in Figure 6.14. It is clear from the analysis of panel pv12 that the shear resistance of the cracked reinforced concrete becomes more important if the directions of the principal strain vector change significantly. However the ultimate failure load is not affected if the failure mode is governed by yielding of the reinforcement.

It is concluded that neglecting the shear resistance of the cracked reinforced concrete is allowed as long as the anisotropy of the reinforcement is less than five and the loading is such that rotation of the principal directions can be expected. In cases where the structure is reinforced only in one direction, the Rankine model should be used with care, because the analysis might show a much too brittle response due to continuously rotation of the principal stress.

7. APPLICATION TO REINFORCED CONCRETE

The previous Chapters have been addressed the two major problem areas in the modeling of reinforced structures, i.e. the development of a numerically stable algorithm which deals with the biaxial stress states and the rational modeling of the tension-stiffening concept. In this Chapter, two typical engineering problems will be presented which show the range of application of the developed models. The first example concerns the analyses of two deep beams without shear reinforcement which are designed to fail in compression. The proper modeling of the biaxial stress state is important for these type of structures. The second example concerns the analyses of shear wall panels in which both the biaxial stress state problems and the tension-stiffening problems will be encountered.

7.1 Analysis of deep beams

The analysis of deep beams is usually performed using an approach in which the structure is modeled using compressive struts and tensile ties. The experimental research program of Lehwalter (1988) was mainly concerned with the carrying-capacity of the compressive struts in this truss-model approach. The program consisted of two series of tests, the first series consisting of deep beams without shear reinforcement and the second series consisting of deep beam with shear reinforcement. The beams have a densely reinforced layer at the bottom of the beams which is designed such that the beams fail due to compressive failure without yielding of the reinforcement. Two beams of the first series have been selected, beam v023 with a depth over span ratio of 0.5, and beam v121 with a depth over span ratio of 1.0. Both beams have a thickness of 250 [mm].

The first analysis concerns beam v023 with a depth of 360 [mm] and a span of 720 [mm]. Only a half of the specimen has been modeled using 400 four-noded plane-stress elements with a 4-point integration scheme. The reinforcement with a total area $A_s = 1020 \text{ [mm}^2\text{]}$ has been modeled using embedded bar elements. The developed model for the reinforced concrete has not been used in this analysis since it is believed that the concrete-reinforcement interaction does not have a large influence on the ultimate failure load of the structure. These examples have been selected merely to indicate the importance of the modeling of the biaxial stress state. The support platen has been modeled with eight four-noded plane-stress elements also with a four-point integration scheme. The finite element mesh is shown in Figure 7.1 and the material properties are given in Table 7.1. The analyses have been performed with the solution strategy which has been proposed in Chapter 2 without any modification. The sign of the initial incremental load factor has been determined in the pre-peak regime with the displacement-based method, because negative pivots are expected in the range where the bending cracks tend to localize. After the cracks have developed, the sign of the initial load increment has been determined with the pivot-based method.

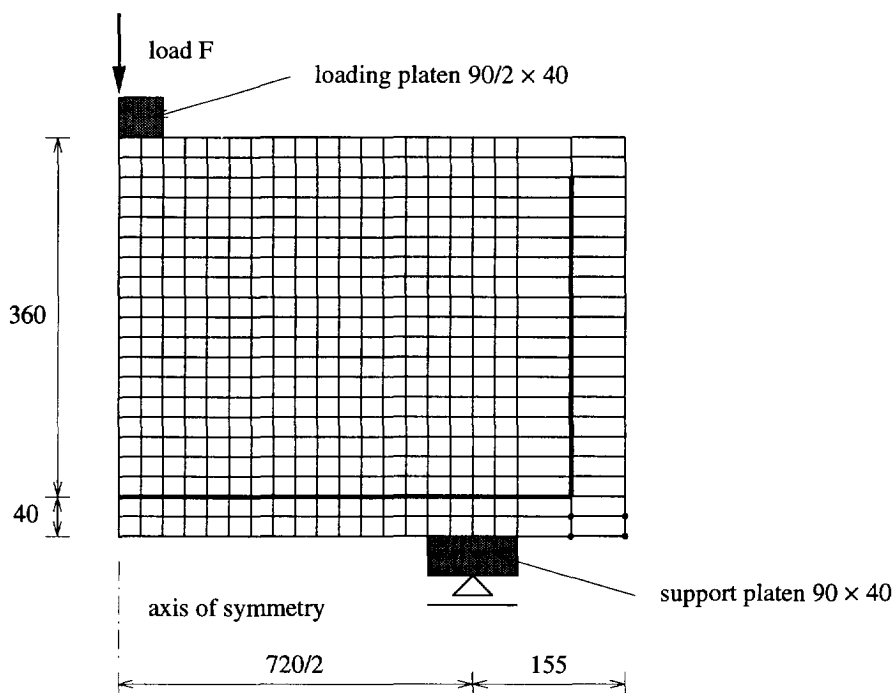


Figure 7.1 Deep beam v023 Lehwalter. Finite element mesh. Measures in [mm].

Table 7.1 Material properties deep beam v023.

concrete		
f_{cm}	20.0	[N/mm ²]
E_c	30000	[N/mm ²]
ν	0.15	[-]
$f_{ct,m}$	2.0	[N/mm ²]
G_f	0.10 ¹⁾	[Nmm/mm ²]
G_c	10.0 ²⁾	[Nmm/mm ²]
reinforcement		
f_{sy}	420 – 500 ³⁾	[N/mm ²]
E_s	210000	[N/mm ²]

1) exponential softening

2) parabolic softening

3) hardening of steel with $\varepsilon_{sv} = 0.079$ [-]

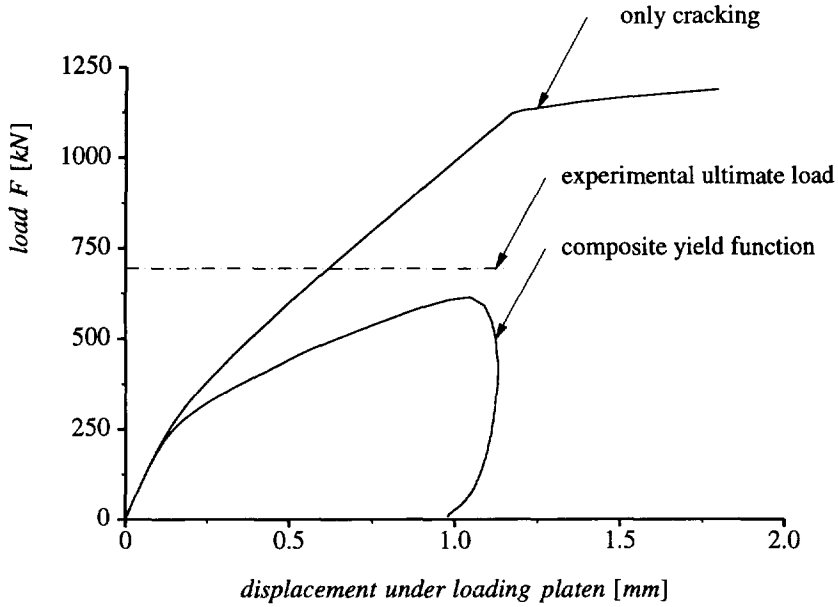


Figure 7.2 Deep beam v023 Lehwalter. Load - displacement diagram.

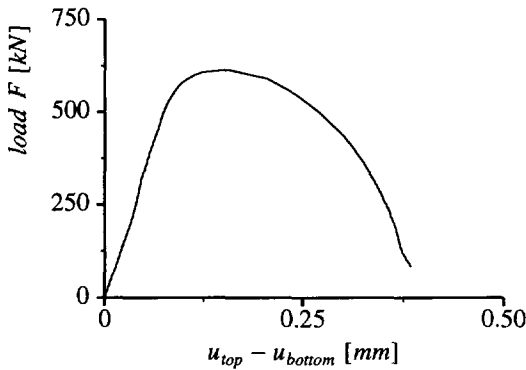


Figure 7.3 Deep beam v023 Lehwalter. Difference in the displacement of the midspan top and bottom of the beam.

The vertical displacement of the loading platen has been plotted against the load in Figure 7.2 in which the influence of compressive softening on the structural behavior is evident. If only cracking is taken into account, the analysis clearly shows first cracking and finally yielding of the reinforcement. The kinematic or isotropic hardening models give identical responses. The analysis with a composite yield surface shows that the nonlinear compressive behavior under the loading platen dominates the structural response. The failure load which has been obtained in the analysis with a composite

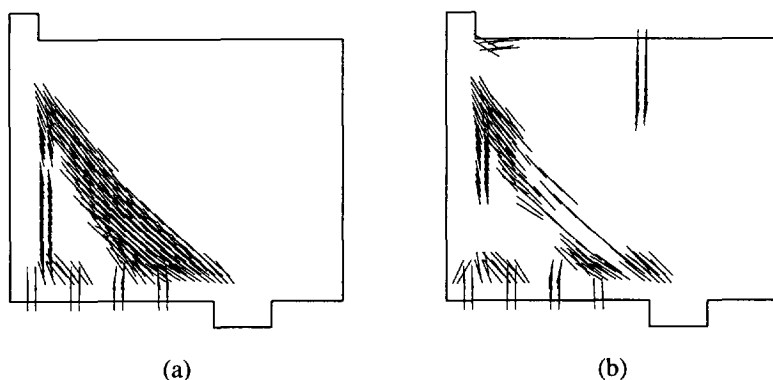


Figure 7.4 Deep beam v023 Lehwalter. Crack pattern. (a) at maximum load ; (b) at final load

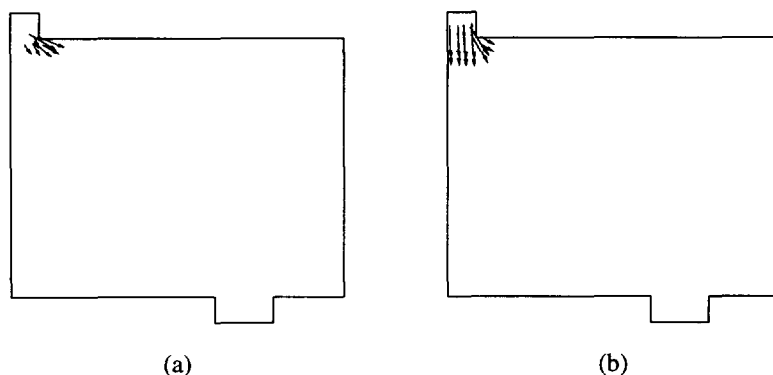


Figure 7.5 Deep beam v023 Lehwalter. Compressive principal plastic strain. (a) at maximum load ; (b) at final load

yield surface is in good agreement with the experimental failure load. The experimental load-deformation response has not been plotted because the measured response was inaccurate due to deformation of the supports, see Lehwalter (1988) and Walraven (1993). Only the experimental failure load has been depicted in Figure 7.2. The crack pattern which have been obtained with the composite yield surface is depicted in Figure 7.4. The distributed crack pattern around the reinforced area localizes in a dominant vertical crack. At a later stage the diagonal, densely cracked region develops. The crack pattern at the final stage shows that the diagonal cracks are closing while a vertical crack starts to develop above the support which has also been observed in the experiment. The compressive principal inelastic strain vectors depicted in Figure 7.5 shows that the failure mode is a local, compressive type of failure due to nonlinear compressive behavior. This is also clear from Figure 7.3 in which the difference between the displacement of the top and bottom at the midspan of the beam has been plotted. The load-displacement

curve shows a monotonically increasing behavior, whereas the load-displacement curve of the loading platen, depicted in Figure 7.2, shows a snap-back behavior. The structure unloads at the final stage, but the difference between the displacements under the loading platen and the bottom of the beam shows that we have an increasing deformation under the loading platen. The analysis of beam v023 shows that the behavior of the beam is governed by bending cracks and compression-shear cracks in the pre-peak regime. The ultimate failure mechanism is dominated by compressive softening under the loading platen, which results in a very brittle failure mechanism which is indicated by the snap-back in the load-displacement diagram. If only cracking is modeled, the ultimate failure mechanism is dominated by yielding of the reinforcement with an over-estimation of the ultimate load with approximately a factor equal to 2, and results in a too ductile failure mechanism.

The second analysis concerns beam v121 with a depth of 930 [mm] and a span of 930 [mm]. Only half of the structure has been modeled using 220 four-noded plane-stress elements with a four-point integration scheme. The reinforcement has been modeled using embedded bar elements. The support platens have been modeled with four four-noded plane-stress elements also with a four-point integration scheme. The finite

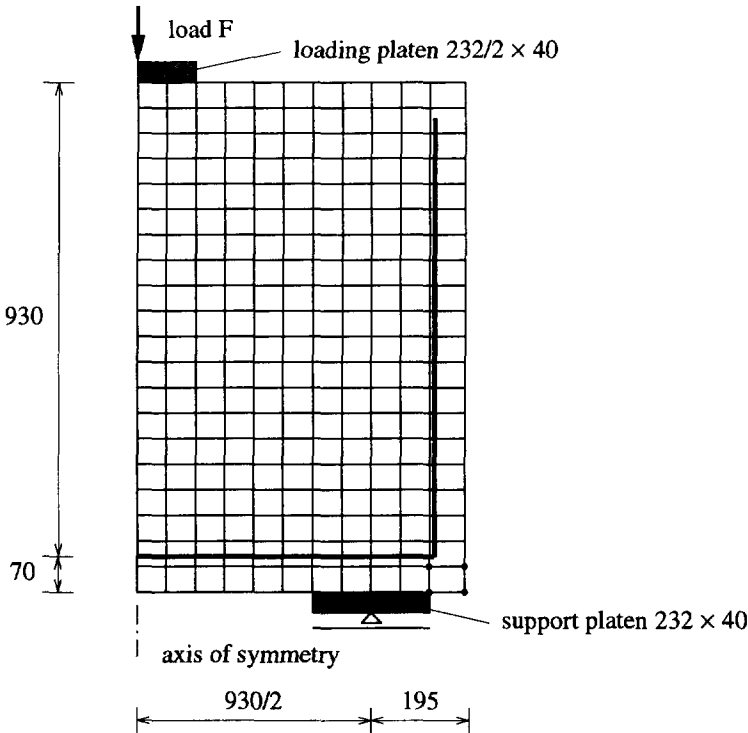


Figure 7.6 Deep beam v121 Lehwalter. Finite element mesh. Measures in [mm].

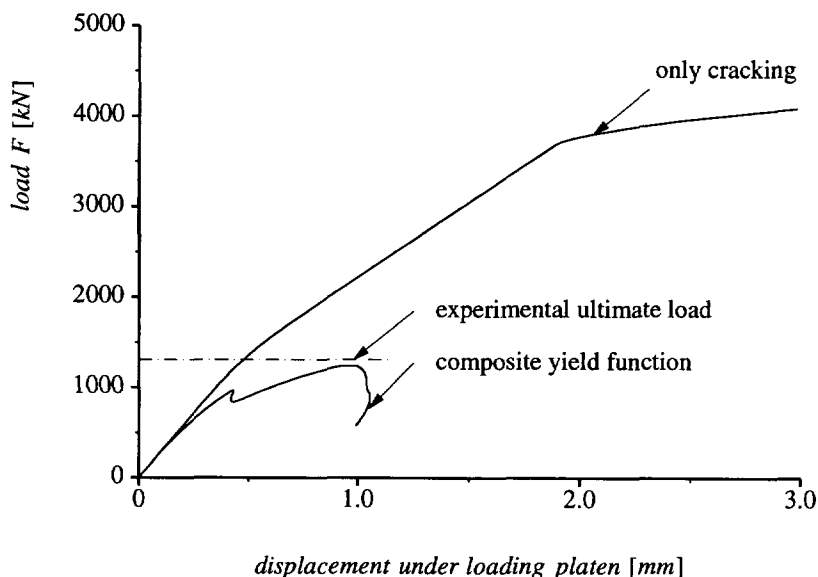


Figure 7.7 Deep beam v121 Lehwalter. Load - displacement diagram.

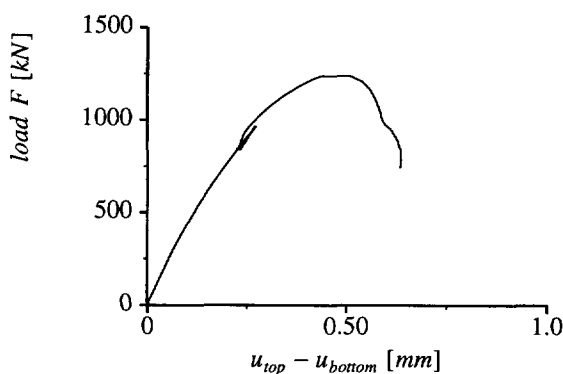


Figure 7.8 Deep beam v121 Lehwalter. Difference in the displacement of the midspan top and bottom of the beam.

element mesh is depicted in Figure 7.6, and the material properties are equal to the material properties of beam v023 which have been given in Table 7.1. Again, the vertical displacement of the loading platen has been plotted against the applied load in Figure 7.7 in which the influence of compressive softening on the structural behavior is even more evident than for the previous structure. If only cracking is taken into account, the analysis shows a decrease in the stiffness due to cracking and finally yielding of the reinforcement. The analysis with a composite yield surface shows that the nonlinear compressive behavior under the loading platen results in a large decrease of the

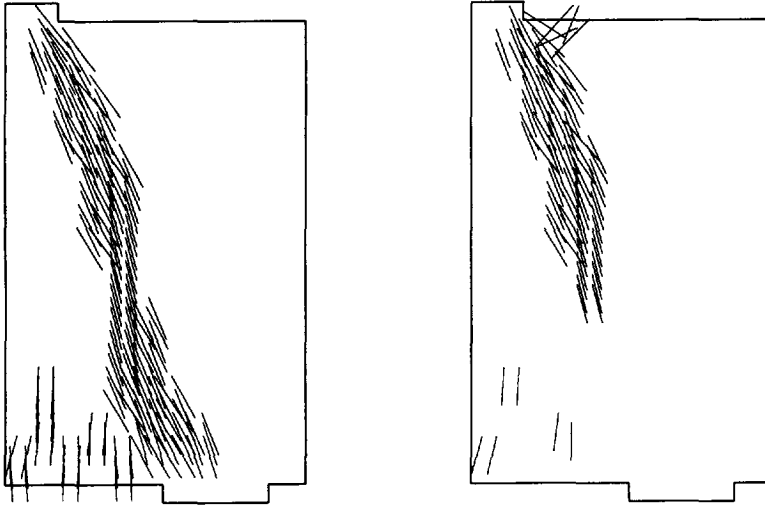


Figure 7.9 Deep beam v121 Lehwalter. Crack pattern (a) at maximum load ; (b) at final load

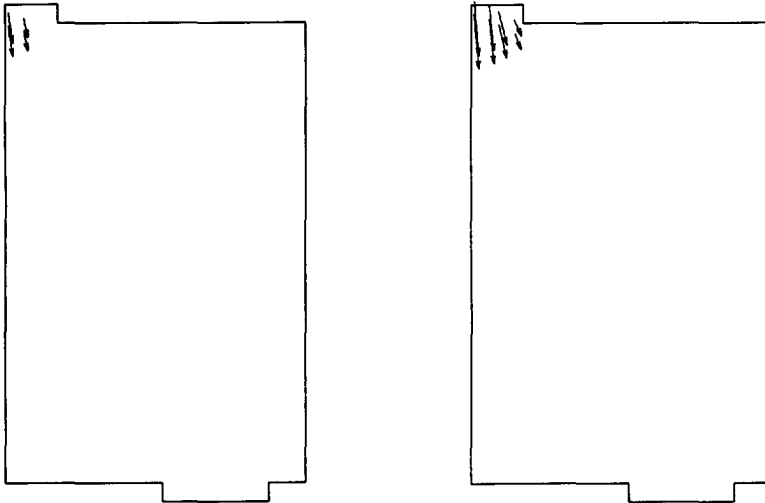


Figure 7.10 Deep beam v121 Lehwalter. Compressive principal plastic strain. (a) at maximum load ; (b) at final load

maximum load and that it is important to incorporate compressive softening in order to accurately predict the failure load of these types of deep beams. The calculated failure load is in good agreement with the experimental failure load which have been plotted in

Figure 7.7. Again, only the maximum experimental failure load has been plotted, since the load-deflection curve which has been measured is inaccurate because of displacements of the supports. The difference between the displacement of the loading platen and the deflection of the midspan of the beam is shown in Figure 7.8. The calculated crack pattern which is shown in Figure 7.9, indicates that the structure is mainly subjected to a compression-shear loading, because the bending cracks are less dominant than in the previous structure. At the maximum load we observe some small bending cracks in the middle of the structure with a dominant shear-type crack pattern in the compressive strut. The failure mode is governed by the compressive softening under the loading platen which is shown in Figure 7.10. This local failure mechanism causes an unloading of the structure which has also been observed in the previous example.

The two analyses of the deep beams show the major influence of compressive softening on the structural failure mechanism.

7.2 Analysis of shear wall panels

The analysis of shear wall panels is a good example of the possible application of the developed models. The stress state in the panels can be considered to be in tension-compression. The panels are usually reinforced by a reinforcing grid which makes the examples also a good indicator for the influence of the tension-stiffening on the behavior of the panels. The panels which will be presented in this study have been tested at the E.T.H. of Zürich by Maier and Thürlimann (1985) and have been analyzed before with the finite element package DIANA by Wang, Van der Vorm and Blaauwendraad (1990). The constitutive model which has been used in that study is a combination of a fixed crack model to describe the tensile stress state and a Mohr-Coulomb plasticity model to describe the compressive stress states, see for details about this constitutive model Van der Vorm (1988). However, the combination of cracking and plasticity resulted in convergence problems if a large region existed in which both the cracking and the plasticity model became active. These numerical problems were solved by defining two areas in which either only the cracking model or only the plasticity model could become active. The solutions which were obtained with this approach are in good agreement with the experimental results which indicates that the method is rather effective. The arbitrariness of defining the regions a-priori is a major draw-back of this method and the analyses with the combined yield surface presented here will show that the convergence problems are avoided if a stable algorithm is used to describe the constitutive behavior. The experimental program of Maier and Thürlimann (1986), concerned a series of 10 shear wall panels with flanges and panels without flanges. The panels are all loaded initially by a vertical compressive force, and then loaded by a horizontal force until the experiment became unstable and the failure load had been reached. The experimental set-up is shown in Figure 7.11, with the panels supported on a base block and loaded through a thick top slab.

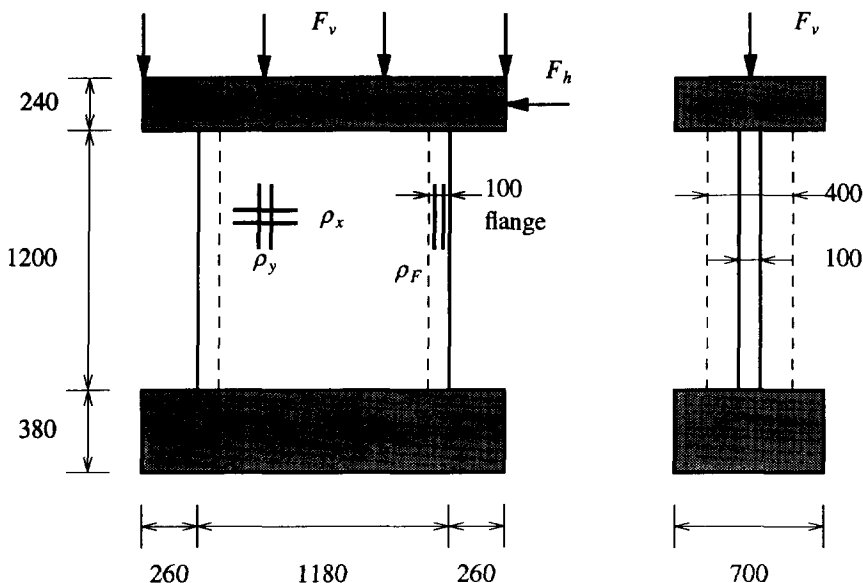


Figure 7.11 Experimental set-up. Measures in [mm].

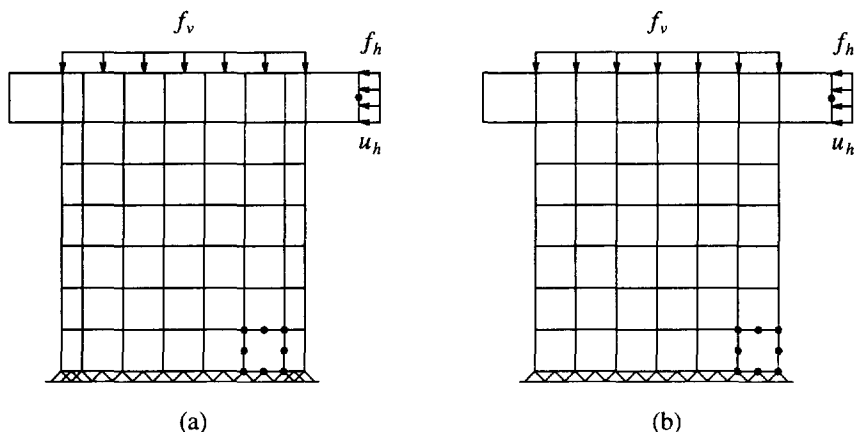


Figure 7.12 Finite element discretization panels Maier and Thürlimann (1985).
a) panels S1 and S2 ; b) panels S4 and S10

Four panels from the experiments, S1, S2, S4 and S10, have been analyzed with the composite plasticity model and the influence of the tension-stiffening component on the behavior has been examined. The material properties have been averaged from the experimental data of the four panels provided by Thürlimann and Maier (1986) with a reduction of the compressive strength of 20 %. The material properties which have been used in the analyses are given in Table 7.2. The material properties have been

averaged in order to simulate the behavior of the panels in a qualitative manner. In this way, it is better possible to study the influence of the different reinforcement ratio, initial vertical stress and geometry. The reinforcement is applied by reinforcing grids in two directions with a diameter of 8 [mm] and a clear cover of 10 [mm]. The reinforcement ratios and the initial vertical force are given in Table 7.3.

Table 7.2 Material properties panels Maier and Thürlimann (1985).

concrete		
f_{cm}	27.5	[N/mm ²]
E_c	30000	[N/mm ²]
ν	0.15	[-]
$f_{ct,m}$	2.2	[N/mm ²]
G_f	0.07 ¹⁾	[Nmm/mm ²]
G_c	50.0 ²⁾	[Nmm/mm ²]
reinforcement		
f_{sy}	574 – 764 ³⁾	[N/mm ²]
E_s	200000	[N/mm ²]

1) linear softening

2) parabolic softening

3) hardening of steel with $\varepsilon_{sv} = 24.6 \cdot 10^{-3}$ [-]

Table 7.3 Reinforcement and vertical load of panels Maier and Thürlimann (1985).

Panel	ρ_x [10 ⁻³]	ρ_y [10 ⁻³]	ρ_F [10 ⁻³]	F_v [kN]
S1	10.3	11.6	11.6	-433
S2	10.3	11.6	11.6	-1653
S4	10.3	10.5	10.5	-262
S10	9.8	10.0	57.1 ¹⁾	-262

1) additional reinforcement in tension area over 197 [mm]

The finite element discretizations of the panels are depicted in Figure 7.12 with quadratic plane-stress elements with a nine-point Gaussian integration for both the reinforcement and the element. The reinforcement has been applied in two layers of a reinforcing grid. The top slab has been modeled with linear-elastic elements without reinforcement, whereas the supporting block has been replaced by fixed supports in the x - and y -direction. The additional reinforcement in panel S10 has not been applied in an area of 240 [mm] as in the experiments, but has been applied in the first element at the tension side, i.e. over a length of 197 [mm].

The horizontal and vertical load have been applied as a uniformly distributed element load as indicated in Figure 7.12. The horizontal displacement u_h of the top slab

has been monitored and compared with the experimental load-displacement curves. Initially, the solution technique with the constrained Newton-Raphson iteration with line searches has been applied to analyze the panels. It happened that it was not possible to achieve converged solutions after the maximum load and therefore the indirect displacement control method without line searches has been used to analyze these panels. The displacement in the horizontal direction u_h has been chosen as the active degree-of-freedom with load steps of approximately 0.2 [mm]. With this solution technique, converged solutions could be obtained in the complete loading regime.

The first panel which will be presented is a panel with flanges which will be denoted as panel S1. This panel is subjected to an initial vertical load of 433 [kN] $\equiv 2.5$ [N/mm²] which results in an initial horizontal displacement of 0.06 [mm] in the experiment. The calculated initial displacement is equal to $-80 \cdot 10^{-6}$ [mm] which indicates a possible eccentricity in the experimental set-up. After the initial vertical load, the horizontal load is applied with indirect displacement control. The load-displacement diagram of panel S1 is shown in Figure 7.13, which shows a reasonable agreement between experimental and calculated response. The influence of the tension-stiffening component on the load-displacement diagram is small, but including of the tension-stiffening avoids some numerical difficulties which are related to local maxima due to crack localization in the pre-peak regime. The results of the analysis will be presented by plotting the active cracks, the integration points which are in a compressive plastic state and the principal stresses which are in general compressive.

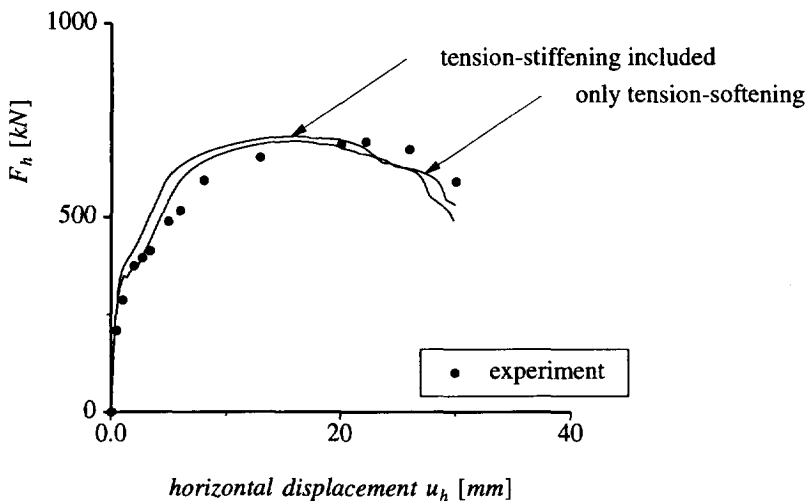


Figure 7.13 Panel S1. Load - displacement diagram.

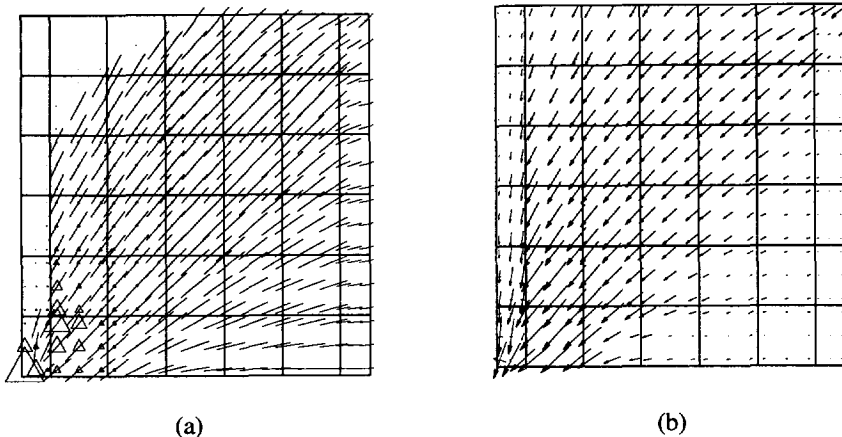


Figure 7.14 Panel S1. Results of the analysis at a displacement of 10 [mm]. (a) active cracks and plastic points ; (b) principal stresses.

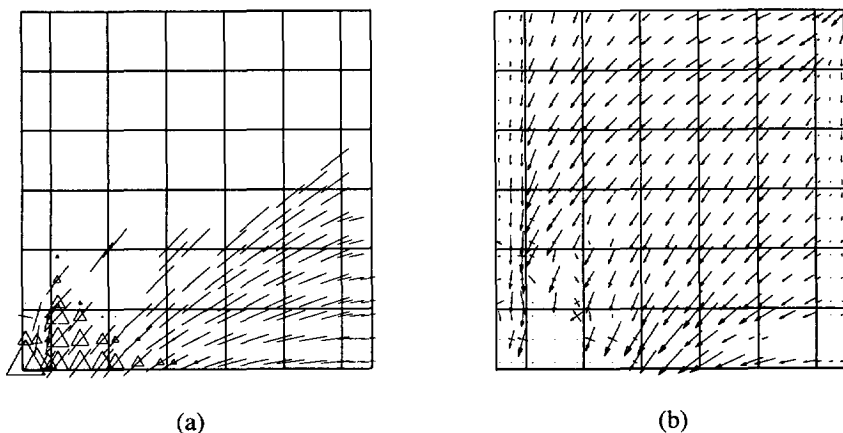


Figure 7.15 Panel S1. Results of the analysis at a displacement of 30 [mm]. (a) active cracks and plastic points ; (b) principal stresses.

The active cracks are defined as those cracks for which the internal parameter κ_T is equal or greater than $0.5 \kappa_u$. The results for panel S1 at a displacement of the top slab of 10 [mm] are shown in Figure 7.14. The panel is densely cracked with plastic points in the bottom-left corner of the panel. The concrete in the bottom-right corner does not transfer any stress anymore as can be seen from Figure 7.14(b). The load carrying mechanism through a compressive strut can clearly be observed from the principal stresses. The results of panel S1 at the final displacement of 30 [mm] show the failure mechanism which is governed by compressive softening of the concrete and yielding of the reinforcing steel both in tension and compression, see Figure 7.15. In the ultimate

state, the concrete in the bottom-left corner transfers no stress anymore, which is in agreement with the experimentally observed failure mechanism where the concrete was crushed in the bottom-left corner of the panel and in the flange at the compression side.

Panel S2 is identical with the previous panel, but the initial vertical load is approximately four times the initial stress in panel S1, which increases the ultimate load of the structure but decreases the ductility of the panel dramatically, see Figure 7.16. The agreement between the ultimate load of the experiment and the calculated maximum load is good. The influence of the additional stiffness if the tension-stiffening component is included is small. The experimental initial displacement of the experiment is quite large, which could not be simulated. The experimental failure mechanism was rather explosive and caused a complete loss of load-carrying capacity which can be explained by the brittle behavior of the panel after maximum load, see Figure 7.16. The results of the analysis at a displacement u_h equal to 5 [mm], see Figure 7.17, shows that the panel is densely cracked with plastic points in the bottom-left corner of the panel and in the compressive flange. The results of panel S2 at the ultimate displacement u_h of 15 [mm] are shown in Figure 7.18 in which the redistribution of internal forces in the panel can clearly be observed. The complete loss of stiffness in the bottom of the panel can be seen from Figure 7.18 which is combined with yielding of the reinforcement in compression. The reinforcement in the tension flange also yields, but this is less dominant.

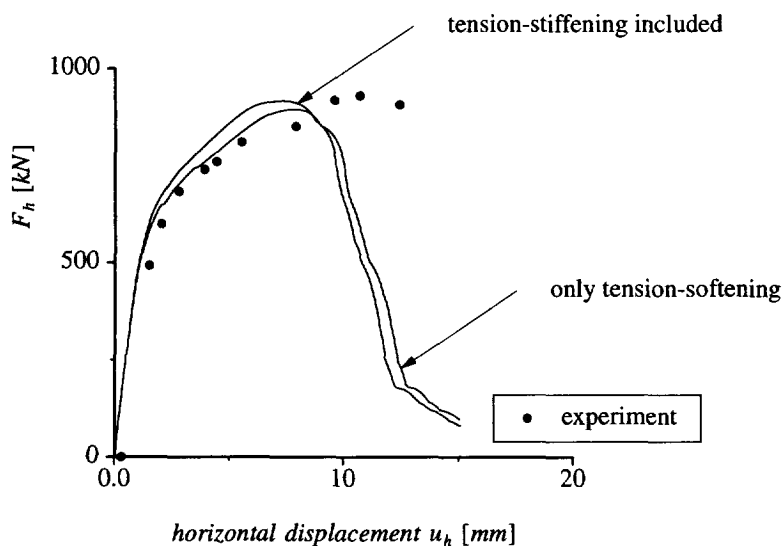


Figure 7.16 Panel S2. Load - displacement diagram.

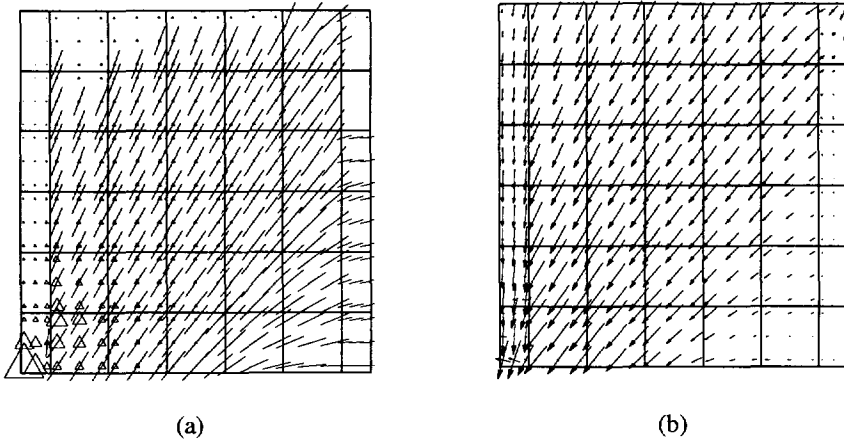


Figure 7.17 Panel S2. Results of the analysis at a displacement of 5 [mm]. (a) active cracks and plastic points ; (b) principal stresses.

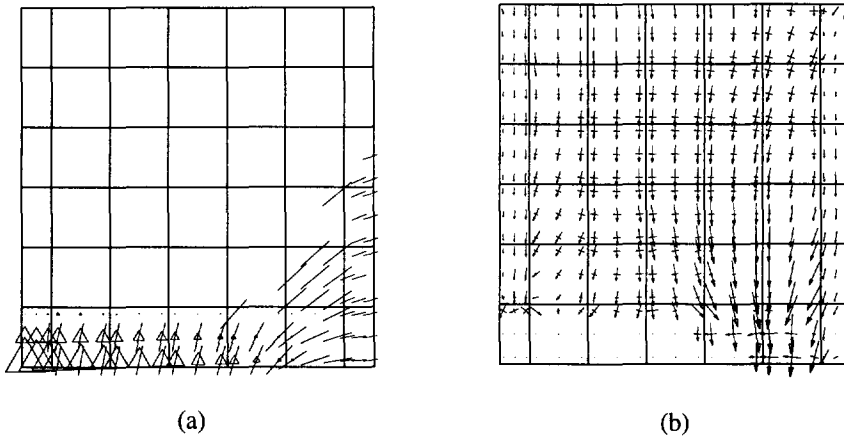


Figure 7.18 Panel S2. Results of the analysis at a displacement of 15 [mm]. (a) active cracks and plastic points ; (b) principal stresses.

Panel S4, which will be analyzed next, is the equivalent of panel S1 without flanges. The initial vertical force of 262 [kN] results in approximately equal vertical stresses as in panel S1. The load-displacement diagram is given in Figure 7.19 which shows again a reasonable agreement between the ultimate load in the experiment and in the analysis. The influence of the tension-stiffening component is more dominant and results in a more stable numerical solution than if the tension-stiffening component is neglected. In this case convergence could only be achieved with small steps in the ascending branch until a stabilized crack pattern has been achieved. The panel behaves in a rather

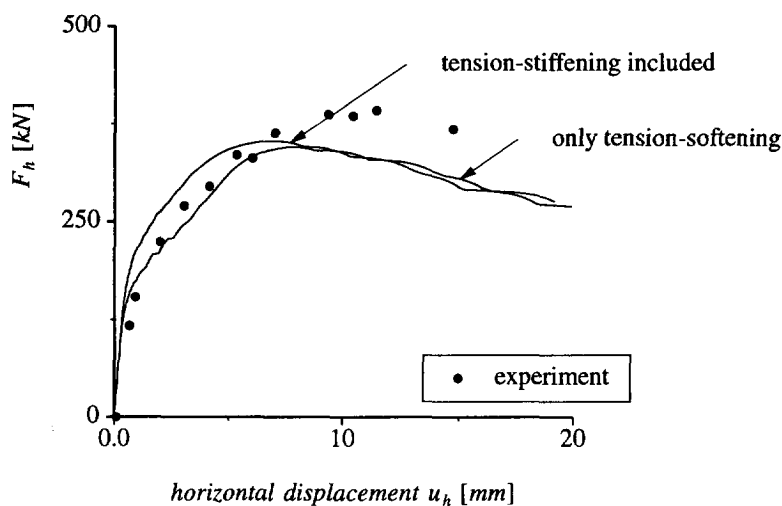


Figure 7.19 Panel S4. Load - displacement diagram.

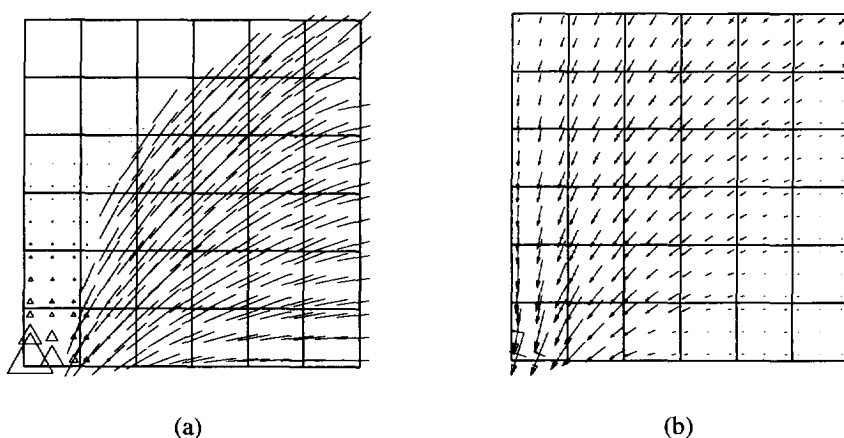


Figure 7.20 Panel S4. Results of the analysis at a displacement of 5 [mm]. (a) active cracks and plastic points ; (b) principal stresses.

ductile manner after peak-load which has also been observed during the experiment where the horizontal displacement could be increased approximately 30 % after the ultimate load had been reached. The results of the analysis are shown in Figures 7.20 and 7.21 at a horizontal displacement u_h of 5 [mm] and 20 [mm] respectively. The experimentally observed failure mode is related to crushing of the concrete in a region in the bottom-left part of the panel. This failure mechanism can also be observed from Figure 7.21(a) and (b), because the principal stresses at the bottom-left corner of the panel are almost reduced to zero.

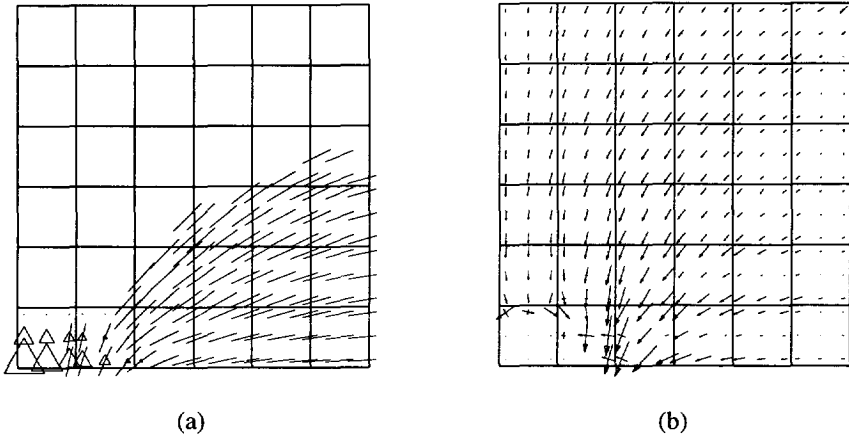


Figure 7.21 Panel S4. Results of the analysis at a displacement of 20 [mm]. (a) active cracks and plastic points ; (b) principal stresses.

The final panel which will be analyzed, is a panel with a "hidden tensile flange". In the tension side of the panel, additional reinforcement has been applied which increases the ultimate load, compared with panel S4, but results in a less ductile behavior, see Figure 7.22. The agreement between the experimental and calculated ultimate load is quite reasonable, but the calculated initial stiffness exceeds the experimental initial stiffness with approximately a factor equal to two. Also the displacement at the failure load is too small compared with the experimental displacement.

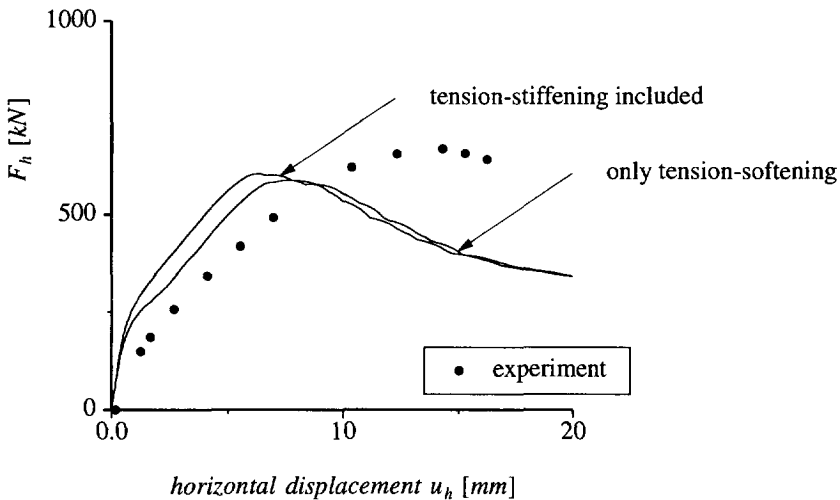


Figure 7.22 Panel S10. Load - displacement diagram.

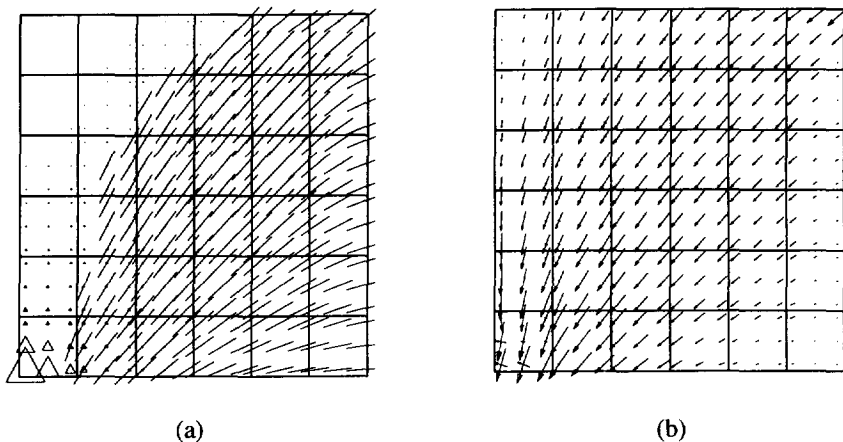


Figure 7.23 Panel S10. Results of the analysis at a displacement of 5 [mm]. (a) active cracks and plastic points ; (b) principal stresses.

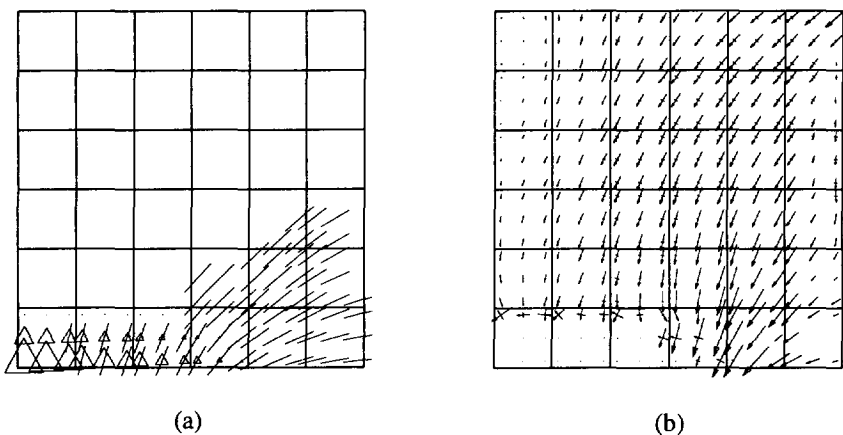


Figure 7.24 Panel S10. Results of the analysis at a displacement of 20 [mm]. (a) active cracks and plastic points ; (b) principal stresses.

The results of the analysis of panel S10, given in Figures 7.23 and 7.24, show the differences with the results of panel S4, mainly in the post-peak regime. The active cracks and plastic points as well as the direction of the principal compressive strut are almost equal for both panel S4 and S10, compare Figure 7.20 and Figure 7.23. The results at a displacement of 20 [mm] show a considerable different behavior between panel S4 and panel S10. The part of panel S10 in which the stresses are reduced to zero is much larger than the region in panel S4 which has also been observed in the experiments.

In conclusion, it has been shown that the agreement between the experimental and numerical results is good, and that the failure mechanism can be simulated. The

influence of the modeling of the tension-stiffening component on the load-displacement curve is in general small, but inclusion of it can result in a more stable iterative procedure in the pre-peak regime.

8. SUMMARY AND CONCLUDING REMARKS

The structural engineer more and more needs reliable numerical tools to analyze the post-failure behavior of structures in order to assess the structural safety. In general, a reliable tool consists of an accurate material description in combination with a robust solution strategy. In this study an attempt has been made to provide such a tool for the analyses of reinforced concrete structures.

A solution technique to solve the equilibrium problem has been proposed which consists of the combination of a constrained Newton-Raphson method with a line-search technique and a self-adaptive incremental load estimator based on external work. The proposed solution strategy has been used throughout this study and it has proven to meet the need of a robust solution. The convergence characteristics of the calculations presented in this study are satisfactory. The application of an indirect displacement control is essential to obtain converged solutions in the post-failure regime of the shear wall panels. With this method, which is in fact a combination of a constrained Newton-Raphson method and a load incrementation method, it is possible to control the calculation with the displacement of a single, dominant degree-of-freedom.

A material model for plain and reinforced concrete in a plane-stress situation has been discussed. It is assumed that the failure mechanism of concrete loaded in tension and compression is governed by crack growth at the micro-level. Furthermore it is assumed that the internal damage caused by these micro-cracks can be modeled using internal parameters which are related to a fracture energy in tension and to a compressive fracture energy. The material properties have been estimated using CEB-FIP recommendations which are based on the compressive strength of the concrete. The comparisons between numerical analyses with material properties based on these recommendations and experiments show that estimated material properties are adequate. The biaxial behavior of concrete is assumed to be governed by the failure surface of Kupfer and Gerstle with a tension-softening and a compression-softening constitutive behavior. The mechanical response of reinforced concrete is assumed to be given by a superposition of the elasto-plastic behavior of the reinforcement, the tension-softening behavior of the plain concrete and an additional stiffness due the interaction between concrete and reinforcement. The total amount of fracture energy due to distributed cracking is assessed using the average crack spacing based on CEB-FIP recommendations. For the biaxial behavior of reinforced concrete the biaxial loaded reinforced panels of Kollegger

and Mehlhorn have been used. It is not obvious from these experiments that the compressive strength should be reduced as a function of lateral cracking, since a constant reduction can be observed. This phenomenon is possibly a result of the size effect and the influence of different boundary conditions in the standard compression test and the actual experiment.

The constitutive model of plain concrete can be formulated in an incremental fashion or within a total strain concept. The rotating crack model falls within the latter category. In the former group of models, two fracture energy-based plasticity models have been presented, the Rankine plasticity model with mixed hardening and a composite yield function which governs the entire range of biaxial stress states. For all models, special attention has been given to the consistent formulation of the tangent stiffness matrix and the treatment of singularities in the formulations. The models have been compared with a fundamental tension-shear model problem which indicates that the constitutive behavior of the Rankine plasticity model and the rotating crack model show much resemblance. The models have been applied to different structures and a comparison between the numerical and experimental results indicates that the most promising material model for concrete is the fracture energy-based plasticity model. Application of the plasticity model to reinforced concrete structures in which biaxial stress states are prominent, shows that the plasticity model results in a stable and accurate algorithm. The entire pre- and post-failure regime can be traced in a stable manner, which gives a good impression of the failure characteristics of these type of structures.

The reinforcement has been modeled using an embedded formulation in which the displacements of the reinforcement are consistent with the displacement of the parent element. In this approach, perfect bond is assumed. The constitutive model for the reinforcing steel is given by an elasto-plastic uniaxial model. The constitutive model for plain concrete is given by the fracture energy-based plasticity model. The proposed model for reinforced concrete is a superposition of the stiffness of the reinforcement, the stiffness of the plain concrete and an additional stiffness due to the interaction between concrete and reinforcement. In this approach, the shear stiffness of the cracked, reinforced concrete has been neglected. The model has been validated with single-element simulations of experiments which show a good agreement between the numerical and experimental behavior as long as the anisotropy of the reinforcement is less than five. The average crack spacing based on CEB-FIP recommendations can be estimated within acceptable limits. Analyses of shear wall panels with the proposed model show in general a good agreement with the experimental results, but the pre-failure response is slightly too stiff which might be caused by an overestimation of the total amount of fracture energy.

In retrospect, a feedback can be made to the four objectives which were defined at the beginning of this study in section 1.1.

Regarding the first objective, to propose a solution technique which is stable and economic in the entire loading regime of the structure, it can be concluded that this objective is attained. The examples presented in this study are all calculated with the

proposed solution algorithm. Although sometimes difficulties are encountered, the solution algorithm has shown to be stable and general applicable which is a major advantage for the development of a numerical tool for structural engineers.

The second objective, to develop a constitutive model for reinforced concrete which incorporates the knowledge of nonlinear fracture mechanics used in crack propagation problems, is also achieved. The proposed model for reinforced concrete is based on a decomposition of the stiffness in a contribution of the plain concrete, a contribution of the reinforcement and an additional contribution due to the interaction between concrete and reinforcement. The model which describes the behavior of the concrete is based on the total amount of dissipated fracture energy at stabilized cracking which is determined by the average crack spacing. The additional stiffness contribution due to the interaction between concrete and reinforcement is based on the tensile strength of the material and on the effective tension area. In this manner, the behavior of reinforced concrete is based on a rational modeling.

The third objective, to develop a constitutive model for concrete which is stable and robust in all stress states, is achieved with the development of a composite plasticity model based on an incremental formulation. The model shows a behavior which is similar to the behavior of the rotating crack model in tension. In compression, the nonlinear behavior due to crushing of the material is also described. Furthermore, the interaction between the behavior in tension and the behavior in compression can be taken into account. The algorithm which has been developed has proven to be stable in all stress situations which have been encountered in the example calculations.

The last objective, the developed model should be able to predict the ultimate load and the failure mode within 30 % of the experimental behavior, is also achieved which is demonstrated by the analyses of experiments in Chapter 5 and Chapter 7.

REFERENCES

- ARREA, M. and INGRAFFEA, A.R. (1982) - Mixed-mode crack propagation in mortar and concrete. Report 81-13, Cornell University, Ithaca, New York, USA.
- BATHE, K.J. (1982) - *Finite element procedures in engineering analysis*. Prentice-Hall, Englewood Cliffs, New Jersey, USA.
- BATOZ, J.L. and DHATT, G. (1979) - Incremental displacement algorithms for nonlinear problems. *Int. J. Numer. Methods Engrg.*, **14**, p. 1262-1267.
- BAŽANT, Z.P. (1983) - Comment on orthotropic models for concrete and geomaterials. *J. Engrg. Mech.*, ASCE, **109**(3), p. 849-865.
- BAŽANT, Z.P. and OH, B.H. (1983) - Crack band theory for fracture of concrete. *Materials and Structures*, RILEM, **93**(16), p. 155-177.
- BECKER, E. and BÜRGER, W. (1975) - *Kontinuumsmechanik*. Teubner Verlag, Stuttgart, Germany.
- BELLINI, P.X. and CHULYA, A. (1987) - An improved automatic incremental algorithm for the efficient solution of nonlinear finite element equations. *Comp. Struct.*, **26**(1/2), p. 99-110.
- BERGAN, P.G. (1982) - Automated incremental-iterative solution methods in structural mechanics, in: *Recent Advances in Non-Linear Computational Mechanics*, eds. E. Hinton et al., Pineridge Press, Swansea, U.K., p. 41-62.
- BHIDE, S.B. and COLLINS, M.P. (1987) - Reinforced concrete elements in shear and tension. Publication 87-02, University of Toronto, Toronto, Canada.
- BRAAM, C.R. (1990) - Control of crack width in deep reinforced concrete beams. Dissertation, Delft University of Technology, Delft, The Netherlands.
- CEB-FIP (1990) - Model code 1990. Bulletin d'information, CEB, Lausanne, Switzerland.
- CERVENKA, V., PUKL, R. and ELIGEHAUSEN, R. (1990) Computer simulation of anchoring technique in reinforced concrete beams, in: *Computer Aided Analysis and Design of Concrete Structures*, eds. N. Bićanić et al., Pineridge Press, Swansea, U.K., p. 1-21.
- CHEN, W.F. (1982) - *Plasticity in reinforced concrete*. McGraw-Hill, New York, New York, USA.
- CLARKE, M.J. and HANCOCK, G.J. (1990) - A study of incremental-iterative strategies for nonlinear analyses. *Int. J. Num. Meth. Engrg.*, **29**, p. 1365-1391.
- CRISFIELD, M.A. (1981) - A fast incremental/iterative solution procedure that handles snap-through. *Comp. Struct.*, **13**(1/3), p. 55-62.
- CRISFIELD, M.A. (1982) - Accelerated solution techniques and concrete cracking. *Comp. Meth. Appl. Mech. Engrg.*, **33**, p. 858-607.
- CRISFIELD, M.A. (1983) - An arc-length method including line searchers and accelerations. *Int. J. Num. Meth. Engrg.*, **19**, p. 1269-1289.
- CRISFIELD, M.A. (1984) - Difficulties with current numerical models for reinforced concrete and some tentative solutions, in: *Computer Aided Analysis and Design of*

- Concrete Structures*, , eds. F. Damjanic et al., Pineridge Press, Swansea, U.K., p. 331-358.
- CRISFIELD, M.A. (1987) - Plasticity computations using the Mohr-Coulomb yield criterion. *Engrg. Comput.*, **4** , p. 300-308.
- CRISFIELD, M.A. and WILLS, J. (1989) - Analysis of R/C panels using different concrete models. *J. Engrg. Mech.*, ASCE, **115(3)** , p. 578-597.
- DE BORST, R. (1986) - Non-linear analysis of frictional materials. Dissertation, Delft University of Technology, Delft, The Netherlands.
- DE BORST, R. (1991) - The zero-normal stress condition in plane-stress and shell elastoplasticity. *Comm. in Appl. Numer. Methods*, **7** , p. 29-33.
- DE BORST, R. (1993) - A generalisation of J_2 -flow theory for polar continua. *Comp. Meth. Appl. Mech. Engrg.*, **103** , p. 347-362.
- DE BORST, R. and NAUTA, P. (1985) - Non-orthogonal cracks in a smeared finite element model. *Engrg. Comput.*, **2** , p. 35-46.
- DE BORST, R. and FEENSTRA, P.H. (1990) - Studies in anisotropic plasticity with reference to the Hill criterion. *Int. J. Numer. Methods Engrg.*, **29** , p. 315-336.
- DENNIS, J.E. and SCHNABEL, R.B. (1983) - *Numerical methods for unconstrained optimization and nonlinear equations*. Prentice-Hall, Englewood Cliffs, New Jersey, USA.
- ELFGREN, L. (1990) - Round-robin analysis of anchor bolts. Invitation. *Materials and Structures*, RILEM, **23(133)** , p. 78.
- FEENSTRA, P.H. and SCHELLEKENS, J.C.J. (1991) - Self-adaptive solution algorithm for a constrained Newton-Raphson method. Report 25.2-91-2-13, Delft University of Technology, Delft, The Netherlands.
- FEENSTRA, P.H., ROTS, J.G. and DE BORST, R. (1990) - Round robin analysis of anchor bolts. Report 25.2-90-5-07, Delft University of Technology, Delft, The Netherlands.
- FEENSTRA, P.H., DE BORST and R. ROTS, J.G. (1991a) - Numerical study on crack dilatancy. I: Models and stability analysis. *J. Engrg. Mech.*, ASCE, **117(4)** , p. 733-753.
- FEENSTRA, P.H., DE BORST and R. ROTS, J.G. (1991b) - Numerical study on crack dilatancy. II: Applications. *J. Engrg. Mech.*, ASCE, **117(4)** , p. 754-769.
- FORDE, B.W.R. and STIEMER, S.F. (1987) - Improved arc-length orthogonality methods for nonlinear finite element analysis. *Comp. Struct.*, **27(5)** , p. 625-630.
- GAMBAROVA, P.G. (1987) - Modelling of interface problems in reinforced concrete, in: *IABSE Report, vol. 54*, Delft University Press, Delft, The Netherlands, p. 1-16.
- GROEN, A.E. (1993) - Private communications.
- HANNANT, D.J., BUCKLEY, K.J. and CROFT, J. (1973) - The effect of aggregate size on the use of the cylinder splitting test as a measure of tensile strength. *Materials and Structures*, RILEM, **6(31)** , p. 15-21.
- HORDIJK, D.A. (1991) - Local approach to fatigue of concrete. Dissertation, Delft University of Technology, Delft, The Netherlands.

- KOITER, W.T. (1953) - Stress-strain relations, uniqueness and variational theorems for elastic-plastic materials with a singular yield surface. *Q. Appl. Math.* **11** , p. 350-354.
- KOLLEGER, J. (1988) - Ein Materialmodell für die Berechnung von Stahlbetonflächentragwerken. Dissertation, Gesamthochschule Kassel, Kassel, Germany.
- KOLLEGER, J. and MEHLHORN, G. (1990a) - Experimentelle Untersuchungen zur Bestimmung der Druckfestigkeit des gerissenen Stahlbetons bei einer Querkzugbeanspruchung. Heft 413, Deutscher Ausschuß für Stahlbeton, Berlin, Germany.
- KOLLEGER, J. and MEHLHORN, G. (1990b) - Material model for the analysis of reinforced concrete surface structures. *Comp. Mech.*, **6** , p. 341-357.
- KRIEG, R.D. and KRIEG, D.B. (1977) - Accuracies of numerical solution methods for the elastic-perfectly plastic model. *J. Pressure Vessel Techn.*, ASME, **99** , p. 510-515.
- KUPFER, H.B. and GERSTLE, K.H. (1973) - Behavior of concrete under biaxial stresses. *J. Engrg. Mech.*, ASCE, **99(4)** , p. 853-866.
- LABBANE, M., SAHA, N.S. and TING, E.C. (1993) - Yield criterion and loading function for concrete plasticity. *Int.J.Solids Structures*, **30(9)** , p. 1269-1288.
- LANGESLAG, F.J.C.M. (1992) - Evaluation of solution techniques in DIANA (in Dutch). Report 25.2-92-2-9, Delft University of Technology, Delft, The Netherlands.
- LEHWALTER, N. (1988) - Die Tragfähigkeit von Betondruckstreben in Fachwerkmodellen am Beispiel von Gedrungenen Balken. Dissertation, Technischen Hochschule Darmstadt, Darmstadt, Germany.
- MAIER, J. and THÜRLIMANN, B. (1985) - Bruchversuche an Stahlbetonscheiben. Report 8003-1, Eidgenössische Technische Hochschule Zürich, Zürich, Switzerland.
- MATTHIES, H.G. (1989) - A decomposition method for the integration of the elastic-plastic rate problem. *Int. J. Numer. Methods Engrg.*, **28** , p. 1-11.
- MATTHIES, H.G. and STRANG, G. (1979) - The solution of nonlinear finite element equations. *Int. J. Numer. Methods Engrg.*, **14** , p. 1613-1626.
- MÜHLHAUS, H.-B. (1989) - Application of Cosserat theory in numerical solutions of limit load problems. *Ing.-Arch.* **59** ,p. 124-137.
- NAGHDI, P.M. and TRAPP, J.A. (1975) - The significance of formulating plasticity theory with reference to loading surfaces in strain space. *Int. J. Engrg. Sci.* **13** , p.785-797.
- NAPOLEÃO, J., ELWI, A.E. and MURRAY, D.W. (1992) - An eigenvector-based strategy for the analysis of inelastic structures. *Comp. Struct.*, **42(5)** , p. 833-848.
- NELISSEN, L.J.M. (1972) - Biaxial testing of normal concrete. *Heron* **18** , p. 3-90.
- OLIVER, J. (1989) - A consistent characteristic length for smeared crack models. *Int. J. Numer. Methods Engrg.*, **28** , p. 461-474.
- ORTIZ, M. and POPOV, E.P. (1985) - Accuracy and stability of integration algorithms for elastoplastic constitutive relations. *Int. J. Numer. Methods Engrg.*, **21** , p. 1561-1576.
- PANKAJ (1990) - Finite element analysis in strain softening and localization problems. Dissertation, University College of Swansea, Swansea, U.K.

- PIJAUDIER-CABOT, G. and BAŽANT, Z.P. (1987) - Nonlocal damage theory. *J. Engrg. Mech.*, ASCE, **113**(10), p. 1512-1533.
- PRAMONO, E. and WILLAM, K.J. (1989) - Implicit integration of composite yield surfaces with corners. *Engrg. Comput.*, **7**, p. 186-197.
- RAMM, E. (1981) - Strategies for tracing the nonlinear response near limit points, in: *Nonlinear Finite Element Analysis in Structural Mechanics*, eds. W. Wunderlich et al., Springer Verlag, Berlin, Germany, p. 63-89.
- RIGGS, H.R. and POWELL, G.H. (1990) - Tangent constitutive matrices for inelastic finite element analyses. *Int. J. Numer. Methods Engrg.*, **29**, p. 1193-1203.
- RIKS, E. (1970) - On the numerical solution of snapping problems in the theory of elastic stability. Dissertation, Stanford University, Stanford, California, USA.
- ROTS, J.G. (1988) - Computational modeling of concrete fracture. Dissertation, Delft University of Technology, Delft, The Netherlands.
- ROTS, J.G. (1992) - Removal of finite elements in strain-softening analysis of tensile fracture, in: *Fracture mechanics of concrete structures*, ed. Z.P. Bažant, Elsevier Applied Science, London, U.K., p. 330-338.
- SAOURIDES, C. and MAZARS, J. (1989) - A multiscale approach to distributed damage and its usefulness for capturing structural size effect, in: *Cracking and damage. Strain localization and size effect*, eds. J. Mazars and Z.P. Bažant, Elsevier Applied Science, London, U.K., p. 391-403.
- SCHELLEKENS, J.C.J. (1992) - Computational strategies for composite structures. Dissertation, Delft University of Technology, Delft, The Netherlands.
- SCHELLEKENS, J.C.J. and DE BORST, R. (1990) - The use of the Hoffman yield criterion in finite element analysis of anisotropic composites. *Computers and Structures*, **37**(6), p. 1087-1096.
- SCHLANGEN, E. (1993) - Experimental and numerical analysis of fracture processes in concrete. Dissertation, Delft University of Technology, Delft, The Netherlands.
- SCHREYER, H.L., KULAK, R.F. and KRAMER, J.M. (1979) - Accurate numerical solutions for elastic-plastic models. *J. Pressure Vessel Techn.*, ASME, **101**, p. 226-234.
- SCHWEIZERHOF, K. (1992) - A general and consistent concept for line search algorithms in combination with arc-length constraints. Report 15/1992, University of Karlsruhe, Karlsruhe, Germany.
- SCHWEIZERHOF, K. and WRIGGERS, P. (1986) - Consistent linearization for path following methods in nonlinear FE-analysis. *Comp. Meth. Appl. Mech. Engrg.*, **59**, p. 261-279.
- SIMO, J.C. (1992) - Algorithms for static and dynamic multiplicative plasticity that preserve the classical return-mapping schemes of infinitesimal theory. *Comp. Meth. Appl. Mech. Engrg.*, **99**, p. 61-112.
- SIMO, J.C. and TAYLOR, R.L. (1985) - Consistent tangent operators for rate-independent elastoplasticity. *Comp. Meth. Appl. Mech. Engrg.*, **48**, p. 101-118.
- SIMO, J.C. and TAYLOR, R.L. (1986) - A return mapping algorithm for plane stress elastoplasticity. *Int. J. Numer. Methods Engrg.*, **22**, p. 649-670.

- SIMO, J.C., KENNEDY, J.G. and GOVINDJEE, S. (1988) - Non-smooth multisurface plasticity and viscoplasticity. Loading/unloading conditions and numerical algorithms. *Int. J. Numer. Methods Engrg.*, **26**, p. 2161-2185.
- VAN DER VORM, P.L.J. (1988) - A numerical study on reinforced concrete panels. Report and appendices, Delft University of Technology, Delft, The Netherlands.
- VAN MIER, J.G.M. (1984) - Strain-softening of concrete under multiaxial loading conditions. Dissertation, Eindhoven University of Technology, Eindhoven, The Netherlands.
- VECCHIO, F.J. and COLLINS, M.P. (1982) - The response of reinforced concrete to in-plane shear and normal stresses. Publication 82-03, University of Toronto, Toronto, Canada.
- VECCHIO, F.J. and NIETO, M. (1991) - Shear-friction tests on reinforced concrete panels. *J. ACI*, **ACI**, **88**(3), p.371-379.
- VERVUURT, A., SCHLANGEN, E. and VAN MIER, J. (1993) - A numerical and experimental analysis of the pull-out behavior of steel anchors embedded in concrete. Report 25.5-93-1, Delft University of Technology, Delft, The Netherlands.
- VONK, R.A. (1992) - Softening of concrete loaded in compression. Dissertation, Eindhoven University of Technology, Eindhoven, The Netherlands.
- WALRAVEN, J.C. and REINHARDT (1981) - Theory and experiments on the mechanical behaviour of cracks in plain and reinforced concrete subjected to shear loading. *Heron*, **26**(1a), p. 3-68.
- WALRAVEN, J.C. (1993) - Private communications.
- WANG, Q.B., VAN DER VORM, P.L.J. and BLAAUWENDRAAD, J. (1990) Failure of reinforced concrete panels - How accurate the models must be ?, in: *Computer Aided Analysis and Design of Concrete Structures*, eds. N. Bićanić et al., Pineridge Press, Swansea, U.K., p. 153-163.
- WEMPNER, G.A. (1971) - Discrete approximations related to non-linear theories of solids. *Int.J. Num. Meth. Engrg.*, **7**, p. 1581-1599.
- WILLAM, K.J., PRAMONO, E. and STURE, S. (1986) - Fundamental issues of smeared crack models, in: *Proc. SEM/RILEM Int. Conf. Fracture of Concrete and Rock*, eds. S.P. Shah and S.E. Swartz, Springer-Verlag, New York, USA, p. 142-157.
- WILLAM, K.J. and DIETSCHKE, A. (1992) - Fundamental aspects of strain-softening descriptions, in: *Fracture mechanics of concrete structures*, ed. Z.P. Bažant, Elsevier Applied Science, London, U.K., p. 227-238.
- WITTMAN, F.H. (1983) - Structure of concrete with respect to crack formation, in: *Fracture mechanics of concrete*, ed. F.H. Wittman, Elsevier, Amsterdam, The Netherlands, p. 43-74.

SAMENVATTING

NUMERIEKE ASPECTEN VAN TWEE-ASSIGE SPANNINGSTOESTANDEN IN ONGEWAPEND EN GEWAPEND BETON

Er bestaat een groeiende behoefte in de constructiepraktijk aan betrouwbare numerieke gereedschappen om het na-critische gedrag van constructies te kunnen bepalen teneinde de veiligheid van de constructie te kunnen inschatten. In het algemeen kan gesteld worden dat een betrouwbare rekentechniek bestaat uit een nauwkeurige materiaalbeschrijving in combinatie met een robuuste oplosmethodiek. In deze studie is een verdere stap gezet om een dergelijk numeriek gereedschap te ontwikkelen.

Een oplosmethodiek om het evenwichtsprobleem op te lossen wordt voorgesteld die bestaat uit een Newton-Raphson iteratieprocedure in combinatie met een booglengtemethode. Daarbij is het convergentiegedrag verbeterd met behulp van een line-search techniek en een schattingsmethode voor het belastingincrement. De laatste verfijning is waarschijnlijk de belangrijkste verbetering van het convergentiegedrag.

Een materiaalmodel voor ongewapend en gewapend beton is eveneens geformuleerd. De belangrijkste aanname daarbij is dat de bezwijkmechanismen van beton zowel in trek als in druk bepaald worden door scheurgroei op microniveau. Voorts is aangenomen dat de interne beschadiging veroorzaakt door deze microscheuren kan worden gemodelleerd door gebruik te maken van interne parameters die gerelateerd kunnen worden aan een breukenergie in trek en een overeenkomstige energie in druk. De materiaaleigenschappen van het beton zijn gerelateerd aan de druksterkte door gebruik te maken van de CEB-FIP bepalingen. De overeenstemming tussen experimentele en numerieke resultaten toont aan dat de materiaaleigenschappen, geschat op basis van deze aanbevelingen, nauwkeurig zijn. Het gedrag van gewapend beton is beschreven met behulp van een superpositie van het elasto-plastische gedrag van het wapeningsstaal, het softening gedrag van het beton en een additionele stijfheid tengevolge van de interactie tussen beton en wapeningsstaal. De totale hoeveelheid breukenergie tengevolge van de uitgesmeerde scheurvorming in gewapend beton is bepaald aan de hand van de gemiddelde scheurafstand op grond van CEB-FIP aanbevelingen.

Het twee-assige gedrag van ongewapend beton is gemodelleerd met een gecombineerd plasticiteitsmodel: een hoofdspanningscriterium voor de trekspanningen en een Von Mises plasticiteitsmodel voor de drukspanningen. Het gecombineerde vloeiooppervlak vertoont een overeenstemming met de experimentele bezwijkomhullende van Kupfer en Gerstle. Bijzondere aandacht is gegeven aan de consistente formulering van de tangentiële stijfheidsrelatie en een consistente behandeling van de singuliere punten van het vloeiooppervlak. Het gedrag van dit plasticiteitsmodel is vergeleken met het gedrag van het roterend scheurmodel waarbij duidelijk is geworden dat het gedrag van beide modelleringen sterke overeenkomsten heeft. De combinatie van trek-drukspanningstoestanden, die in het verleden tot numerieke problemen leidde, kan nu stabiel en nauwkeurig worden beschreven en geanalyseerd. Het twee-assige gedrag van

gewapend beton, met name de trek-druk interactie, is bestudeerd aan de hand van tweedimensionaal belaste, gewapend betonpanelen van Kollegger en Mehlhorn. Het is niet duidelijk aantoonbaar dat de druksterkte van het beton wordt beïnvloed door laterale scheurvorming. Echter, een constante reductie van de druksterkte ten opzichte van de kubusdruksterkte kan worden geobserveerd, wat waarschijnlijk meer een gevolg is van de verschillende randvoorwaarden en proefstukgrootten dan van de laterale scheurvorming.

CURRICULUM VITAE

Naam	Peter Hendrikus Feenstra
21 september 1962	Geboren te Sittard
1978	MAVO-diploma te Heerlen
1978-1981	MTS te Heerlen
1981-1983	HTS te Heerlen
1983-1988	Studie Civiele Techniek aan de Technische Universiteit te Delft. Onderwerp van het afstudeerproject : numerieke plasticiteitstheorie. Het afstudeerwerk is verricht bij TNO-Bouw, afdeling Numerieke Mechanica
27 oktober 1988	Diploma van civiel ingenieur (met lof)
november 1988 - april 1989	Wetenschappelijk medewerker TNO-Bouw, afdeling Numerieke Mechanica
april 1989 - oktober 1993	Werkzaam aan de TU-Delft, faculteit der Civiele Techniek voor onderzoek van de Stichting voor de Technische Wetenschappen (STW)